Theoretical and Experimental Studies on Confined Vortex Flows

Georgios Haralampou Vatistas

A Thesis

in

The Department

of

Mechanical Engineering

Presented in Partial Fulfilment of the Requirements
for the degree of Doctor of Philosophy at
Concordia University
Montréal, Québec, Canada

July 1984

ABSTRACT

ABSTRACT

Theoretical and Experimental Studies on Confined Vortex Flows

Georgios Haralampou Vatistas
Concordia University, 1984

For a simple vortex to evolve energy must be externally provided. Extrema are shown to exist in this case followed by the Helmholtz minimum viscous rate of dissipation condition for the steady-state. The required energy that must be supplied to the flowfield for a forced vortex to evolve is obtained analytically utilizing the integral energy equation.

An analytical model directed toward studying selected fluid parameters in vortex chambers is presented. From the model, the dimensionless quantities (a) core size, (b) static pressure drop across the chamber, (c) radial static pressure distribution, and (d) radius of reversed flow at the exit, are shown to be functions of chamber geometry only. In addition, it is experimentally demonstrated that in chambers with small contraction ratios, the static pressure drop across the chamber can be effectively lowered by plugging the exit flow.

Next, a numerical solution to the viscous equations for the swirling confined flow is presented. The method utilizes the forward time centered space finite differences formulation, with attention focused toward the steady-state flowfield condition.

The presented theoretical results and experimental evidence compare well with each other as well as with that appearing in the literature. The difference between viscous flowfield numerical simulation results

and the inviscid potential flow solutions are outlined. Finally, numerical results are conformal qualitatively using previously known experimental findings.

ACKNOWLEDGEMENTS

ACKNOWLEDGEMENTS

Among those that the author owes a particular debt of gratitude are his advisors C.K. Kwok and S. Lin for their guidance and valuable advice.

Thanks are due to D.G. Lilley of Oklahoma State University, for occasional very informative conversations. The technical assistance by the fluid mechanics group, lead by J. Elliott is greatly appreciated. For typing the manuscript, thanks are extended to Mrs. Ilana Crawford. The author can only partially acknowledge his wife Stavroula for her love, patience and encouragement.

The support provided by the Mechanical Engineering Department at Concordia University as well as the scholarship by NSERC is acknowledged.

The present work was partially supported by NSERC Grant No. A7435.

TABLE OF CONTENTS

TABLE OF CONTENTS

	Page
ABSTRACT	i
ACKNOWLEDGEMENTS	iii
TABLE OF CONTENTS	iv
LIST OF FIGURES	vii
LIST OF TABLES	xi
NOMENCLATURE	xii
CHAPTER 1	
INTRODUCTION	1
1.1 General	1
1.2 Vortex Chamber Flows	3
1.3 Previous Work on Vortex Chamber Flows	5
1.4 Summary of the Thesis and Findings	8
CHAPTER 2	
SIMPLE VORTEX FLOWS	10
2.1 The Principle of Least Action	11
2.2 The Equations of Motion for Axisymmetric Swirling Flows	11
2.3 A Variational Principle	13
2.4 The Forced Vortex	17
2.5 The Potential Vortex	28
2.6 The Rankine's Vortex	35

Page

CHAPTER 3

EXPERIMENTAL APPARATUS AND PROCEDURE 42

3.1 Experimental Facility for Vortex Chamber Flows 42

3.2 Instrumentation 45

3.3 Experimental Procedure and Data Reduction 49

3.4 Reliability of the Experimental Results 50

CHAPTER 4

ANALYTICAL AND EXPERIMENTAL STUDIES OF FLOWFIELDS IN VORTEX CHAMBERS. 52

4.1 Governing Equations 52

4.2 The Core-Size 56

4.3 The Static Pressure Drop and Radial Distribution 72

4.4 The Aerodynamic Resistance of Vortex Chamber 79

4.5 Experimental Velocity Map within the Chamber 87

4.6 The Reverse Flow Radius Inside the Core 94

4.7 On the Reduction of Pressure Drop Across the Vortex Chambers . 103

CHAPTER 5

APPROXIMATE AIR VELOCITY MAPPING IN THE VORTEX CHAMBER 110

5.1 The Mathematical Model 110

5.2 The Finite Difference Equations 115

5.3 Boundary Conditions 118

5.4 Stability Considerations 120

5.5 Computation Procedure 121

5.6 Results and Discussions on Approximate Velocity Mapping 121

Page

CHAPTER 6

CONCLUSIONS 135

REFERENCES 137

APPENDIX A 147

APPENDIX B 149

APPENDIX C 157

APPENDIX D 161

APPENDIX E 165

LIST OF FIGURES

LIST OF FIGURES

Figure		Page
1.2.1	A Typical Flowpattern in a Vortex Chamber [24].	4
2.2.1	Coordinate System.	11
2.3.1	Schematic of the Problem.	14
2.4.1	The Cylindrical Vessel.	18
2.4.2	Velocity Profiles During Spin-Up with $\omega_I = 0$.	19
2.4.3	Velocoty Profiles During Spin-Up with $\omega_I = \frac{1}{2}\omega_F$.	20
2.4.4	Dimensionless Viscous Dissipation and Change of Kinetic Energy vs $V_{\theta I}/V_{\theta F}$ for the Spin-Up Process ($A = -F_T/\frac{1}{2}\rho\pi R_o^2 V_{\theta F}^2$, $B = \delta T/\frac{1}{2}\rho\pi R_o^2 V_{\theta F}^2$).	24
2.4.5	Dimensionless Energy Supply vs. $V_{\theta I}/V_{\theta R}$ for the Spin-Up Process.	26
2.5.1	Production of a Vortex Between Two Circular Parallel Plates with Small Spacing.	33
2.6.1	The Rankine's Vortex.	34
2.6.2	Decay of Rankine's Vortex with $\bar{t} = t\nu/R_o^2$ and Free-Slip at $r = R_o$.	36
2.6.3	Decay of Rankine's Vortex vs $\bar{t}$ with No-Slip at $r = R_o$. . .	38
2.6.4	Cumulative Dimensionless Viscous Dissipation During the Decay of a Confined Rankine Vortex.	40
3.1.1	A Layout of the Experimental Facility.	43
3.1.2	The Cyclone Chamber [61]	44
3.1.3	The Five-Hole Pitot-Probe.	46
3.1.4	Illustration of the Velocity Components or Flow Direction in Association with the Five-Hole Pitot-Probe.	47
3.1.5	Experimental Arrangement for the Reduction of Static Pressure Drop Across the Chamber Experiments.	48
4.1.1	Schematic of the Physical System	53

Figure		Page
4.2.1	Experimental Tangential Velocity Distribution for Different Axial Stations [$\bar{z}$ = distance from the bottom plate/height of the chamber].	55
4.2.2	Core Size on D-plane for Different [R_E/R_0) (Axial Station $\bar{z}_4$).	59
4.2.3	Core Size on O-Plane for Different Contraction Ratios.	61
4.2.4	Variation of X_{CD} with the Dimensionless Inlet Area ($A_0 = 2\pi R_0^2$, $R_E/R_0 = 0.3$).	63
4.2.5	Core Size on D-Plane vs. Q ($R_E/R_0 = 0.3$).	64
4.2.6	Core Size on O-Plane vs. Q.	65
4.2.7	Experimental Core Size vs. Q from Ref. [66] [$z_6 = 0.56$, $R_E/R_0 = 0.21$].	67
4.2.8	Experimental Radial Distribution of the Tangential Velocity for Different Inlet Volumetric Flowrates.	68
4.2.9	Experimental Radial Distribution of the Tangential Velocity for Different Inlet Volumetric Flowrates from Ref. [66].	69
4.2.10	Core Size on O-Plane vs. Inlet Swirl [$R_E/R_0 = 0.333$].	70
4.2.11	Core Size on O-Plane vs. Inlet Swirl [$R_E/R_0 = 0.5$].	71
4.3.1	Variation of the Dimensionless Pressure Drop Across the Chamber with the Inlet Volumetric Flowrate for Three Contraction Ratios.	75
4.3.2	Static Pressure Distribution Inside the Vortex Chamber ($R_E/R_0 = 0.3$).	77
4.3.3	Experimental Static Pressure Distribution Inside the Vortex Chamber from Ref. [66].	78
4.3.4	Static Pressure Distribution for Different Axial Stations.	80
4.3.5	Dimensionless Pressure Drop Across the Chamber vs. Contraction Ratio.	81
4.3.6	ΔP vs. Q for Three Different Contraction Ratios.	82
4.3.7	Dimensionless Pressure Drop Across the Vortex Chamber vs. Inlet Swirl $R_E/R_0 = 0.333$, — Eq. (4.3.2), --- Theory from Ref. [27].	83

Figure		Page
4.3.8	Dimensionless Pressure Drop Across the Vortex Chamber vs. Inlet Swirl ($R_E/R_o = 0.5$).	84
4.4.1	$\Delta\tilde{P}$ vs. $[R_E/R_o]$ and $[A_{in}/A_o]$.	86
4.5.1	Difference in Head Between Taps 5 and 4 of the Pitot-Probe (Δh_m = measured, Δh_c = correction, Δh_a = actual).	88
4.5.2	Dimensionless Axial Velocity vs. the Radius for the Axial Station $\bar{z}_2 = 0.285$.	90
4.5.3	Dimensionless Axial Velocity vs. the Radius for the Axial Station $\bar{z}_3 = 0.396$.	90
4.5.4	Dimensionless Axial Velocity vs. the Radius for the Axial Station $\bar{z}_4 = 0.510$.	91
4.5.5	Dimensionless Axial Velocity vs. the Radius for the Axial Station $\bar{z}_5 = 0.618$.	92
4.5.6	Dimensionless Axial Velocity vs, the Radius for the Axial Station $\bar{z}_6 = 0.729$.	93
4.6.1	Artistic Impression of the Entrained Flow at the Outlet.	95
4.6.2	The Reverse Flow Radius vs. the Inlet Volumetric Flowrate for $R_E/R_o = 0.1$.	97
4.6.3	The Reverse Flow Radius vs. the Inlet Volumetric Flowrate for $R_E/R_o = 0.15$.	98
4.6.4	The Reverse Flow Radius vs. the Inlet Volumetric Flowrate for $R_E/R_o = 0.2$.	100
4.6.5	The Reverse Flow Radius vs. the Inlet Swirl.	102
4.7.1	Overall Energy Distribution.	104
4.7.2	Pressure Drop Across the Chamber vs. Plug Position (□, Q = 0.035 m^3/s ◇, Q = 0.050 m^3/s).	106
4.7.3	Different Tip Configuration of the Cone.	107
4.7.4	Pressure Drop Across the Chamber vs. Plug Position with Diffuser (□, Q = 0.035 m^3/s, ◇, Q = 0.050 m^3/s, ▽, Q = 0.066 m^3/s).	108
5.1.1	Mathematical Model of the Vortex Chamber.	111

Figure		Page
5.2.1	The Grid System.	113
5.2.2	Arrangement of Finite Difference Variables in a Typical Cell.	114
5.6.1	Axial Distributions of the Radial Velocity in Different Radial Stations.	122
5.6.2	Typical Experimental Axial Distributions of the Tangential and Radial Velocities [79].	123
5.6.3	Axial Distributions of the Tangential Velocity in Different Axial Stations.	124
5.6.4	Circulation and Tangential Velocity vs. the Radius for Different Values of Parameter k [80].	126
5.6.5	Radial Distribution of the Tangential Velocity in Different Axial Stations.	128
5.6.6	Axial Velocity vs. the Radius for z/H = 0.2.	129
5.6.7	Axial Velocity vs. the Radius for z/H = 0.4.	130
5.6.8	Axial Velocity vs. the Radius for z/H = 0.6.	131
5.6.9	Axial Velocity vs. the Radius for z/H = 0.8.	132
5.6.10	Axial Velocity vs. the Radius with Free-Slip on the Circumferential Wall.	134
E.1	The Grid System for the Inviscid Potential Flow Simulation.	168

LIST OF TABLES

LIST OF TABLES

Table		Page
4.3.1	Flow Coefficients.	73
5.6.1	Specifications for the Numerical Problem.	133

NOMENCLATURE

NOMENCLATURE

A_{in}	inlet area of the vortex chamber
A_o	cross-sectional area of the vortex chamber ($A_o = \pi R_o^2$)
a	dimensionless geometric parameter ($a = [(A_{in}/A_o)/(R_E/R_o \cos\psi)]^2$)
C_Q	flow coefficient
Curl	curl of a vector field
div	divergence of a vector field
d	spacing between two parallel circular disk
$\dot{E}_s$	rate of energy supply
E_s	total energy supply
Eu	Euler's number
$\vec{e}_r, \vec{e}_\theta, \vec{e}_z$	unit vectors in r, θ and z directions
$\dot{F}$	rate of viscous energy dissipation in the control volume
F_T	viscous energy dissipation in the control volume
$F_T, \bar{t}$	cumulative viscous energy dissipation as a function of $\bar{t}$
g	gravitational acceleration
h'	height of the conical plug
h_{in}	height of the inlet port
$\vec{n}$	unit normal vector drawn outward the control surface
P	static pressure
$\hat{P}$	ratio of static pressure to constant density ($\hat{P} = P/\rho$)
Q	inlet volumetric flowrate
Q_{Rin}	volumetric flowrate of the reverse flow entering the chamber
Q_{Ro}	outlet volumetric flowrate of the reverse flow
Q_O	volumetric flowrate of the fluid passing through $R_{CO} \leq r \leq R_E$

$\vec{q}$	total velocity vector $(\vec{e}_r V_r + \vec{e}_\theta V_\theta + \vec{e}_z V_z)$
q	magnitude of the total velocity vector $(q = \sqrt{V_r^2 + V_\theta^2 + V_z^2})$
r,θ,z	radial, tangential and axial coordinates respectively
R_i, R_o	radii of the inner and outer cylinders respectively (R_o is also the radius of the vortex chamber)
R_E	radius of the throat
$\bar{R}$	dimensionless reverse flow radius $(\bar{R} = R_R/R_E)$
R_R	reverse flow radius
$R_{i,j}$	residuals
s	control surface
t	time
$\bar{t}$	dimensionless time $(\bar{t} = \nu t/R_o^2)$
t_{res}	residence time
T	kinetic energy
T_{int}	initial kinetic energy
V_r, V_θ, V_z or $\bar{V}_r, \bar{V}_\theta, \bar{V}_z$	average velocity components in r,θ, and z directions respectively
V_r', V', V_z'	fluctuating velocity components in r,θ, and z directions respectively
V_{zch}	average axial velocity in the main chamber $(V_{zch} = Q/\pi R_o^2)$
V	volume
Z_o	distance above the top plate
Z'	distance of the tip of the cone from the top plate

Greek Symbols

α	donor cell constant
Γ	vortex strength

γ	specific weight
$\Delta\hat{P}$	"pressure" change
$\Delta t, \Delta r, \Delta z$	time increment, radial and axial distances between two neighboring mesh points respectively
$\Delta hm, \Delta hc, \Delta ha$	measured, corrected and actual differences in head
$\delta_{i,j}$	Kronecker "delta"
δE_s, δT	change in energy supply and kinetic energy respectively
$\vec{\nabla}$	vector differential operator
ϵ	small scalar parameter
ϵ_m	eddy viscosity
μ	dynamic viscosity
ν	kinematic viscosity
ν_T	turbulent kinematic viscosity
ν_ℓ	laminar kinematic viscosity
ξ, η, ζ	vorticities in r, θ and z directions
$\pi(t)$	general function of time
ρ	density
σ	stress component
τ	shear stress
ϕ	inlet angle
$\overset{\circ}{\Phi}, \Phi$	rate of viscous energy dissipation per unit volume and scalar function respectively
ψ', θ'	pitch and yaw angles of the pitot-probe respectively
ψ	streamfunction
ω	angular velocity, overrelaxation function

Subscripts

CE, CO, CD	core size on E, O and D planes
E, O, D, in	properties evaluated on E, O, D and in planes

F,I	final and initial conditions of the variable respectively
i,j	mesh-point indexes
int	initial condition

Superscripts

$\ell,\ell+1$	previous and updated value of the variable
n	new value of the variable

CHAPTER 1

INTRODUCTION

CHAPTER 1

INTRODUCTION

1.1 General

Vortex flows should be familiar to anyone who has taken the time to observe the motion of water as it drains out of a bathtub, or has seen satellite pictures of a hurricane. These phenomena have also fascinated man from the earliest days. The whirling and swirling motion of water and air, may have inspired artists and craftsmen in antiquity, in the design of spiral ornamentation [1]. Aristotle, in 4th century B.C., after observations on whirlwinds (tornadoes) he wrote [2],

> "So the whirlwind....moves things by its wind in the direction in which it is blowing in a straight line and whirls around by its circular motion and forcibly snatches up whatever it meets".

In the 15th century A.D., Leonardo da Vinci shows sketches of the alternating vortices behind an obstacle in great detail [3]. Euler and d'Alembert in the 1750's considered the kinematics of vortex motion. But formal analytical treatment commenced with a classical paper by Helmholtz (1859) "On Integral of the Hydrodynamic Equations Corresponding to Vortex Motion". Lord Kelvin (1867), motivated by this work, proposed that atoms are actually vortices, although vortex theories for the molecule and the universe were presented earlier by Rankine and Descartes respectively [4].

Today in fluid dynamics, flow of a real fluid cannot be realized without the presence of vortices. Other classifications of scientific knowledge such as: low temperature physics, ion flow dynamics, meteorology etc., show great interest in vortex flows. This lies mainly on the fact

that, they are either governed by similar laws, or one of their processes involves fluid or plasma moving in circles [5-7]. It is therefore clear why these phenomena are considered by many among the most important subjects in the field, and have preoccupied research effort for many years.

The continued interest on confined vortex flows in particular has been motivated by a large number of engineering applications, which utilize these phenomena. The first application, the dust collector, dates back to 1885. In 1877 DeLaval presented his centrifugal separator used to separate cream from milk [8]. Based on the same principle, several other equipment were built with the task to separate fluid-solid mixtures or fluids with different densities. Confined vortex phenomena are also utilized for energy separation [9,10]. The Ranque Hilsch tube [11] achieves the latter and is used as a low cost refrigerator. The high specific impulse Gaseous Fission Rocket, an American project of the 1950's, uses the artificially created gravity to hold gaseous nuclear fuel in suspension. Although this project was never materialized, the associated research contributed to a better understanding of confined vortex phenomena [12,13]. One of the most known engineering applications is the vortex amplifier [14]. Although still in use today in pneumatic systems, it is fighting a loosing battle to a more compact and inexpensive microchip.

Confined vortical flows have also been extensively employed in the gas turbine combustors to effectively stabilize the flame in the primary zone, and thus satisfy many of the stringent requirements demanded by this high performance engine [15-17]. Recent success in burning low calorific value fuels in cyclone chambers [18-21] has revived the interest of several investigators to further explore these intricate flows. A result of

this renewed interest is also the present work.

There are many advantages of the cyclone combustor in comparison to conventional combustion chambers. They lie mainly on a unique flow pattern produced by the dominant circumferential velocity component. The strong centrifugal field created by the tangential inlets, alters the two-dimensional radial-axial flow and aids the combustion processes in several ways. The evolved secondary flow regions exhibit ideal conditions, whereupon a waste gas can be efficiently burned. The spiral fluid motion, enhances the residence of solid fuel in the chamber, and provides adequate time even for the most "difficult" fuel to be completely burned. Unfortunately all these benefits are achieved at the expense of a large pressure loss. Nonetheless, a superposition of the gas-turbine combustor and cyclonic flows, may produce the needed combustion system [22] suitable for low volatility and heating value fuels. However, before such a hybrid combustor is built, sufficient understanding of vortex flow and liquid droplet interaction must first be acquired.

1.2 Vortex Chamber Flows

Vortex chambers in general, have a cylindrical configuration with a central axis outlet and circumferential inlets. The inlet ports may be arranged near the top plate, at the bottom plate or both. An alternate design features a rotating chamber with a porous circumferential wall from which fluid can enter into the chamber.

The swirling motion, imparted to the fluid by the inlet ports, generates a strong centrifugal force-field which gives rise to the complex flow-pattern of Fig. 1.2.1 taken from [23]. It can be seen that, as the fluid enters the chamber it is immediately confronted by a strong

centrifugal force. In the attempt to find paths leading to the outlet with the least resistance, it is divided into two streams. The first, propagates along the circumferential wall and then is directed to the outlet at a point near the top plate. The familiar eddy motion in the upper corner is noticeably present. The second, flows towards the central axis following closely the bottom plate. One expects the second stream to exit the chamber through an area close to the central axis. However, the static pressure in this region has dropped below the pressure of the exterior to the chamber ambient air [24], and the induced reverse flow, forces the stream to reach the outlet at a larger radius. A

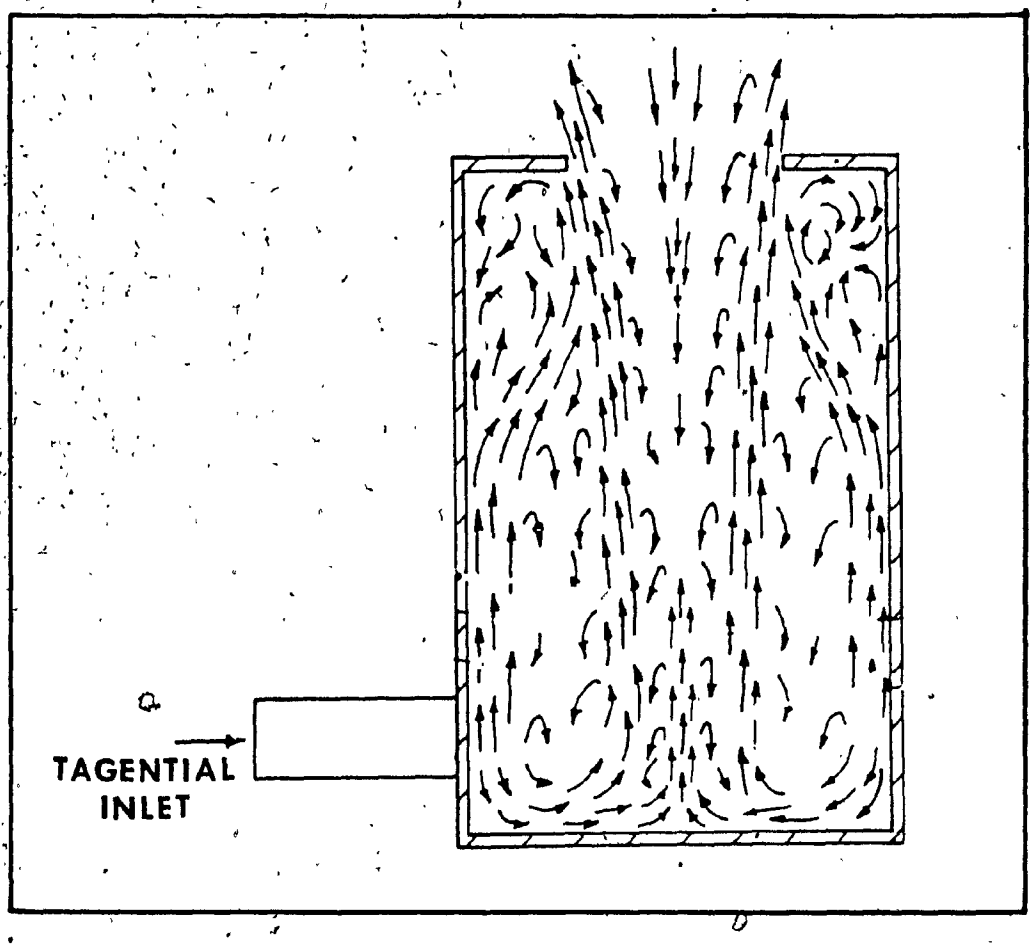

Fig. 1.2.1: A Typical Flowpattern in a Vortex Chamber [23]

common sight in vortex chambers is the two recirculatory flow areas, shown in the same figure. The toroidal, eddy type fluid motion within the chamber, is of the same nature as that through a bend. The reverse flow taking place in the vortex core, and in the vicinity of the outlet is already attributed to the static pressure reduction within the chamber to values which are below the ambient.

1.3 Previous Work on Vortex Chamber Flows

An extensive review by Lewellen [25] has shown an impressive number of papers dealing with both the experimental and theoretical facets of the confined vortex phenomena. The experimental work has been mainly focused on specific applications. Empirical relations were developed based on the experimental results and as expected, their validity is limited to a narrow spectrum of specific applications. The theoretical research was confined to particular solutions of the conservation equations. A numerical solution to the general confined vortex equations even today, in the era of high speed computing machines is indeed a formidable endeavor.

Although the dominance and form (Rankine's free-forced vortex) of the tangential velocity in this sort of flow was evident to fluid dynamicists from the beginning, there is little work done in defining where the velocity changes from free to forced vortex (core size). The early studies of Binnie and Hookings [26] focused on the discharge of swirling water through trumpet-shaped circular weirs. Lewellen discussed the point of maximum tangential velocity in a cylindrical chamber, utilizing Binnie's et al maximum flowrate principle. Recently, Shakespeare and Levy [27] reported new experimental findings for the velocity distribution

on the exit plane of a rotating chamber. Their theoretical study given in the same paper shows an overestimation of the core size.

Detailed map of the aerodynamic pattern within a short vortex chamber were presented by Savino and Keshock [28]. Kwok [29] has shown the velocity distribution on the exit plane for small aspect and contraction ratio vortex chambers. The studies presented in Ref. 28 are connected with the nuclear gaseous or solid particulate confinement, while the work by Kwok was motivated by the emerging fluidic technology of the sixties.

The experimental research in high aspect ratio vortex chamber is mainly a result of research and development on vortex separator and cyclone furnaces. In a comprehensive survey article, Syred et al [30], reviewed the problems of low calorific-value gases in various types of cyclone combustors. The early experimental work of Kalisheovshevshii and Gachev [31] was directed towards the detailed investigation of velocity and temperature distributions for a horizontal cyclone furnace. Later, Baluev and Troyankin [23] showed experimentally the cold aerodynamic structure of gas flow in a vertical chamber. Continuing their investigations, the same authors [32] further studied the effects of several design parameters on the aerodynamics of the same experimental model. The turbulent flow structure of such flows was carried out by Ustimenko and Bukhman [33].

Turbulent flow structures in vortex chambers under hot conditions were reported by Styles et al [34]. The chamber studied is of the separator type with top inlets and an exhaust manifold protruding into the chamber. Further work, has shown the flame stabilization to depend on the ratio of gas/air mixture [35,36].

The complexity presented by vortex chamber flowfields have forced theoreticians to focus their attention on particular solutions of the general equations of motion. Many were able to reduce the Navier-Stokes equations to a form amenable to analytical treatment [37,38]. Wormley [39] developed a mathematical model for short cylindrical chambers based on the integral equations of motion. Numerical solution of Wormley's equations with the inclusion of eddy viscosity, was obtained by Kwok et al [40]. A close form solution to Navier-Stokes equations for the swirling flow in a "thin" chamber was also previously reported by Kwok [29].

The abundance of recirculatory flow regions in vortex flowfields, presents extreme complexities, and flow characteristization can oly be possible by numerical integration of the complete set of the Navier-Stokes equations. The first attempt to numerically solve these equations was by Lilley and Vatistas [41]. The solution was achieved extending the well known two-dimensional SOLA numerical algorithm to axisymmetric swirling flows [42]. Numerical results including the effects of turbulence are presented by Gupta and Lilley [8]. Turbulence is simulated via the "two-equations" (kinetic energy and dissipation of turbulence) model [43,44]. The solution is achieved utilizing the Imperial College steady-state numerical algorithm [45]. However, the solution obtained gives no better approximation of the flowfield than the present enhanced viscosity model. The reason being that the "two-equation" model is known to fail when sufficient streamline bending is present [46,47].

1.4 Summary of the Thesis and Findings

Investigations on simple vortex and vortex chamber flows are presented herein.

Based on the energy equation, simple vortex flows are shown to extremize the transient energy supply, and Helmholtz's minimum viscous dissipation is found to take place at the steady-state condition of the flowfield. The proof to the above is established via a first and/or a second variation of the energy supply integral.* The solid body rotation exhibited in Rankine's free-forced vortex is shown as an essential mechanism in minimizing the viscous energy dissipation in the field. The transient energy supply and total fluid frictional losses during the evolution of a forced vortex are investigated. A similar study concerning the decay of Rankine's vortex is included. Inviscid-potential and viscous-potential vortex flows are critically discussed.

Analytical, experimental and numerical investigations concerning the flows in a vortex chamber are presented. The point of maximum tangential velocity is established with the aid of energy and inviscid equations of motion. From this, calculations for the dimensionless pressure drop across the chamber and radial distribution, flow coefficient and the reverse flow radius near the exit are made possible. The analysis suggests and the experimental results confirm that none of the above fluid parameters depend on the absolute dimensions of the chamber.

Experimental velocity, save the radial velocity component, distributions inside the chamber for different axial stations and inlet volumetric flowrates are also presented. The experimental results

*to be defined in Chapter 2.

regarding the radial velocity component obtained with a five-hole pitot-probe are shown to be unreliable over most of the flowfield. The latter arises from the strong radial static pressure interference created by the fluid in its attempt to balance the centrifugal forces. For small contraction ratios vortex chambers, it was experimentally found that a considerable reduction in the static pressure drop across the chamber can be achieved by preventing the entrained flow at the exit to occur.

Finally, the extended two-dimensional swirling finite-difference solution procedure is used to numerically obtain the velocity map inside a high aspect ratio vortex chamber. The Marker and Cell (MAC) simulation and solution procedure was adopted. The Eulerian finite-difference formulation is presented using the primitive (pressure and velocity) dependent variables. At each time step, the time-marched expressions of the radial and axial velocity components are substituted into the continuity equation for each cell, and the guess-and-correct iterative process on pressure and velocity corrections are performed until the incompressibility condition is sufficiently well satisfied. The numerically obtained solutions show the velocity profiles on several axial and radial stations. The inviscid-potential solution is achieved solving the streamfunction equation via a successive overrelaxation procedure. Differences between the fully viscous and inviscid flowfield solutions are outlined.

The dominance of the end plate boundary layers over the main chamber flow, known from previous experiments, is evident in the present numerical simulations. Similarily, the tangential velocity peaks near the top and bottom plates and the axial velocity reversal, midway on the radius of the chamber are also present in the numerical results.

CHAPTER 2

SIMPLE VORTEX FLOWS

CHAPTER 2

SIMPLE VORTEX FLOWS

2.1 The Principle of Least Action

Quite often a higher level of understanding concerning a physical phenomenon can be provided via a variational analysis. In 1869, Helmholtz [48], following Leonard Euler's principle of the "Least Action", has shown that the fluid motion in a steady, incompressible and isoviscous field minimizes the rate of viscous dissipation. His proof demanded that the velocities must be specified on the boundaries, all the external forces are zero and the fluid must have a slow motion. However, under the assumption of a single valued second derivative of the velocities, Rayleigh [49] has indicated that it is not necessary for the theorem to be restricted to slow fluid motions.

In this Chapter, the variational principle is applied to simple vortex flows which are generated by viscous diffusion. Secondary fluid motion effects, a common occurance in these flows, [50,51] are not to be considered here. It will be shown that the fluid motion in such fields extremizes the energy supply, whereby the minimum dissipation is taking place at the steady state. The solid body rotation exhibited in Rankine's vortex will be shown as an essential mechanism to minimize the energy dissipation within the field. Finally, the transient energy supply and/or viscous dissipation in simple vortex flows will be investigated.

2.2 The Equations of Motion for Axisymmetric Swirling Flows

The equations which describe the fluid motion in an axisymmetric, incompressible, isothermal and isoviscous field, in cylindrical

coordinates, are:

radial-momentum

$$\frac{\partial V_r}{\partial t} + V_r \frac{\partial V_r}{\partial r} + V_z \frac{\partial V_r}{\partial z} - \frac{V_\theta^2}{r} = -\frac{1}{\rho}\frac{\partial P}{\partial r} + \nu\left(\nabla^2 V_r - \frac{V_r}{r^2}\right) \qquad (2.2.1)$$

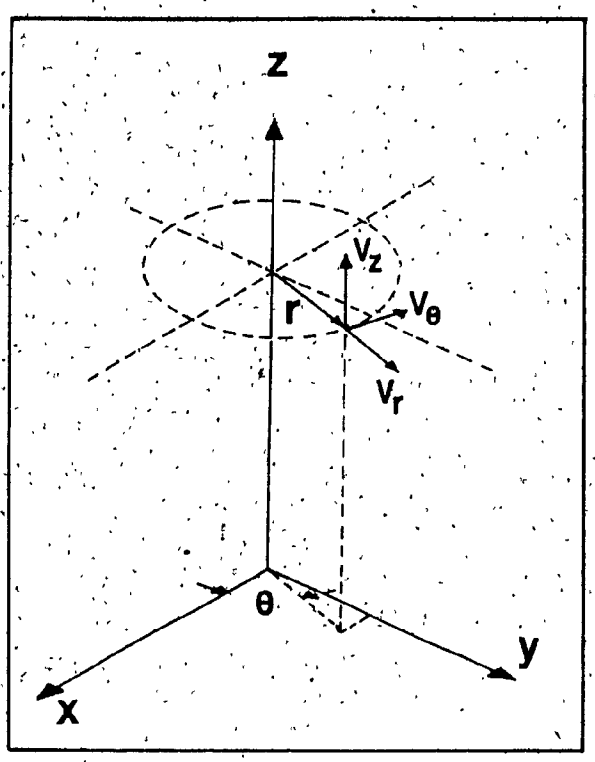

Fig. 2.2.1: Coordinate System

tangential-momentum

$$\frac{\partial V_\theta}{\partial t} + V_r \frac{\partial V_\theta}{\partial r} + V_z \frac{\partial V_\theta}{\partial z} + \frac{V_r V_\theta}{r} = \nu\left(\nabla^2 V_\theta - \frac{V_\theta}{r^2}\right) \qquad (2.2.2)$$

axial-momentum

$$\frac{\partial V_z}{\partial t} + V_r \frac{\partial V_z}{\partial r} + V_z \frac{\partial V_z}{\partial z} = -\frac{1}{\rho}\frac{\partial P}{\partial z} + \nu \nabla^2 V_z \qquad (2.2.3)$$

continuity

$$\frac{\partial V_r}{\partial r} + \frac{V_r}{r} + \frac{\partial V_z}{\partial z} = 0 \qquad (2.2.4)$$

where,

$$\nabla^2 = \frac{\partial^2}{\partial r^2} + \frac{1}{r}\frac{\partial}{\partial r} + \frac{\partial^2}{\partial z^2}$$

The energy equation neglecting the potential energy is,

$$\frac{dE_s}{dt} + \frac{1}{2}\rho \iiint_{\forall} \frac{D(q^2)}{Dt}\, d\forall = -\mathring{F} - \oiint_S P\, \vec{q} \circ \vec{n}\, ds \qquad (2.2.5)$$

where

$$\mathring{F} = \iiint_{\forall} \mathring{\Phi}\, d\forall \qquad (2.2.6)$$

The rate of viscous dissipation per unit volume $\mathring{\Phi}$ is [52],

$$\mathring{\Phi} = 2\mu \left[\left(\frac{\partial V_r}{\partial r}\right)^2 + \left(\frac{V_r}{r}\right)^2 + \left(\frac{\partial V_z}{\partial z}\right)^2 + \frac{1}{2}\left(\frac{\partial V_\theta}{\partial r} - \frac{V_\theta}{r}\right)^2 \right.$$

$$\left. + \frac{1}{2}\left(\frac{\partial V_\theta}{\partial z}\right)^2 + \frac{1}{2}\left(\frac{\partial V_r}{\partial z} + \frac{\partial V_z}{\partial r}\right)^2 \right] \qquad (2.2.6a)$$

Lamb [53] gives $\mathring{F}$ in the more general form,

$$\mathring{F} = \mu \iiint_{\forall} (\text{curl } \vec{q})^2\, d\forall + \mu \oiint_S \left\{ \frac{\partial \vec{q}^2}{\partial n} - 2(\vec{q} \times \text{curl } \vec{q}) \circ \vec{n} \right\} ds \qquad (2.2.7)$$

where the unit vector $\vec{n}$ is drawn outwards to the control surface. The coordinate system is shown in Fig. (2.2.1).

2.3 A Variational Principle

The most elementary form of vortex flows can be obtained by considering the motions of fluid about the z-axis, which are generated by the unsteady rotation of the infinite concentric cylinders of Fig. (2.3.1). Assuming that the azimuthal velocity is the only one existing in the regions $[0,R_i^-]$, $[R_i^+,R_o^-]$ or $[R_o^+,\infty)^*$, the equations (2.2.1) to (2.2.4) reduce to,

$$\frac{V_\theta^2}{r} = \frac{1}{\rho}\frac{\partial P}{\partial r} \tag{2.3.1a}$$

and

$$\frac{\partial V_\theta}{\partial t} = \nu\left(\frac{\partial^2 V_\theta}{\partial r^2} + \frac{1}{r}\frac{\partial V_\theta}{\partial r} - \frac{V_\theta}{r^2}\right) \tag{2.3.1}$$

The energy equation in any of the above regions, under the same assumptions from Eqs. (2.2.5) and (2.2.6) is,

$$\dot{E}_s = -2\pi\int_{R_1}^{R_2}\left\{\rho V_\theta\frac{\partial V_\theta}{\partial t} + \mu\left(\frac{\partial V_\theta}{\partial r} - \frac{V_\theta}{r}\right)^2\right\}r\,dr \tag{2.3.2}$$

where,

$$(R_1,R_2) = \begin{cases} (0,R_i^-) & \text{for the flow inside the inner cylinder} \\ (R_i^+,R_o^-) & \text{for the fluid bounded by the inner and outer cylinders} \\ (R_o^+,\lim r=\infty) & \text{for the fluid outside the outer cylinder.} \end{cases}$$

*Minus and plus superscripts indicate convex and concave surfaces respectively. Also $R_i^+ - R_i^- = R_o^+ - R_o^- = 0$.

If the solution of $V_\theta(t,r)$ can be expressed by,

$$V_\theta = T(t)\ R(r)$$

then Eq. (2.3.2) becomes,

$$E_s^\circ = -2\pi \int_{R_I}^{R_2} f(r;R,R')\ dr \qquad (2.3.3)$$

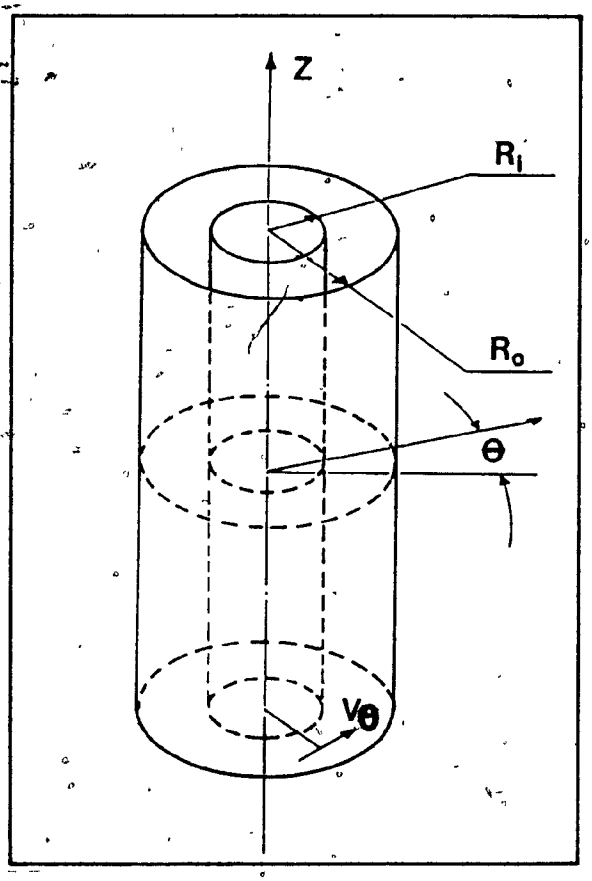

Fig. 2.3.1: Schematic of the Problem

where,

$$f(r,R,R') = \left[\rho R^2 T \frac{\partial T}{\partial t} + \mu T^2 \left(\frac{\partial R}{\partial r} - \frac{R}{r}\right)^2\right] r$$

If $\overset{\circ}{E}_s$ is to be an extremum then Euler-Lagrange equation, provides the necessary condition:

$$\frac{\partial f}{\partial R} - \frac{d}{dr}\left(\frac{\partial f}{\partial R'}\right) = 0 \tag{2.3.4}$$

In addition R and $R' \equiv \frac{\partial R}{\partial r}$ must both be continuous functions of the radius in $[R_1, R_2]$, and f must also be continuous and possess continuous derivatives of the first and second orders in the same interval [54,55]. Then from eq. (2.3.4) we have,

$$R\frac{\partial T}{\partial t} = \nu T\left(\frac{\partial^2 R}{\partial r^2} + \frac{1}{r}\frac{\partial R}{\partial r} - \frac{R}{r^2}\right)$$

or

$$\frac{\partial V_\theta}{\partial t} = \nu\left(\frac{\partial^2 V_\theta}{\partial r^2} + \frac{1}{r}\frac{\partial V_\theta}{\partial r} - \frac{V_\theta}{r^2}\right)$$

which is identical with eq. (2.3.1). The latter clearly shows that the fluid motions of this kind conserve the azimuthal momentum and simultaneously extremize $\overset{\circ}{E}_s$.

At steady-state of the flowfield

$$\overset{\circ}{E}_s = -\overset{\circ}{F}$$

where,

$$\overset{\circ}{F} = 2\pi\mu\int_{R_1}^{R_2}\left(\frac{dV_\theta}{dr} - \frac{V_\theta}{r}\right)^2 r\,dr \tag{2.3.5}$$

Therefore, when the transient effects diminish, the dissipation in the flowfield attains an extreme value. The second variation from Appendix A of eq. (2.3.5) is,

$$\left.\frac{d^2\overset{\circ}{F}(\varepsilon)}{d\varepsilon^2}\right|_{\varepsilon=0} = \int_{R_1}^{R_2} \left\{ \frac{\partial^2 G}{\partial V_\theta^2} (\eta(r))^2 + 2 \frac{\partial^2 G}{\partial V_\theta \partial V'_\theta} \eta'(r)\eta(r) + \frac{\partial^2 G}{\partial V_\theta'^2} (\eta'(r))^2 \right\} dr \tag{2.3.6}$$

where,

$$G = 2\pi\mu \left(\frac{dV_\theta}{dr} - \frac{V_\theta}{r} \right)^2 r \tag{2.3.7}$$

$\eta(r)$ is a function of r with continuous derivatives in $[R_1, R_2]$ and vanishes at the boundaries, while ε is a small parameter. Integration by parts of the second terms of the integral gives,

$$\int_{R_1}^{R_2} 2 \frac{\partial^2 G}{\partial V_\theta \partial V'_\theta} \eta'(r)\eta(r)\, dr = \frac{\partial^2 G}{\partial V_\theta \partial V'_\theta} (\eta(r))^2 \Big|_{R_1}^{R_2} - \int_{R_1}^{R_2} \frac{d}{dr} \left(\frac{\partial^2 G}{\partial V_\theta \partial V'_\theta} \right) (\eta(r))^2 dr \tag{2.3.8}$$

Then the second variation of the integral (2.3.6) becomes,

$$\left.\frac{d^2\overset{\circ}{F}(\varepsilon)}{d\varepsilon^2}\right|_{\varepsilon=0} = \int_{R_1}^{R_2} \left\{ \left[\frac{\partial^2 G}{\partial V_\theta^2} - \frac{d}{dr} \left(\frac{\partial^2 G}{\partial V_\theta \partial V'_\theta} \right) \right] (\eta(r))^2 + \frac{\partial^2 G}{\partial V_\theta'^2} (\eta'(r))^2 \right\} dr \tag{2.3.9}$$

Utilization of eq. (2.3.7), and eq. (2.3.9) leads to the sufficient condition,

$$\left.\frac{d^2\overset{\circ}{F}(\varepsilon)}{d\varepsilon^2}\right|_{\varepsilon=0} = 4\pi\mu \int_{R_1}^{R_2} \left\{\frac{(\eta(r))^2}{r} + r(\eta'(r))^2\right\} dr \qquad (2.3.10)$$

The integral in (2.3.10) is always positive. Hence, at steady-state the viscous dissipation in the field is minimum as Helmholtz has also shown in an alternate way.

2.4 The Forced Vortex

A stationary cylindrical vessel containing a stationary fluid is suddenly forced to rotate with a constant angular velocity. The fluid is expected to acquire a solid body rotation asymptotically as time goes to infinity. This expectation as Lord Rayleigh [49] points out is based on experiment rather than theory.

Originally, the fluid and vessel are motionless, the dissipation is zero and the least dissipation principle is satisfied. When the vessel is suddenly set in motion, a tangential velocity modification of the fluid due to non-slip condition at the wall is inevitable. As the "disturbance" at the wall is diffused inward by the viscosity, the fluid motion is changed in such a way as to reach an alternate level with minimum dissipation. In the process, the gradual alteration of the velocity is achieved through profiles which extremize the rate of energy supply.

Let us now consider the following situation: the fluid inside the cylinder $r = R_0$, depicted in Fig. (2.4.1) is rotating with a constant angular velocity ω_I (with $R_i = 0$). Suddenly, the container is forced to rotate, by an external agent, at another velocity ω_F. The equation governing the motion is (2.3.1). A solution of this equation for $\omega_I = 0$ is given

by Batchelor [56]. For the present with $\omega_I \neq 0$, the velocity is given by,

$$V_\theta(t,r) = \frac{V_{\theta F}}{R_o} r + 2(V_{\theta F} - V_{\theta I}) \sum_{n=1}^{\infty} \frac{J_1\left(\alpha_n \frac{r}{R_o}\right)}{\alpha_n J_o(\alpha_n)} e^{-\left(\frac{\alpha_n}{R_o}\right)^2 \nu t} \qquad (2.4.1)$$

where the α_n's are the roots of the Bessel function J_1. The above solution was obtained utilizing the convenient transformation,

$$\tilde{V}_\theta(t,r) = \frac{V_{\theta F}}{R_o} r - V_\theta(t,r)$$

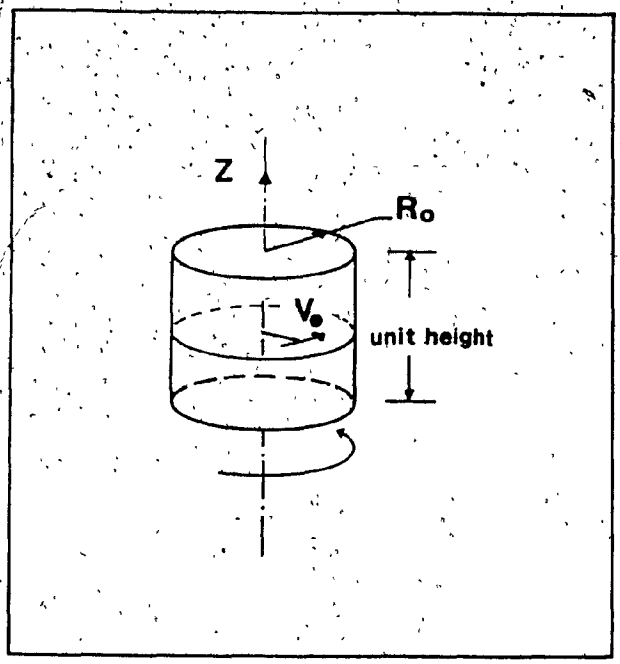

Fig. 2.4.1: The Cylindrical Vessel

The transformed velocity $\tilde{V}_\theta$ is simply the velocity of the fluid, viewed by an observer from a frame of reference rotating with the angular velocity of the cylinder $\omega_F = \frac{V_{\theta F}}{R_o}$. In figures (2.4.2) and (2.4.3) the time history profiles of V_θ are given for ω_I equal to zero and 0.5 ω_F respectively.

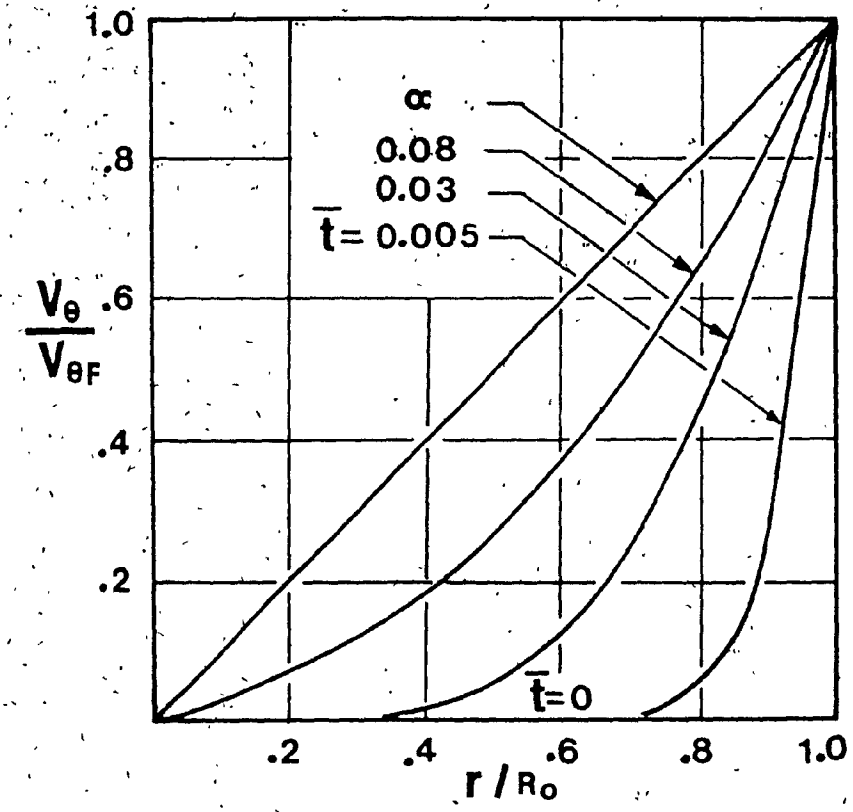

Fig. 2.4.2: Velocity Profiles During Spin-Up with ω_I = o

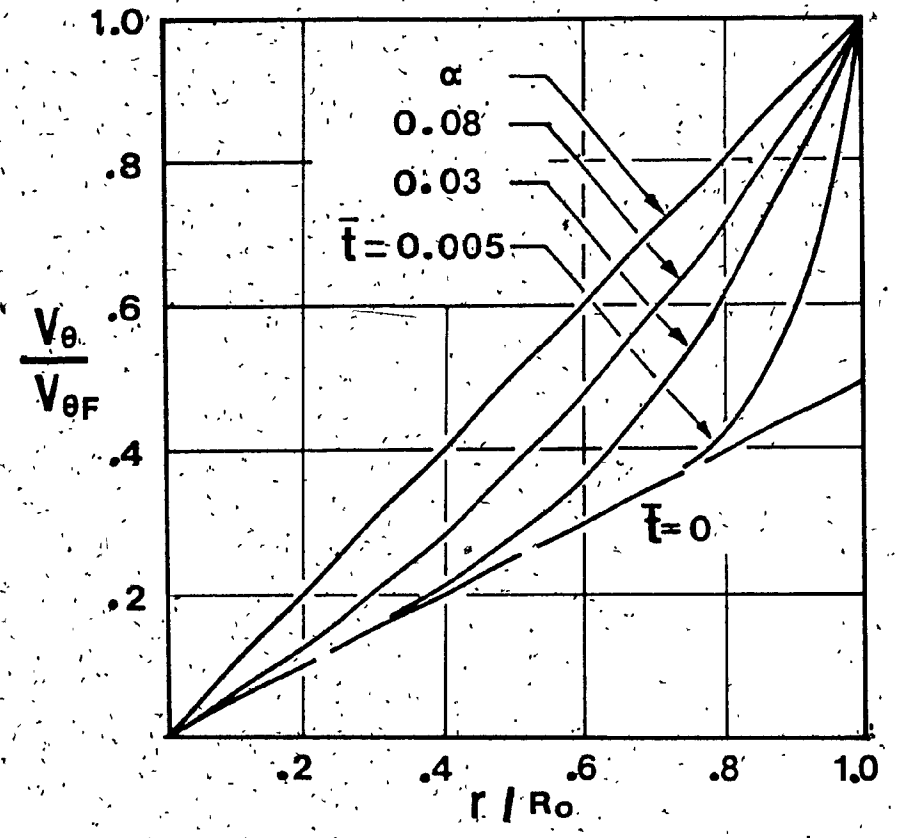

Fig. 2.4.3: Velocity Profiles During Spin-Up with $\omega_I = \frac{1}{2}\omega_F$

The energy equation for the motion from eq. (2.2.5) is,

$$\frac{dE_s}{dt} = -\left\{\frac{\partial T}{\partial t} + \mathring{F}\right\} \qquad (2.4.2)$$

where,

$$T = \frac{1}{2}\rho \iiint_{\Psi} V_\theta^2 \, d\Psi \qquad (2.4.2a)$$

$$\mathring{F} = \mu \iiint_{\Psi} \left[\frac{\partial V_\theta}{\partial r} - \frac{V_\theta}{r}\right]^2 d\Psi \qquad (2.4.2b)$$

and

$$\frac{dE_s}{dt} = -2\pi R_o V_{\theta F} \tau_{r\theta}\Big|_{r=R_o} \qquad (2.4.2c)$$

From eq. (2.4.1), eq. (2.4.2a) becomes,

$$\hat{T} = \pi\rho \int_0^{R_o} \left\{ \left(\frac{V_{\theta F}}{R_o}\right)^2 r^2 + 4\frac{V_{\theta F}}{R_o} r(V_{\theta F} - V_{\theta I}) \sum_{n=1}^{\alpha} \frac{J_1\left(\alpha_n \frac{r}{R_o}\right)}{\alpha_n J_o(\alpha_n)} e^{-\left(\frac{\alpha_n}{R_o}\right)^2 \nu t} \right.$$

$$\left. + 4(V_{\theta F} - V_{\theta I})^2 \sum_{n=1}^{\infty}\sum_{m=1}^{\infty} \frac{J_1\left(\alpha_n \frac{r}{R_o}\right) J_1\left(\alpha_m \frac{r}{R_o}\right)}{\alpha_n \alpha_m J_o(\alpha_n) J_o(\alpha_m)} e^{-\frac{\alpha_n^2 + \alpha_m^2}{R_o^2}\nu t} \right\} r\,dr$$

Then,

$$\frac{\partial \hat{T}}{\partial t} = -4\pi\mu \left\{ \frac{V_{\theta F}}{R_o^3}(V_{\theta F} - V_{\theta I}) \sum_{n=1}^{\infty} \frac{\alpha_n}{J_o(\alpha_n)} e^{-\left(\frac{\alpha_n}{R_o}\right)^2 \nu t} \int_0^{R_o} r^2 J_1\left(\alpha_n \frac{r}{R_o}\right) dr \right.$$

$$+ \frac{(V_{\theta F} - V_{\theta I})^2}{R_o^2} \sum_{n=1}^{\infty}\sum_{m=1}^{\infty} \frac{\left(\frac{\alpha_n}{\alpha_m} + \frac{\alpha_m}{\alpha_n}\right)}{J_o(\alpha_n) J_o(\alpha_m)} e^{-\frac{\alpha_n^2 + \alpha_m^2}{R_o^2}\nu t}$$

$$\left. \cdot \int_0^{R_o} r\, J_1\left(\alpha_n \frac{r}{R_o}\right) J_1\left(\alpha_m \frac{r}{R_o}\right) dr \right\}$$

Utilizing the results (B.12) and (B.14) from the appendix B we have,

$$\frac{\partial T}{\partial t} = 4\pi\mu \left\{ V_{\theta F}(V_{\theta F} - V_{\theta I}) \sum_{n=1}^{\infty} e^{-\left(\frac{\alpha_n}{R_o}\right)^2 \nu t} - (V_{\theta F} - V_{\theta I})^2 \sum_{n=1}^{\infty} e^{-2\left(\frac{\alpha_n}{R_o}\right)^2 \nu t} \right\} \tag{2.4.3}$$

From eq. (2.4.1), eq. (2.4.2b) gives,

$$\mathring{F} = 8\pi\mu\ (V_{\theta F} - V_{\theta I})^2 \sum_{n=1}^{\infty} \sum_{m=1}^{\infty} \frac{1}{\alpha_n \alpha_m J_o(\alpha_n)\ J_o(\alpha_n)} \left\{ \int_o^{R_o} \left[\frac{\partial J_1\left(\alpha_n \frac{r}{R_o}\right)}{\partial r} - \frac{J_1\left(\alpha_n \frac{r}{R_o}\right)}{r} \right] \left[\frac{\partial J_1\left(\alpha_m \frac{r}{R_o}\right)}{\partial r} - \frac{J_1\left(\alpha_m \frac{r}{R_o}\right)}{r} \right] r\,dr \right\} e^{-\frac{\alpha_n^2 + \alpha_m^2}{R_o^2} \nu t}$$

Utilizing the result given in eq. (B.18) (see Appendix B), yields,

$$\mathring{F} = 4\pi\mu\ (V_{\theta F} - V_{\theta I})^2 \sum_{n=1}^{\infty} e^{-2\left(\frac{\alpha_n}{R_o}\right)^2 \nu t} \tag{2.4.4}$$

Incorporating eqs. (2.4.3) and (2.4.4) into eq. (2.4.2) gives,

$$\frac{dE_s}{dt} = -4\pi\mu\ V_{\theta F}(V_{\theta F} - V_{\theta I}) \sum_{n=1}^{\infty} e^{-\left(\frac{\alpha_n}{R_o}\right)^2 \nu t} \tag{2.4.5}$$

The same equation can be derived using eqs. (2.4.2c) and (2.4.1).

From the equations (2.4.3), (2.4.4) and (2.4.5), it can be seen that during vortex growth ($\omega_F > \omega_I$), part of the supplied power will go to

dissipation and the rest will increase the kinetic energy of the fluid. On the other hand, if $\omega_F < \omega_I$, and $\omega_F \neq 0$, a portion of the kinetic energy will transform into heat by viscous dissipation. The other part of the kinetic energy will be transferred as mechanical work from the fluid to the cylinder. At this point however, one must be cautious in drawing any further conclusions concerning the value of the mechanical energy which can be utilized during the vortex decay. The reason is, that the angular momentum of the rotating fluid is not a monotonically increasing function of the radius for $o < t < \infty$, thereby a secondary flow is possible [51]. This secondary flow will indeed diminish with time as the stationary profile of the velocity is approached [49]. Nevertheless, during the transient process, the secondary flow will increase the viscous dissipation and thus reduce the mechanical energy which can be transferred by the fluid to the cylinder.

For vortex growth, the angular momentum of the fluid is a monotonically increasing function of the radius for any time level, and no secondary flow may exist. For this case the total energy dissipated during the vortex growth can be obtained by time integration of eq. (2.4.4),

$$F_T = 4\pi\mu(V_{\theta F} - V_{\theta I})^2 \sum_{n=1}^{\infty} \lim_{t_F \to \infty} \int_o^{t_F} e^{-2\left(\frac{\alpha_n}{R_o}\right)^2 \nu t} \, dt$$

or

$$F_T = 2\pi\rho(V_{\theta F} - V_{\theta I})^2 R_o^2 \sum_{n=1}^{\infty} \frac{1}{\alpha_n^2} \qquad (2.4.6)$$

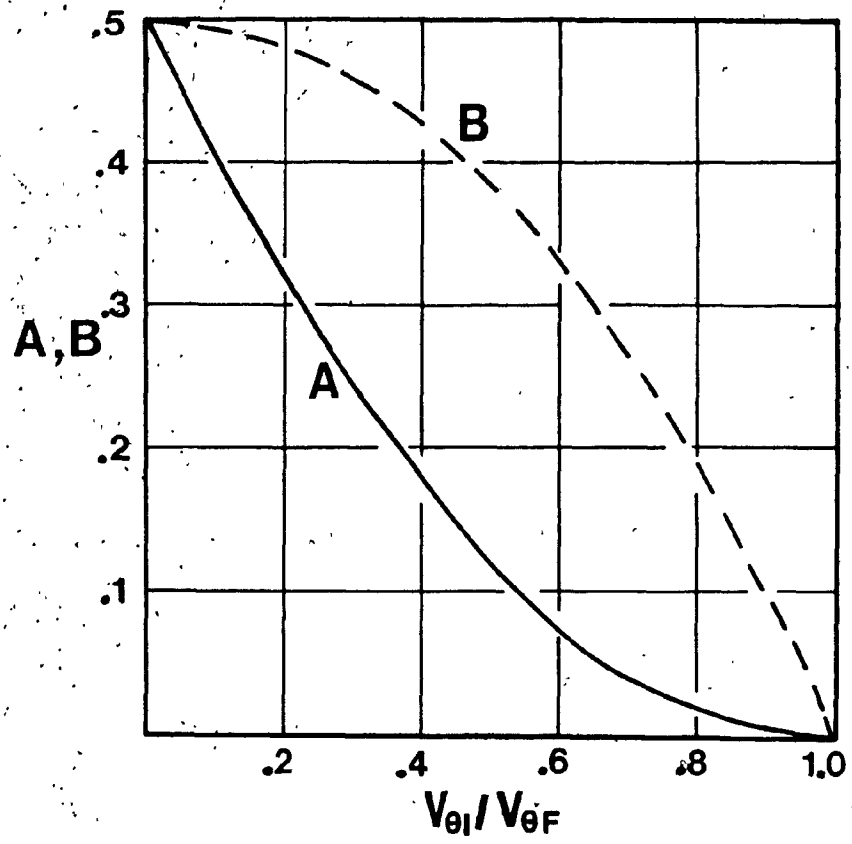

Fig. 2.4.4: Dimensionless Viscous Dissipation and Change of Kinetic Energy vs $V_{\theta I}/V_{\theta F}$ for the Spin-up Process

($A = -F_T/\frac{1}{2}\ \rho\pi R_o^2 V_{\theta F}^2$, $B = \delta T/\frac{1}{2}\ \rho\pi R_o^2 V_{\theta F}^2$).

where the α_n's are given by [57],

$$\alpha_n \doteq \pi \left[n + 0.25 - \frac{0.151982}{(4n+1)} + \frac{0.015399}{(4n+1)^3} - \frac{0.245270}{(4n+1)^5} \right] \qquad (2.4.7)$$

The infinite series in eq. (2.4.6) was found to have a value of 0.125. The convergence was established by comparison to the greater infinite series,

$$\sum_{n=1}^{\infty} \frac{1}{n^2}$$

which can be easily shown to be convergent via the integral test [58].

The total energy supply required for the vortex to grow from a lower solid body rotation (ω_I) level to a higher one, is found through integration of eq. (2.4.5) to be,

$$\delta E_S = -\frac{1}{2} \rho \pi R_o^2 V_{\theta F}^2 \left[1 - \left(\frac{V_{\theta I}}{V_{\theta F}} \right)^2 \right]$$

Figure (2.4.4) shows the overall distributions of viscous dissipation and change in kinetic energy. When $V_{\theta I}$ is zero, or the flowfield starts from rest, the total dissipation during the process is equal to the final kinetic energy of the field. The total energy which must be supplied is twice the total dissipation. From the same figure, when $V_{\theta F} = V_{\theta I}$, which implies no change of the flowfield, both dissipation and change in kinetic energy are equal to zero. For values of $V_{\theta I}/V_{\theta F}$ in (0,1), the required energy supply is obtained by the addition of curves A and B of Fig. (2.4.4). The result is depicted in Fig. (2.4.5) and shows a linear relation of the energy supply vs. $V_{\theta I}/V_{\theta F}$. When $V_{\theta F} = 0$, which corresponds to a sudden halt of the vessel, δE_S is zero and the total initial kinetic energy is

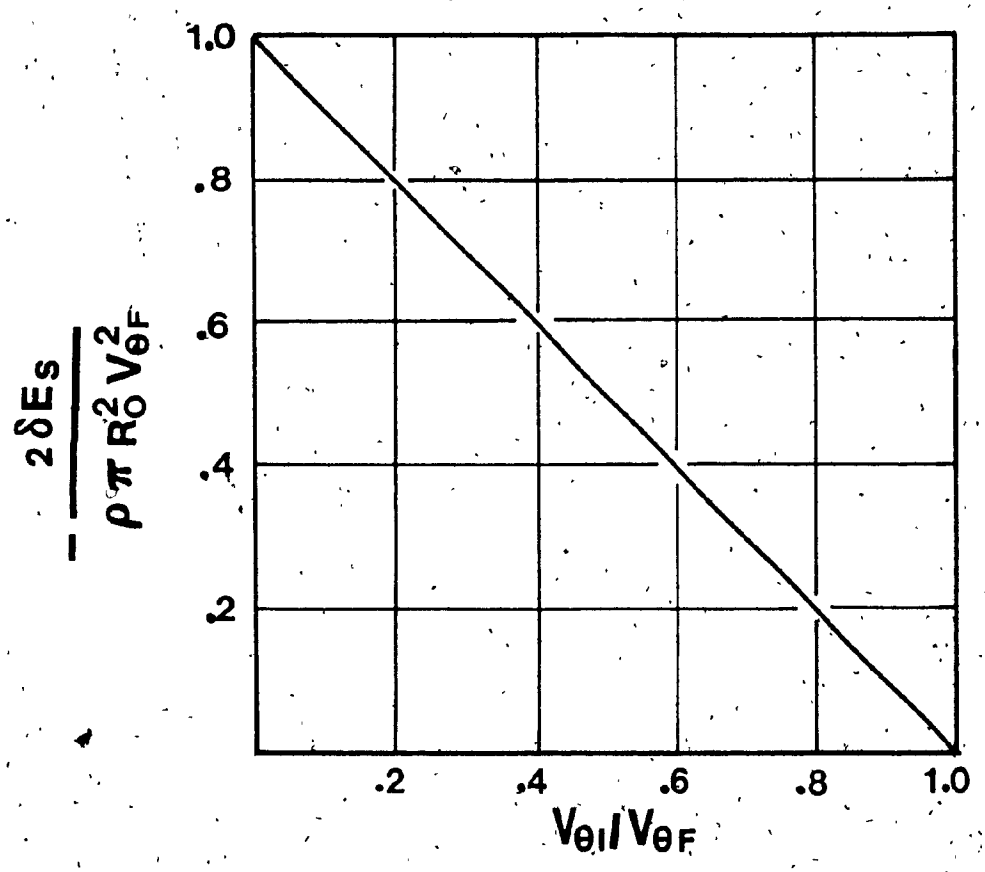

Fig. 2.4.5: Dimensionless Energy Supply vs. $V_{\theta I}/V_{\theta R}$ for the Spin-Up Process.

forced to be converted into heat by the viscous forces. For this case the existance of secondary flow is immaterial, as far as the gross effects are concerned, since F_T is equated to a point function i.e. $\delta(T)$.

At this point it will be a serious omission if the following observation escapes without it being questioned. At the steady state condition, the evolved flowfield is a rotational one. However, from eqs. (2.2.6a) and (2.2.6) the viscous dissipation is zero. The reason for such behaviour can be clearly understood if the phenomenon is viewed on the frame of reference, rotating with the angular velocity $(V_{\theta o}/R_o)$ of the cylinder. Under the required transformation,

$$\tilde{V}_\theta = V_\theta - \frac{V_{\theta o}}{R_o} r \qquad (2.4.8)$$

the steady equation of motion (2.3.1a) and (2.3.1) become respectively

$$\frac{\partial P}{\partial r} = \rho \left(\frac{V_{\theta o}}{R_o}\right)^2 r \qquad (2.4.9)$$

and

$$\frac{\partial^2 \tilde{V}_\theta}{\partial r^2} + \frac{1}{r}\frac{\partial \tilde{V}_\theta}{\partial r} - \frac{\tilde{V}_\theta}{r^2} = 0 \qquad (2.4.10)$$

The general solution of eq. (2.4.10) is,

$$\tilde{V}_\theta = A'r + \frac{B'}{r}$$

Application of the boundary conditions i.e. $\tilde{V}_\theta(r=0) = \tilde{V}_\theta(r=R_o) = 0$, yields,

$$\tilde{V}_\theta = 0$$

Therefore, the rotational flowfield, seen from the "absolute" frame, is nothing else but a hydrostatic flowfield in the relative frame of

reference. Since there is no relative motion among the fluid and the cylindrical vessel, there may exist no dissipation. From eq. (2.4.9), the centrifugal acceleration, produces fluid strata with varying hydrostatic pressure levels. The same phenomenon, i.e. no dissipation, is also true for a fluid enclosed by a vessel undergoing pure translation. Because those two fluid motions (solid body rotation and translation) are the only ones known at the present to produce no viscous dissipation [53], we can conclude that, viscous dissipation is absent in viscous flowfields, where under a permissible coordinate transformation, they become hydrostatic fields.

From the above it is elementary to deduct that the vorticity of the forced vortex, in the relative frame of reference, is equal to zero. It becomes obvious, if one studies the frame transformation equation of the vorticity, given by Robertson [4] as,

$$\text{Curl } \vec{q} = \text{curl } \vec{\tilde{q}} + 2\vec{\omega} \qquad (2.4.11)$$

where $\vec{q}$ and $\vec{\tilde{q}}$ are the fluid velocities in the "absolute" and relative frames of reference respectively, while $\vec{\omega}$ is the angular velocity of the moving frame. It can be seen from eq. (2.4.11) that, a rotational flow in the "absolute" frame of reference will be an irrotational flow in the relative frame, if and only if curl $\vec{q} = 2\vec{\omega}$. A clear example is the forced vortex.

2.5 The Potential Vortex

The potential vortex can have an inviscid or a viscous source of origin. The inviscid potential vortex owes its presence to the Coriolis acceleration $(V_r V_\theta / r)$ in eq. (2.2.2). The viscous potential vortex is developed and maintained by the viscous action of moving boundaries. The

difference between the two is that, in the former, the viscous energy dissipation vanishes while for the latter it does not. However, in both, the flow is irrotational and thereby the velocity vector can be represented by a scalar function Φ. The one to one correspondence of potential and non-viscous flows, often implied in some textbooks, is incorrect and must be clearly differentiated.

A vectorial form of eqs. (2.2.1) - (2.2.3) is,

$$\frac{\partial \vec{q}}{\partial t} + \vec{\nabla}\left(\frac{p}{\rho} + \frac{\vec{q}^2}{2}\right) + \vec{q} \times \text{curl}\, \vec{q} = \nu\, \vec{\nabla}^2 \vec{q} \qquad (2.5.1)$$

Utilization of the vector identity,

$$\vec{\nabla}^2 \vec{q} = \vec{\nabla}\, \text{div}\, \vec{q} - \text{curl}\,(\text{curl}\, \vec{q})$$

Equation (2.5.1) transforms to,

$$\frac{\partial \vec{q}}{\partial t} + \vec{\nabla}\left(\frac{p}{\rho} + \frac{\vec{q}^2}{2}\right) + \vec{q} \times \text{curl}\, \vec{q} = \nu\, [\vec{\nabla}\, \text{div}\, \vec{q} - \text{curl}(\text{curl}\, \vec{q})] \qquad (2.5.2)$$

The solenoidal character of the vector field demands that,

$$\text{div}\, \vec{q} = 0$$

and thereby eq. (2.5.2) reduces to,

$$\frac{\partial \vec{q}}{\partial t} + \vec{\nabla}\left(\frac{p}{\rho} + \frac{\vec{q}^2}{2}\right) + \vec{q} \times \text{curl}\, \vec{q} = -\nu\, \text{curl}(\text{curl}\, \vec{q}) \qquad (2.5.3)$$

The above vector equation can be easily seen to yield eqs. (2.2.1)-(2.2.3) utilizing the following relations,

$$\text{curl } \vec{q} = \frac{1}{r} \begin{vmatrix} \vec{e}_r & r\vec{e}_\theta & \vec{e}_z \\ \frac{\partial}{\partial r} & \frac{\partial}{\partial \theta} & \frac{\partial}{\partial z} \\ V_r & rV_\theta & V_z \end{vmatrix} \qquad (2.5.3a)$$

$$\text{curl}(\text{curl } \vec{q}) = \frac{1}{r} \begin{vmatrix} \vec{e}_r & r\vec{e}_\theta & \vec{e}_z \\ \frac{\partial}{\partial n} & \frac{\partial}{\partial \theta} & \frac{\partial}{\partial z} \\ \xi & r\eta & \zeta \end{vmatrix} \qquad (2.5.3b)$$

and

$$\vec{q} \times \text{curl } \vec{q} = \begin{vmatrix} \vec{e}_r & \vec{e}_\theta & \vec{e}_z \\ V_r & V_\theta & V_z \\ \xi & \eta & \zeta \end{vmatrix} \qquad (2.5.3c)$$

where,

$$\xi = \frac{1}{r}\frac{\partial V_z}{\partial \theta} - \frac{\partial V_\theta}{\partial z}, \quad \eta = \frac{\partial V_r}{\partial z} - \frac{\partial V_z}{\partial r} \qquad (2.5.3d)$$

and $$\zeta = \frac{\partial V_\theta}{\partial r} + \frac{V_\theta}{r} - \frac{1}{r}\frac{\partial V_r}{\partial \theta}$$

For an irrotational flow, curl $\vec{q}$ is zero and the velocity vector is given in terms of scalar function Φ,

$$\vec{q} = \vec{\nabla}\,\Phi \qquad (2.5.4)$$

Then eq. (2.5.3) reduces to,

$$\vec{\nabla}\left(\frac{\partial\Phi}{\partial t}+\frac{P}{\rho}+\frac{\vec{q}^2}{2}\right)=0$$

or

$$\frac{\partial\Phi}{\partial t}+\frac{P}{\rho}+\frac{\vec{q}^2}{2}=\pi(t)$$

At steady-state the above equation yields,

$$\frac{P}{\rho}+\frac{\vec{q}^2}{2}=\text{const.} \qquad (2.5.5)$$

which is the Bernoulli's equation. It has been therefore seen that, in an irrotational flow, the viscous shear terms drop out in the momentum equation. The latter suggests that potential flow is an exact solution of the Euler and Navier-Stokes equations provided the boundary conditions are also free of vorticity. The zero normal velocity on a solid or impermeable boundary gives no problem. However, the fulfilment of the tangential (to the boundary) velocity condition reduces the viscous potential solutions, to a small number of special problems. Prandtl and Tietjens [59] write on this aspect:

> "However, it is not possible to satisfy at the same time the two necessary boundary conditions, stating that the normal as the tangential velocity at a wall has to be zero".

Indeed, for the case where a relative motion exists between the irrotational fluid and solid wall the non-slip condition (i.e. "adherence" of the fluid to the solid body) cannot be achieved without vorticity. On the other hand, if the impermeable surface moves with the local tangential velocity of the irrotational flow, then the non-slip condition, i.e. zero relative velocity between the fluid and the boundary, is accomplished without the presence of vorticity. Examples of such special case problems

that meet both boundary conditions are: the flowfield about a rising spherical gas bubble in a stagnant fluid, critically analyzed by Zierep [50], and the viscous potential vortex which will be presented here.

Let us focus our attention on the viscous energy dissipation given by eq. (2.2.7). For the case of an irrotational flowfield, only the surface integral containing the gradient of the velocity vector, in a direction which is normal to the boundary survives. For an inviscid potential flow, the dissipation is zero since $\mu = 0$. However, for a potential flow where μ is different from zero, the dissipation does not vanish, and the surface integral containing the velocity gradient represents the overall power of the wall shear stress at the moving boundary [50].

a) The Inviscid Potential Vortex

Consider the inviscid steady flow within the two parallel discs depicted in Fig. (2.5.1). The fluid enters the flow-domain having a radial and tangential velocity components V_{ro} and $V_{\theta o}$ respectively. Because the distance d between the plates is very small, V_z can be taken as zero. Then the equations describing the flow are,

$$\frac{\partial(rV_r)}{\partial r} = 0$$

$$\zeta = 0$$

and $$\frac{p}{\rho} + \frac{(V_r^2 + V_\theta^2)}{2} = \text{const.}$$

The velocities are then given by,

$$V_r = -\frac{Q}{2\pi r d} \quad \text{and} \quad V_\theta = \frac{\Gamma}{2\pi r}$$

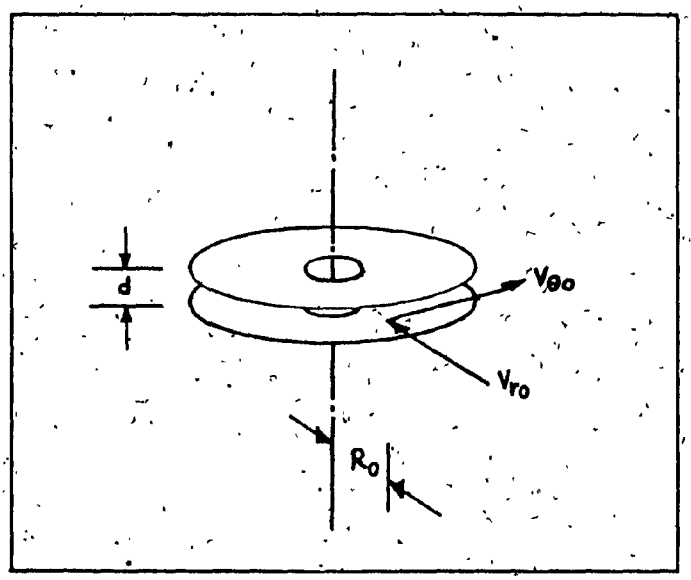

Fig. 2.5.1: Production of a Vortex Between Two Circular Parallel Plates with Small Spacing.

or, $\vec{q}$ is the superposition of two simple inviscid flows at the origin; a sink and a vortex. The pressure-velocity relation is given by the Bernoulli-equation. If the radial velocity is zero at the inlet, no inviscid potential vortex is possible. A V_{ro} equal to zero implies that a jet of "zero" thickness meets the inlet plane tangentially. The latter corresponds to the assumption that, the cylindrical surface rotates with a constant angular velocity $V_{\theta o}/R_o$. Since there is no viscosity, rotation cannot be "sensed" by the fluid inside the flow domain. It is therefore apparent that, if V_r is not present, inviscid potential vortex is theoretically not possible.

b) <u>The Viscous Potential Vortex</u>

Let us now focus our attention on the flowfield outside the cylinder $r = R_o$ shown in Fig. (2.3.1). The cylinder and the fluid are originally at rest. Suddenly the cylinder is forced to rotate with a constant

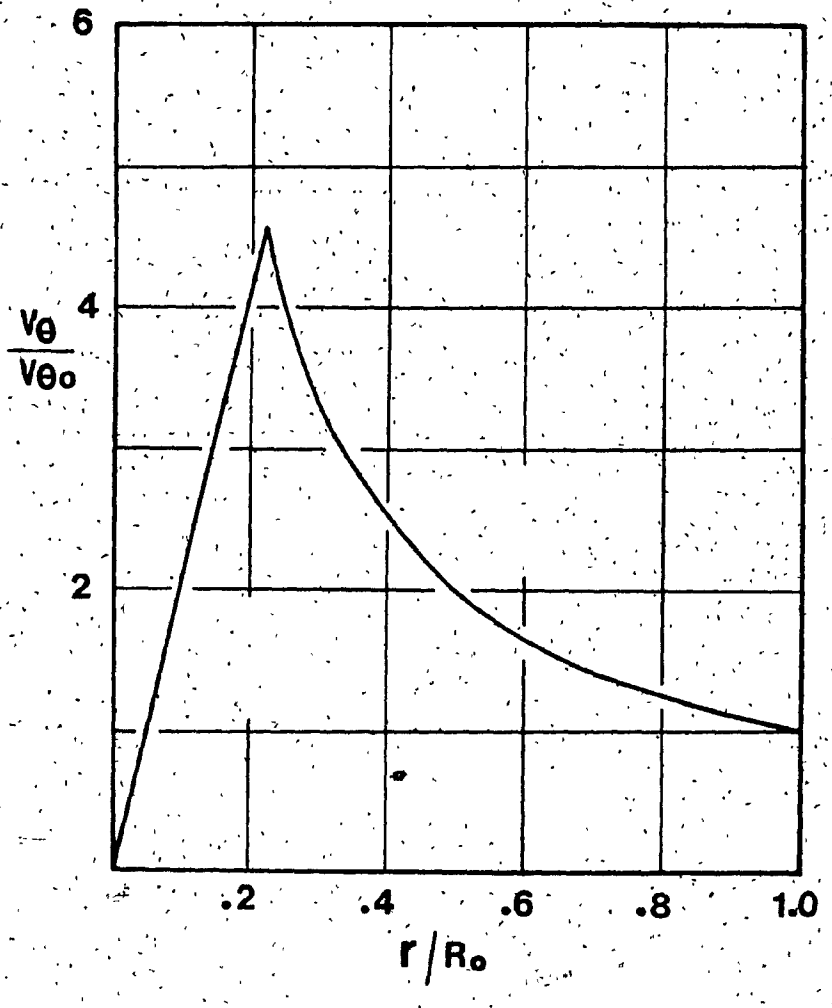

Fig. 2.6.1: The Rankine's Vortex

angular velocity. Under the viscous shear stresses, the fluid velocity is continuously modified until it reaches asymptotically a level where $\mathring{F}$ is zero. Although the vorticity is different from zero during the evolution, it is zero in the limiting case when the transient effects vanish.

It is a simple matter to show from either eq. (2.2.6) or eq. (2.2.7) that the viscous rate of energy dissipation for the viscous potential fluid motion inside the infinite flow domain, is equal to $4\pi\mu V_{\theta o}^2$.

2.6 The Rankine's Vortex

If we focus our attention on the regions $[0,R_i^-]$ and $[R_i^+,R_o^-]$ and assume that,

$$V_{\theta o}R_o = V_{\theta i}R_i$$

at steady-state, then as Fig. (2.6.1) illustrates, the Rankines vortex is obtained. The solid body rotation gives a zero dissipation. However, in the region $[R_i^+, R_o^-]$, the rate of viscous energy dissipation from eq. (2.2.6) is,

$$\mathring{F} = 4\pi\mu\,(V_{\theta i}^2 - V_{\theta o}^2)$$

The power supplied by an external agent to sustain the motion from eq. (2.2.5) is,

$$\mathring{E}_s = -4\pi\mu\,(V_{\theta i}^2 - V_{\theta o}^2)$$

Assume now that after the Rankine's vortex has been established, the inner cylinder is withdrawn without disturbing the flow. Immediately following this action the energy supplied by the inner cylinder is arrested. This results in an energy imbalance which causes the vortex to

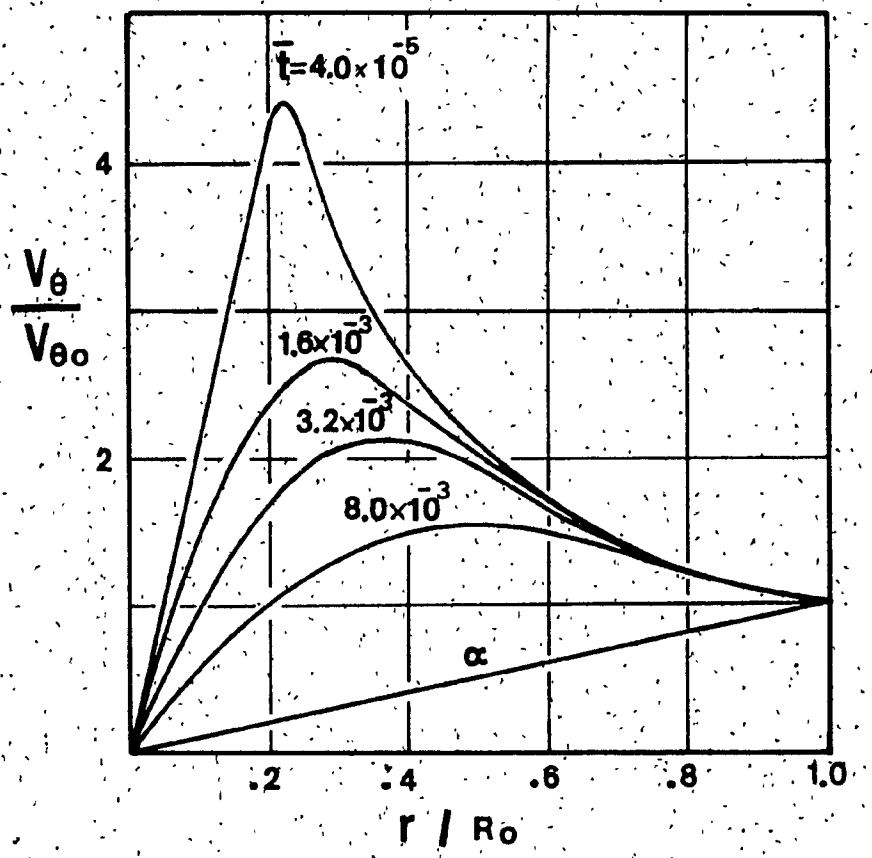

Fig. 2.6.2: Decay of Rankine's Vortex with $\bar{t} = t\nu/R_o^2$ and Free-Slip at $r = R_o$.

decay. The tangential velocity as a function of time elapsed after the inner cylinder is withdrawn, is given by the following equation which is derived in Appendix B.1,

$$\frac{V_\theta\left(t,\frac{r}{R_o}\right)}{V_{\theta o}} = \left(\frac{r}{R_o}\right) + 4\left(\frac{R_i}{R_o}\right)\sum_{n=1}^{\infty} \frac{J_1\left(\alpha_n \frac{R_i}{R_o}\right)}{\alpha_n^2 J_o^2(\alpha_n)} J_1\left(\alpha_n \frac{r}{R_o}\right) e^{-\left(\frac{\alpha_n}{R_o}\right)^2 \nu t} \tag{2.6.1}$$

As it can be seen from Fig. (2.6.2), the velocity is continuously modified. Eventually, the motion will attain the asymptotic stationary solution,

$$\frac{V_\theta}{V_{\theta o}} = \left(\frac{r}{R_o}\right)$$

In this condition $\overset{\circ}{F}$ and $\overset{\circ}{E}_S$ are both zero and no further change of the velocity is possible. If the inner cylinder is withdrawn and the outer cylinder is halted, then the vortex will decay according to,

$$\frac{V_\theta\left(t,\frac{r}{R_o}\right)}{V_{\theta o}} = 2\sum_{n=1}^{\infty}\left[\frac{2}{\alpha_n^2\left(\frac{R_i}{R_o}\right)}\frac{J_1\left(\alpha_n \frac{R_i}{R_o}\right)}{J_o^2(\alpha_n)} - \frac{1}{\alpha_n J_o(\alpha_n)}\right] \cdot J_1\left(\alpha_n \frac{r}{R_o}\right) e^{-\left(\frac{\alpha_n}{R_o}\right)^2 \nu t} \tag{2.6.2}$$

As indicated by Fig. (2.6.3) the tangential velocity for this case will reach the stationary condition,

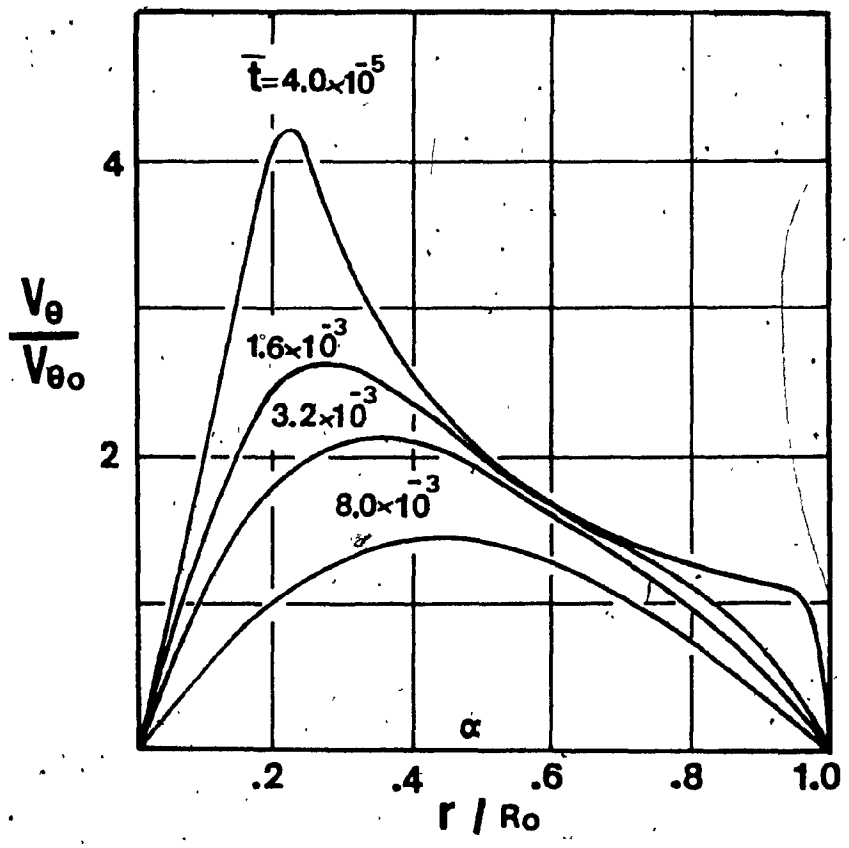

Fig. 2.6.3: Decay of Rankine's Vortex vs $\bar{t}$ with No-Slip at $r = R_o$.

$$\frac{V_\theta}{V_{\theta o}} = 0$$

For the flow described by the eq. (2.6.1), the energy supply and viscous dissipation can be obtained following the previous line of thought presented in Sec. 2.4. From eqs. (2.6.2) and (2.3.5), in the absence of secondary flow, the dimensionless cumulative energy dissipation during the decay of Rankine's vortex is,

$$\frac{F_{T,\bar{t}}}{T_{int}} = \frac{8}{1-4\ell n\left(\frac{R_i}{R_o}\right)} \sum_{n=1}^{\infty} \left[\frac{2}{\alpha_n^2 \left(\frac{R_i}{R_o}\right)} \cdot \frac{\dot{J}_1\left(\alpha_n \frac{R_i}{R_o}\right)}{\dot{J}_o(\alpha_n)} - \frac{1}{\alpha_n} \right]^2 \cdot \left(1 - e^{-2\alpha_n^2 \bar{t}}\right) \tag{2.6.3}$$

where,

$$\bar{t} = \frac{\nu t}{R_o^2}$$

and

$$T_{int} = \int_0^{R_o} \rho V_\theta^2(0,r)\, \pi r dr$$

Equation (2.6.3) is plotted in Fig. (2.6.4). At the start ($\bar{t} = 0^-$) the cumulative energy dissipation is zero. As time progresses $F_{T,\bar{t}}/T_{int}$ increases to a value of one, which is reached when $\bar{t} = \infty$, or when all the initial kinetic energy is converted into heat.

It is therefore evident that fluid motions, which are generated by the unsteady rotation of two concentric cylinders, extremizes the rate of energy supply, and the minimum viscous dissipation is only attained

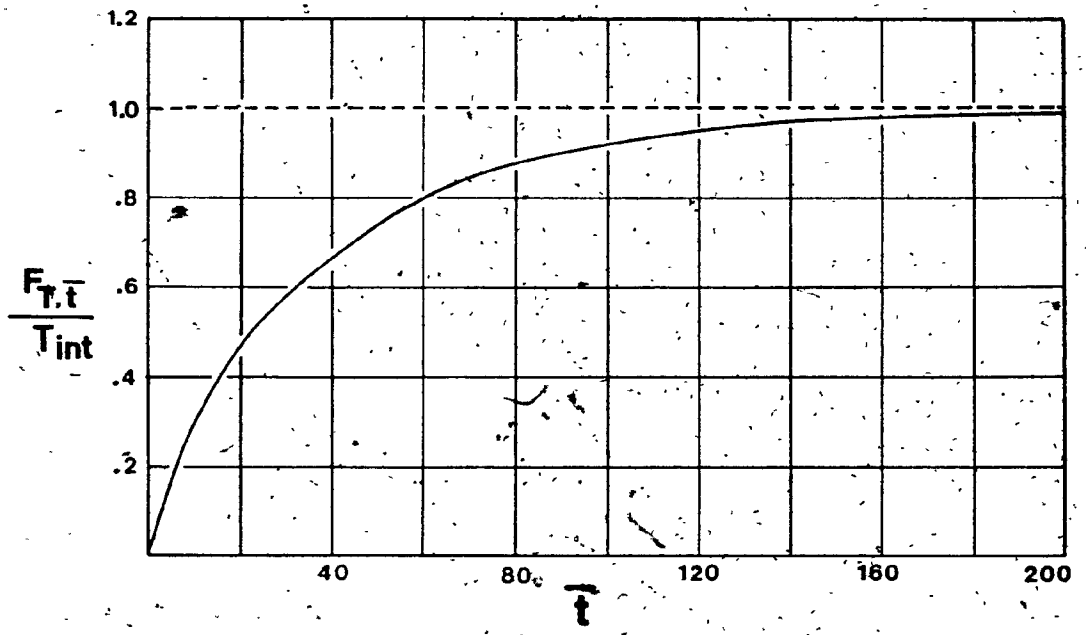

Fig. 2.6.4: Cumulative Dimensionless Viscous Dissipation During the Decay of a Confined Rankine Vortex.

at the steady-state condition of the field. The fluid bounded by a rotating cylinder can attain a profile resembling a free-forced vortex in the presence of an external source of energy, which in this case was generously provided by the inner cylinder. The sole rotation of the cylindrical vessel is not able to induce a Rankine's vortex profile since energy balance does not exist. It is also apparent that, the solid body rotation for the fluid motion resembling the Rankine's vortex, is essential for minimum viscous dissipation in the field.

CHAPTER 3

EXPERIMENTAL APPARATUS AND PROCEDURE

CHAPTER 3

EXPERIMENTAL APPARATUS AND PROCEDURE

3.1 Experimental Facility for Vortex Chamber Flows

The present experiments have been conducted in Concordia's isothermal cyclone chamber test facility which is schematically illustrated in Fig. (3.1.1). Air from the main supply passes through two rotameters (A and B) which are connected in parallel. Before the air expands into the main chamber, the static pressure difference, $\Delta P = P_{in} - P_a$, is recorded with the aid of an inclined manometer, C. The velocity map inside the chamber is obtained through a five hole pitot-probe (D) and traversing mechanism (E) arrangement. The pressures from the take-off tubes are measured by the inclined manometers F and G.

The cyclone chamber, depicted in Fig. (3.1.2) has a cylindrical configuration with a constant cross-sectional area of 15.24 cm radius and a height of 45.72 cm. Swirl is imparted to the fluid, in the counterclockwise direction, by four identical inlet ports 90° apart with a total inlet area of 68.75 cm^2. These are located around the lower periphery of the chamber. The air supply is carefully arranged in such a way as to assure nearly the same volumetric flowrate in each port. Along the circumferential wall, seven openings are drilled from which the probe is easily inserted into the chamber. In each opening, a pressure seal is fitted to avoid air leakage and simultaneously assist in the proper radial alignment of the probe. The modular construction of the top plate incorporates several rings to allow the variation of the exit flow area.

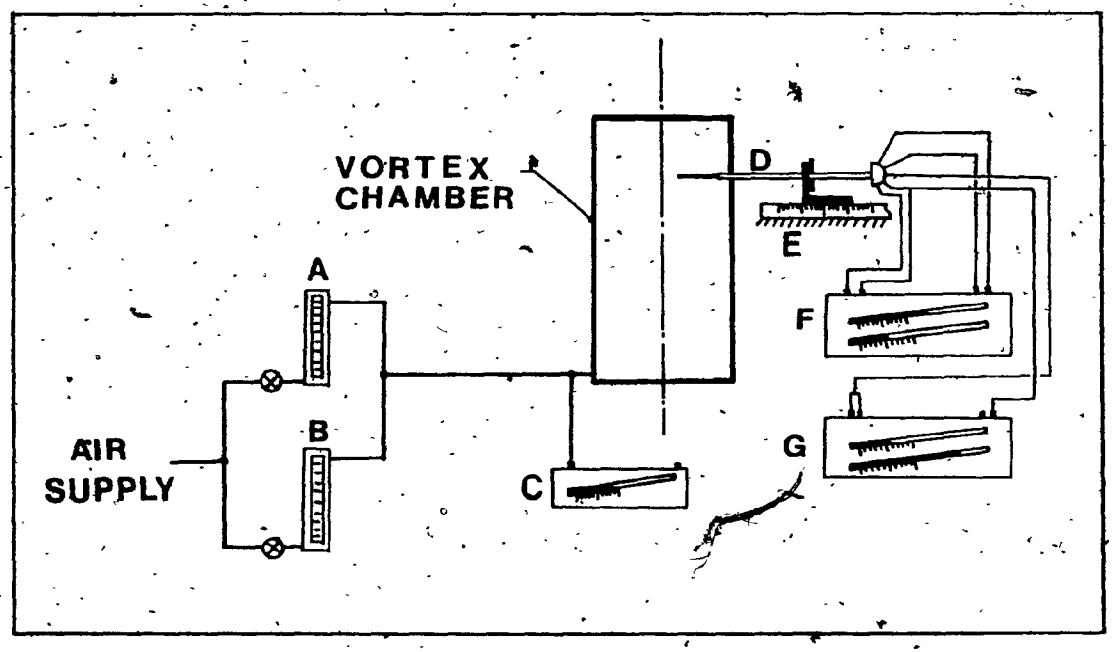

Fig. 3.1.1: A Layout of the Experimental Facility.

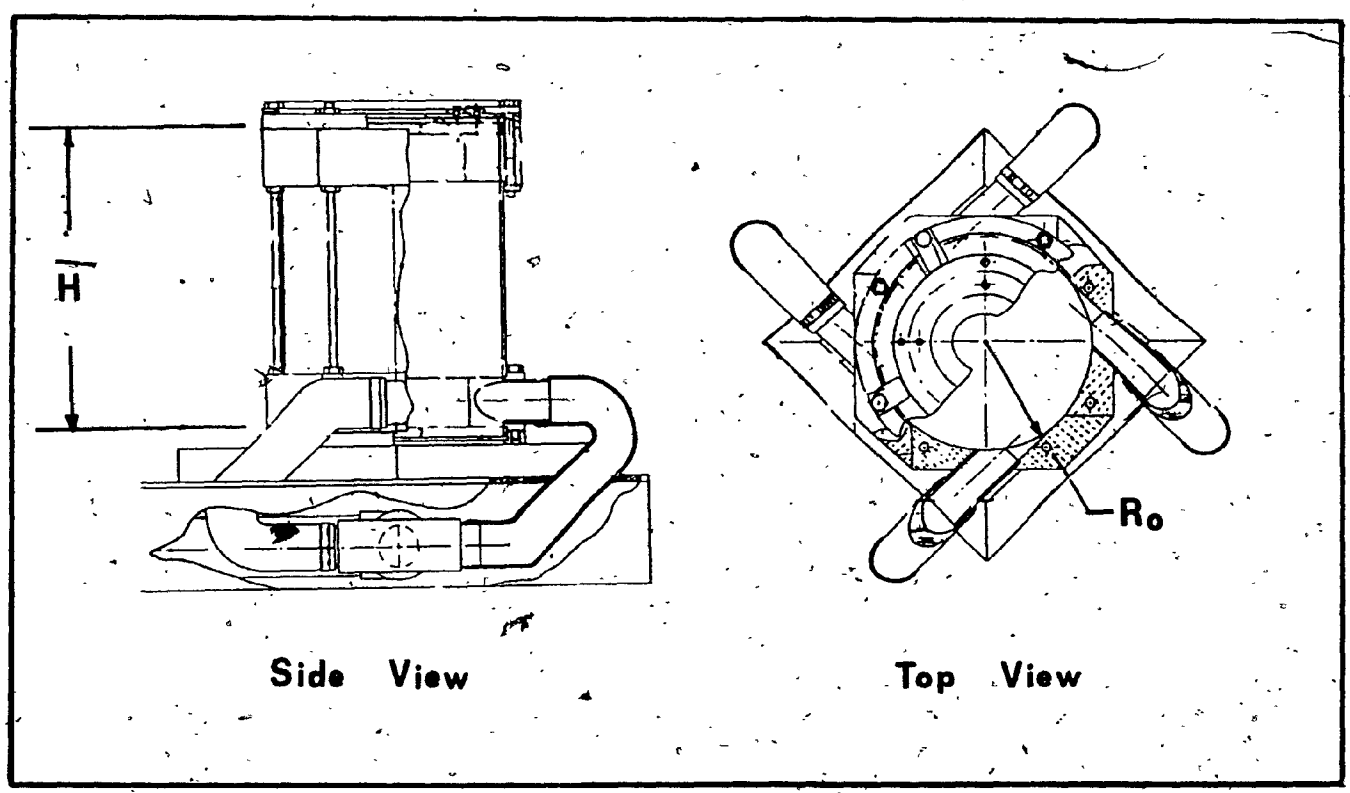

Fig. 3.1.2: The Cyclone Chamber. [6]

3.2 Instrumentation

The three-dimensional character of the flow inside the chamber, realized in preliminary experiments, requires a measuring instrument which can sense the magnitude of the mean velocity as well as its direction. Among the simplest instruments that can perform the task is the five-hole pitot-probe [60]. For the present experiments, the three-dimensional United Sensor and Control Corp. Probe model DA-125-24-F22-CD was used. The probe and its dimensions are shown in Fig. (3.1.3). It has a prismatic sensing head where five fine holes are located. The DA-125-12-CD hook-shaped probe which is also available, was considered at the beginning. However, the second probe was rejected on the assumption that it could not provide measurements near the circumferential wall. Extension of the probe to the opposite side of the wall was thought to considerably affect the vortex structure in the chamber.

The movement of the probe is manually controlled by a three-dimensional traversing mechanism. The movements of the mechanism in the z-and θ-directions, defined in Fig. (2.2.1), were only utilized to position the probe at a specified axial station and then achieve a radial alignment of the probe respectively. The radial traversing was possible with the third available movement of the mechanism, within an accuracy of (±0.127 cm). The yaw angle of the probe is determined via an adjustable disk-dial, shown in Fig. (3.1.4) which is subdivided in 0.5° intervals.

The static pressures from the probe as well as from the inlet pressure taps are measured by several sensitive inclined manometers. This kind of instrument is of the "well-type" and is filled with Meriam oil with specific gravity equal to 0.787. It can assume three different

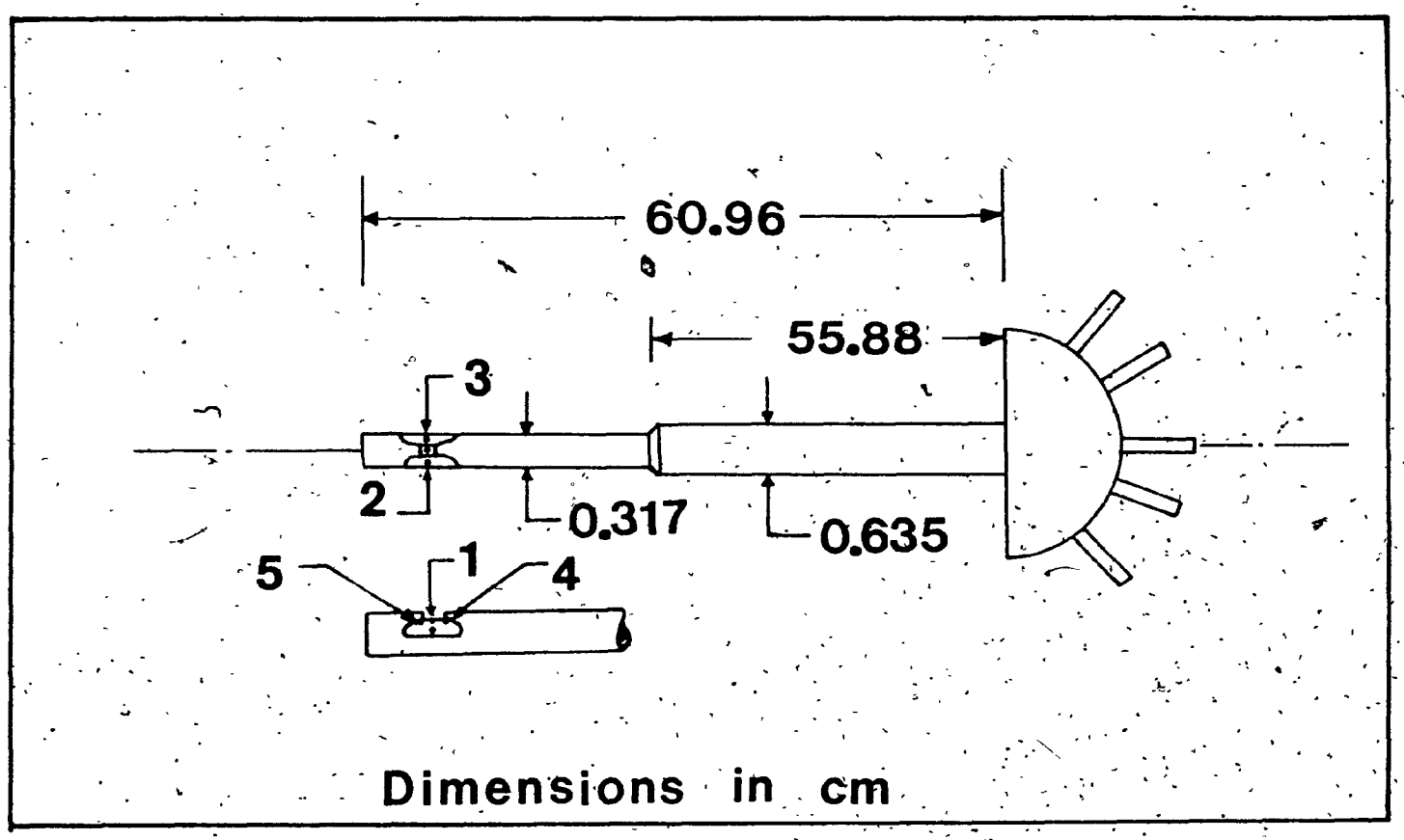

Fig. 3.1.3: The Five-Hole Pitot-Probe.

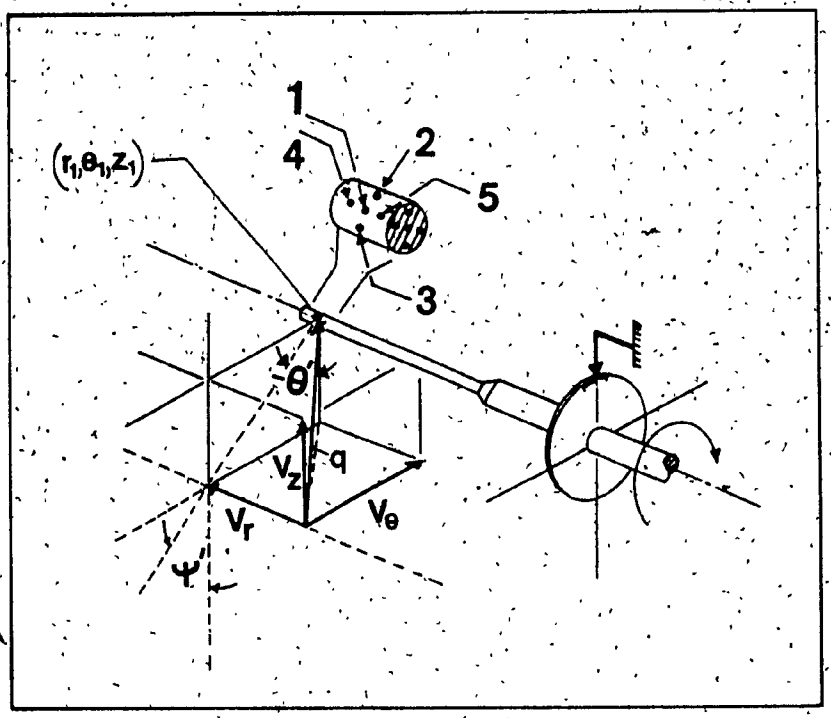

Fig. 3.1.4: Coordinate System, Illustrating the Velocity Components and Flow Direction Associated with the Five-Hole Pitot-Probe.

inclined positions and its scale is subdivided into an equivalent water head. The accuracy of the pressure readings varied from 0.13 mm of H_2O at the first (lowest) position to 0.51 mm of H_2O at the third (highest) position.

The instrumentation utilized for the experiments of pressure drop reduction across the vortex chamber is shown in Fig. (3.1.5). The position of the conical plug is controlled with a screw type traversing arrangement. The axial travel of the plug is read from scale A, which is graduated in 0.0127(0.005") of a cm.

In addition to the previously mentioned instruments, two variable area rotameters are also used to measure the volumetric flowrate. These are carefully calibrated for different operating conditions [61,62].

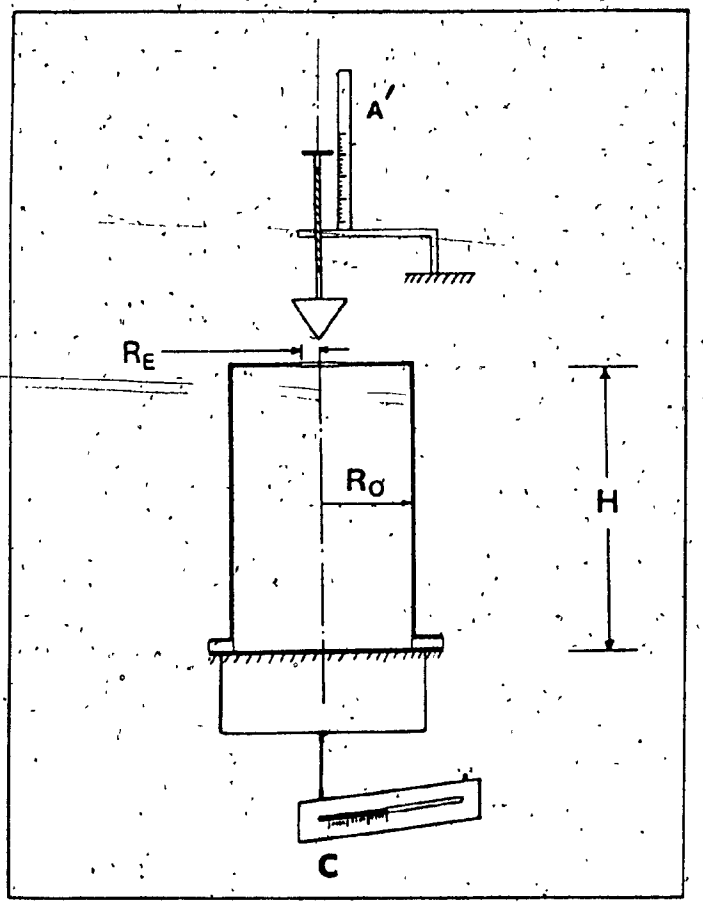

Fig. 3.1.5: Experimental Arrangement for the Reduction of Static Pressure Drop Across the Chamber Experiments.

3.3 Experimental Procedure and Data Reduction

For a typical experimental test, several steps are followed. First, the probe is inserted in the chamber at a specific axial station where the radial transverse is needed. Then the probe is carefully aligned with the radius. The reference angle is established to be zero when the pressure tap no. 1, see Fig. (3.1.4), is aligned with the central axis of the chamber. The desired flowrate is selected and read from the two flowmeters. Approximately fifteen minutes are allowed to elapse prior to any reading, in order for the flowfield to attain a steady-state condition. The pressure drop across the chamber is then recorded. The probe is positioned at the point (r_1, θ_1, z_1) and is rotated about its axis until pressures 2 and 3 are balanced. At this stage pressure tap no. 1 has been aligned with the projection of the total velocity vector $\vec{q}$ in the $V_z - V_\theta$ plane. The pressure differences $(P_1 - P_a)$, $(P_1 - P_2)$ and $(P_4 - P_5)$ and the yaw angle are recorded. The probe is then moved into the next point (keeping θ and z constant) and the process is repeated until a complete radial transverse is made.

The pressure coefficients are calculated from the manometer readings and the total pressure and pitch angle are obtained from the calibration chart which is given in Ref. [61]. From Bernoulli's equation, the magnitude of the total velocity vector at point (r_1, θ_1, z_1), see Fig. (3.1.4), is calculated,

$$|\vec{q}| = \sqrt{2/\rho\ (P_T - P_S)}$$

where, P_T and P_S are the total and static pressures respectively. The velocity components at point (r_1, θ_1, z_1) could then be determined using

the simple trigonometric relations;

$$V_r = |\vec{q}| \sin \psi'$$

$$V_\theta = |\vec{q}| \cos \psi' \sin \theta'$$

$$V_z = |\vec{q}| \cos \psi' \cos \theta'$$

where ψ' and θ' are the pitch and yaw angles respectively, defined in Fig. (3.1.4). To minimize the data reduction time, the computer package of Ref. [61] was used.

3.4 Reliability of the Experimental Results

Several sources of errors may arise when the five-hole pitot-probe is used to map the vortex flowfield. Although most errors cannot be alleviated, their minimization can be effected. Previous experiments revealed that one of the most important factors requiring consideration, is the relative size of the probe. A large probe, in general, tends to decelerate the vortex; and in areas where the fluid motion is almost circular the probe measurements will include the disturbances originated in its own wake [28]. By minimizing the frontal area of the probe and maximizing the circular path in which the fluid wake will convect, one simultaneously reduces both errors. A relatively small probe lessens the deceleration and produces a smaller wake. Furthermore, a larger path allows the viscous dissipation to effectively attenuate the disturbances. These sources of errors were apparent in measurements previously obtained in a smaller cyclone chamber (R_o = 6.98 cm, H = 12.70 cm), using a shorter version of the same probe. For the present experiments, a larger cyclone chamber is used in the attempt to reduce the above mentioned errors.

In the experimental work of Rhode et al [63], which deals with a similar flowfield, the wake effect was investigated. A dummy probe of the same shape and dimensions as the actual one was inserted through the opposite side of the cylindrical wall where the measurements were taken. The measured axial and swirl velocities revealed no significant difference from those obtained in the absence of the dummy probe.

There is little information in the literature to formally give a quantitative account of each source of error in turbulent swirling flowfields. The error, nonetheless, is often presumed to be within 5 percent for most of the measurements, with the provision that this value may be higher in regions of low dynamic pressures [63-65]. These values reflect the total velocity, however, in vortex chambers additional complications are to be considered. The radial and axial velocity components are frequently overshadowed by the dominant tangential velocity. As a result, the instrument favoring this velocity almost ignores the other two components. An indication of this problem is also evident from the signficant difference between the calculated volumetric flowrate, based on the experimental and the actual distributions [61]. The measured pressure difference $(P_4 - P_5)$ on which the radial velocity strongly depends is very small outside the core. This, coupled with the radial static pressure interference, induced from the strong centrifugal field, renders the experimental radial velocity unreliable. The latter problem will be discussed at length in Section 4.5. It is therefore apparent, that the most uncertain regions in the flowfield are those with small dynamic pressures and/or low radial and axial velocity components.

CHAPTER 4

ANALYTICAL AND EXPERIMENTAL STUDIES IN VORTEX CHAMBERS

CHAPTER 4

ANALYTICAL AND EXPERIMENTAL STUDIES OF FLOWFIELDS IN VORTEX CHAMBERS

In the present chapter, analytical and experimental investigations concerning the flow in vortex chambers are presented. Based on the equations of motion and energy, with neglected viscous effects, the point of maximum tangential velocity is determined. Then, the dimensionless pressure distribution in the radial direction, the flow coefficient and the reverse flow radius inside the core are calculated. The study shows that all these parameters depend solely on the geometry of the chamber. Experimental axial velocity profiles, within the chamber, and for different inlet volumetric flowrates are also presented. Interference of the induced radial static pressure, due to centrifugal force balance, in radial velocity calculations, are shown to be more serious, for dimensionless radii (r/R_o) greater than 0.4. Ways to reduce the pressure drop across a chamber of small contraction ratios are shown through experiments. The analytical findings are compared favourably with the present experimental results, as well as with the results given by several others.

4.1 Governing Equations

Consider the steady flow of an incompressible and inviscid fluid inside the vortex chamber of Fig. (4.1.1), with an exaggerated exhaust manifold. The governing equations are:

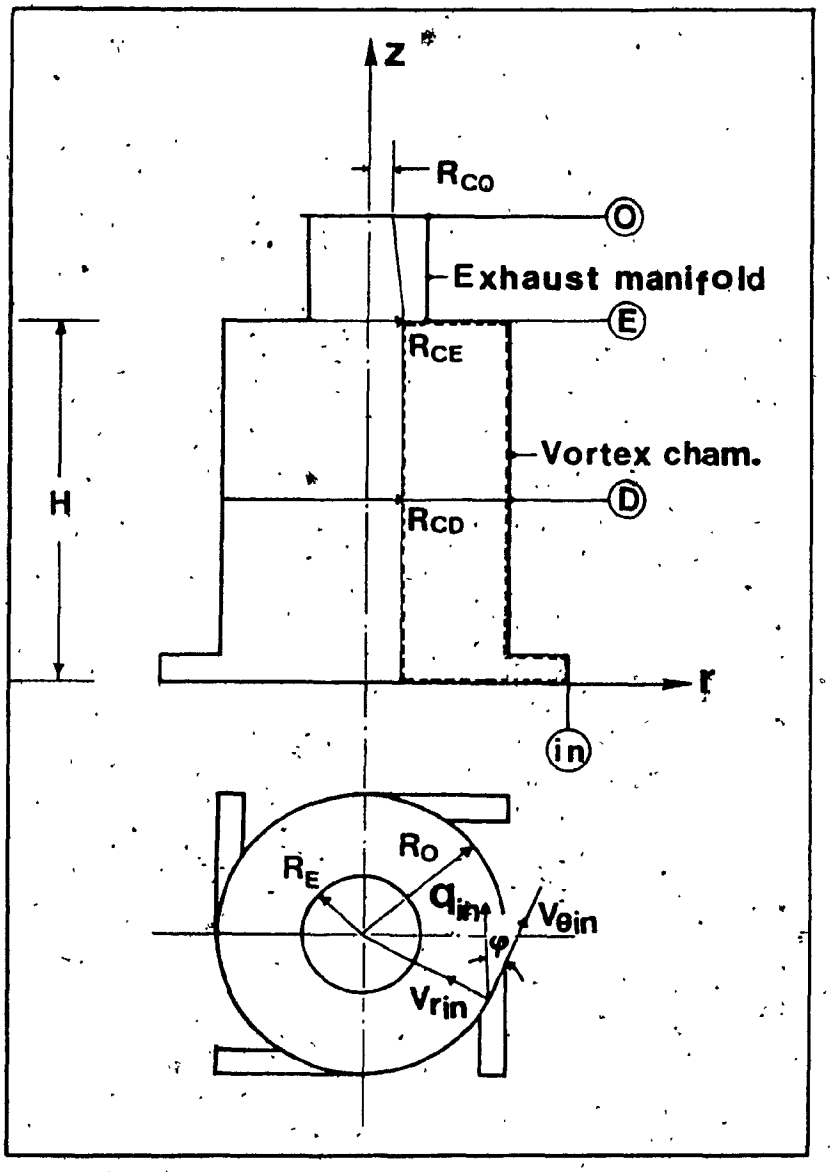

Fig. 4.1.1: Schematic of the Physical System

momentum equation

$$\vec{\nabla}\left(\frac{P}{\rho} + \frac{\vec{q}^2}{2}\right) + \vec{q} \times \text{curl}\, \vec{q} = 0 \qquad \text{(a)}$$

continuity equation (4.1.1)

$$\vec{\nabla} \circ \vec{q} = 0 \qquad \text{(b)}$$

where,

$$\text{curl}\, \vec{q} = \vec{e}_r\, \xi + \vec{e}_\theta\, \eta + \vec{e}_z\, \zeta.$$

and the vorticity components for the axisymmetric flow are:

$$\xi = -\frac{\partial V_\theta}{\partial z} \qquad \text{(a)}$$

$$\eta = \frac{\partial V_r}{\partial z} - \frac{\partial V_z}{\partial r} \qquad \text{(b)} \qquad (4.1.2)$$

$$\zeta = \frac{\partial V_\theta}{\partial r} + \frac{V_\theta}{r} \qquad \text{(c)}$$

For a potential flow, the vorticity components in all directions are zero, and eq. (4.1.2) and eq. (4.1.1) gives the Bernoulli equation.

It is interesting to note that if continuity equation and the equation for the η-vorticity are condensed into a single equation with the aid of the streamfunction, the resulting equation will not in fact contain the velocity component in θ-direction. This suggests that for a potential flow, the fluid motion in r-and z-directions is taking place though V_θ was absent. However, it should be noted that the potential flow assumption outside the core region in the vortex chamber is only an approximation.

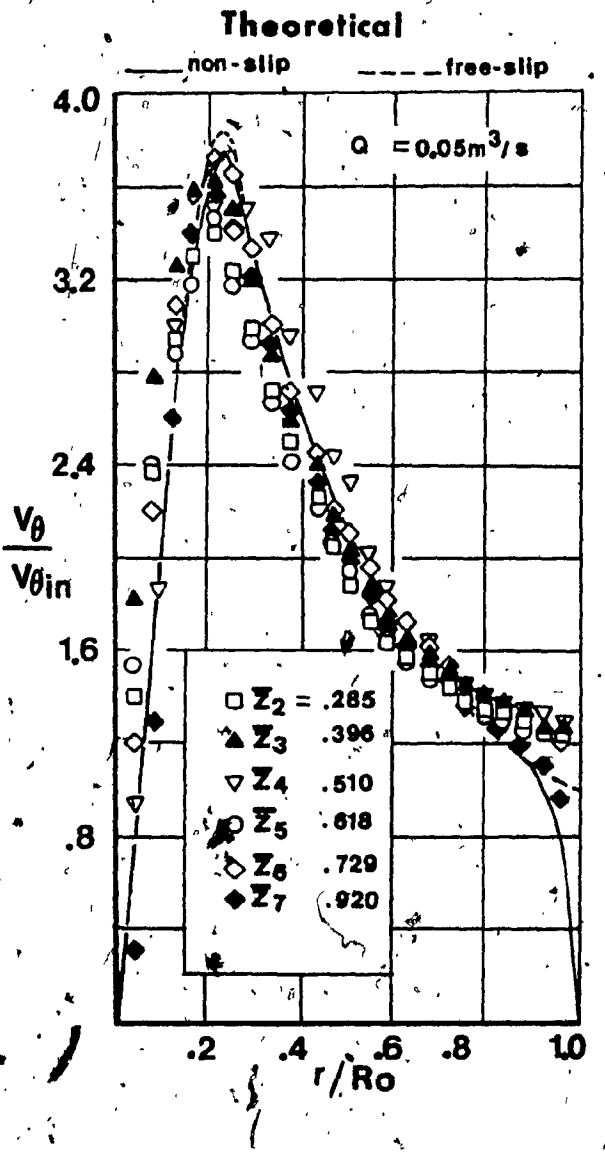

Fig. 4.2.1: Experimental Tangential Velocity Distribution for Different Axial Stations [$\bar{z}$ = distance from the bottom plate/height of the chamber].

4.2 The Core-Size

Experimental results, shown in Fig. (4.2.1), indicated that the radius where the maximum tangential velocity occurs does not vary significantly along the height of the chamber. This is also evident from the experimental studies of Reydon and Gauvin [66] and Ogawa [67]. The core, in the present study, is defined as the space bounded by a cylindrical surface having the same radius with the point of maximum tangential velocity. In view of the above mentioned experimental evidence, the core is assumed constant within the vortex chamber. The potential flow region is restricted outside the core, in the control volume illustrated in Fig. (4.1.1) by dashed lines. In the flow area inside the exhaust manifold above the control volume, the potential theory can not be applied, since the condition of a constant static pressure at the exit of the manifold it cannot be met.

For the potential flowfield, energy conservation is expressed by,

$$\frac{P}{\rho} + \frac{\vec{q}^2}{2} = \text{const} \qquad (4.2.1)$$

The above equation implies that every point in the field has the same total energy. Application of eq. (4.2.1) for the flow from the inlet to the exit (throat E) shown in Fig. (4.1.1), yields,

$$\frac{P_E(r)}{\rho} + \frac{q_E^2(r)}{2} = \frac{P_{in}}{\rho} + \frac{q_{in}^2}{2} \qquad (4.2.2)$$

At the inlet, P_{in} and q_{in} are assumed to be uniform, and on E-plane only the axial velocity is constant while P_E and V_θ are functions of the radius. The streamlines, from within the chamber, converge on plane E,

due to the presence of the exhaust manifold, signifying an increase in velocity. At a plane just above E, the streamlines are almost parallel to the surface of the manifold. The latter implies that the radial velocity is much smaller than the axial. Therefore,

$$V_{rE} \cong 0$$

is a reasonable assumption. Because the radial velocity is zero at E-plane, and V_{zE} is constant, the tangential velocity from eq. (4.1.2c) has to vary with the radius according to,

$$V_\theta = \frac{\Gamma}{2\pi r} \qquad (4.2.3)$$

where Γ is the vortex strength at the inlet. It should be noted that V_θ in eq. (4.2.3) has no subscript. This is because the same equation applies everywhere in the potential field. Therefore, the left hand side of eq. (4.2.2) evaluated at $r = R_{CE}$ and solving for the pressure difference gives,

$$\frac{2\,(P_{in} - P_{CE})}{\rho} = \left(\frac{\Gamma}{2\pi R_{CE}}\right)^2 + V_{zE}^2 - q_{in}^2 \qquad (4.2.4)$$

Incorporating the continuity equation,

$$Q = V_{zE}\,\pi\,(R_E^2 - R_{CE}^2) = q_{in}\,A_{in} \qquad (4.2.5)$$

into (4.2.4) yields,

$$\frac{2\Delta P_E}{\rho} = \left(\frac{Q}{\pi R_E^2}\right)^2 \frac{1}{(1-X_{CE}^2)^2} + \left(\frac{\Gamma}{\pi R_E}\right)^2 \frac{1}{4X_{CE}^2} - \left(\frac{Q}{A_{in}}\right)^2 \qquad (4.2.6)$$

where,

$$\Delta P_E = P_{in} - P_{CE} \quad \text{and,} \quad X_{CE} = \frac{R_{CE}}{R_E}.$$

For given values of Q, A_{in}, R_E and Γ, one obtains from eq. (4.2.6),

$$\lim_{X_{CE} \to 0} \left(\frac{2\Delta P_E}{\rho}\right) = \infty \quad \text{and} \quad \lim_{X_{CE} \to 1} \left(\frac{2\Delta P_E}{\rho}\right) = \infty$$

From the above, it is evident that there must be an X_{CE}, in $0 < X_{CE} < 1$, such as to minimize the pressure difference, or,

$$\frac{\partial}{\partial X_{CE}} \left\{\frac{2\Delta P_E}{\rho}\right\} = 0 \qquad (4.2.7)$$

Under condition (4.2.7), eq. (4.2.6) yields,

$$X_{CE}^6 + (2a - 3)\, X_{CE}^4 + 3X_{CE}^2 - 1 = 0 \qquad (4.2.8)$$

where,

$$a = \left[\frac{A_{in}/A_o}{\frac{R_E}{R_o}\cos\varphi}\right]^2, \quad \text{and} \quad A_o = \pi R_o^2$$

In order to determine the core size at the exit of the manifold (O-plane) some assumptions have to be made.

1) Experimental results obtained by Shakespeare et al [27], have shown that the axial velocity at the exit of the manifold can be assumed constant for $R_{CO} \leq r \leq R_E$. For the present analysis this assumption is also adopted.

2) The centrifugal acceleration of the swirling flow, restricted by the exhaust manifold causes pressure increase with the radius. Just above the manifold, the fluid is suddenly released by the restraining normal stresses and expands freely into the ambient air. This results

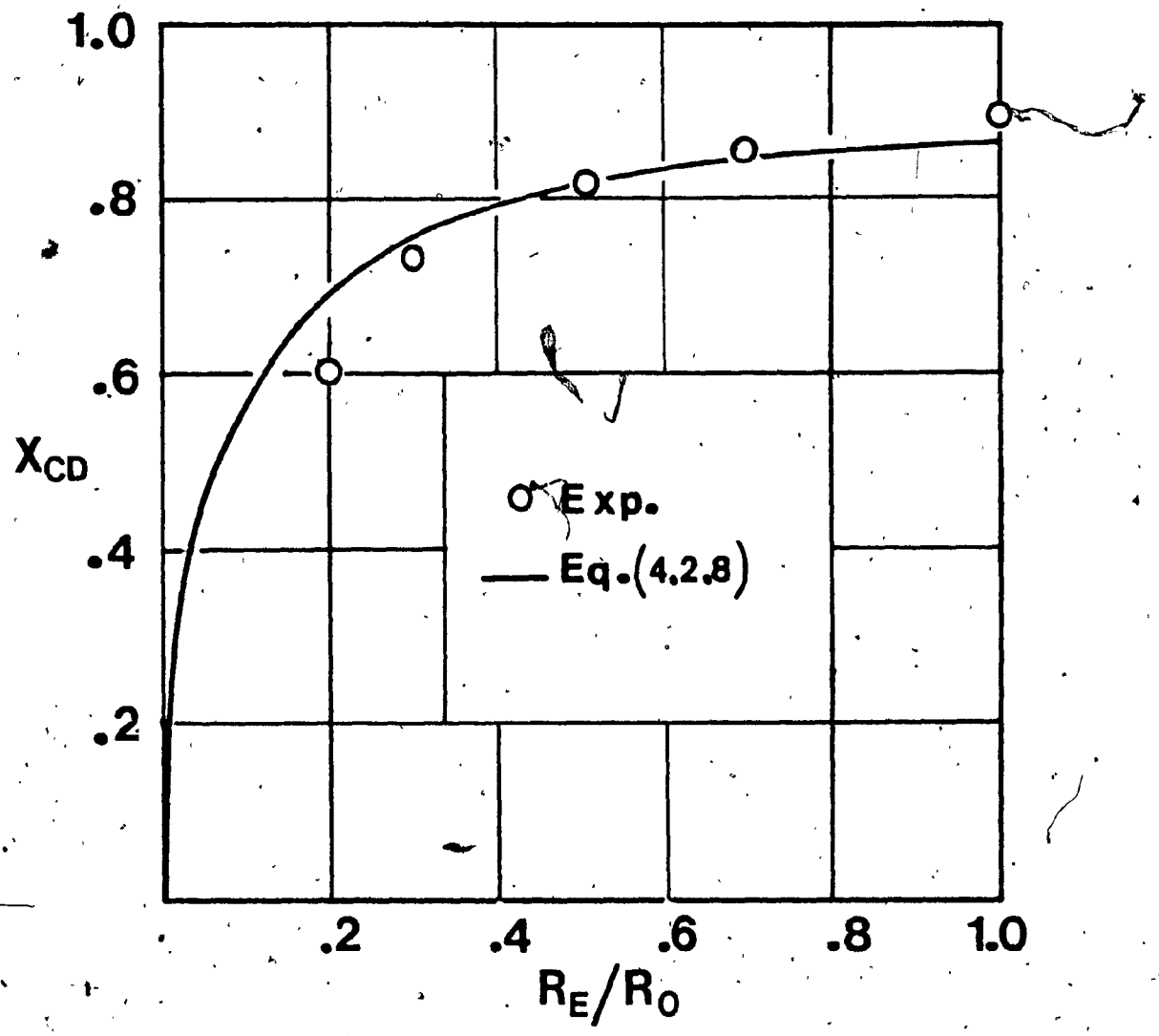

Fig. 4.2.2: Core Size on D-plane for Different $[R_E/R_0]$ (Axial Station z_4).

in a significant radial velocity gradient in the z-direction even though the radial velocity is negligibly small.

3) The tangential velocity is still given by eq. (4.2.3).

The energy equation with neglected potential energy is,

$$\oiint_S \left(p + \frac{\rho q^2}{2}\right) \vec{q} \circ \vec{n}\, ds = -\vec{F} \qquad (4.2.9)$$

Application of eq. (4.2.9) with neglected viscous effects to the flow region bounded by the core, the circumferential wall, the inlet and outlet of the exhaust manifold gives;

$$2\pi \int_{R_{CO}}^{R_E} \left[\frac{P_a}{\rho} + \frac{1}{8}\left(\frac{\Gamma}{\pi r}\right)^2 + \frac{1}{2} V_{zo}^2\right] V_{zo}\, r dr =$$

$$\left(\frac{P_E}{\rho} + \frac{1}{2} q_E^2\right) Q = \left(\frac{P_{in}}{\rho} + \frac{1}{2} q_{in}^2\right) Q \qquad (4.2.10)$$

Integration of eq. (4.2.10) yields,

$$\frac{2\Delta P}{\rho} = \left(\frac{Q}{\pi R_E^2}\right)^2 \frac{1}{(1-X_{CO}^2)^2} + \frac{1}{2}\left(\frac{\Gamma}{\pi R_E}\right)^2 \frac{\ln 1/X_{CO}}{(1-X_{CO}^2)} - \left(\frac{Q}{A_{in}}\right)^2 \qquad (4.2.11)$$

where,

$$\Delta P = P_{in} - P_a \quad \text{and} \quad X_{CO} = \frac{R_{CO}}{R_E}$$

For the same reasons previously discussed, minimization of the pressure difference (eq. 4.2.11) with respect to X_{CO} gives,

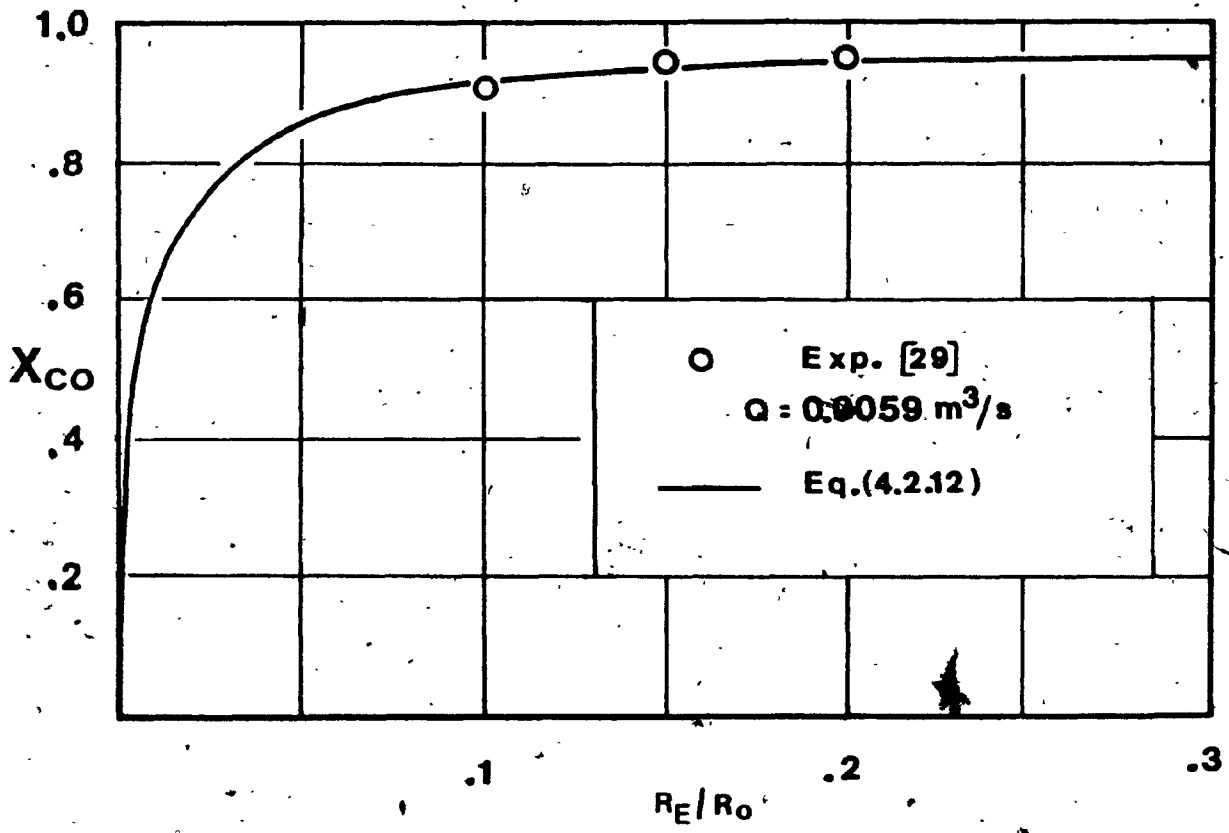

Fig. 4.2.3: Core Size on O-Plane for Different Contraction Ratios.

$$X_{CO}^4 (2\ell n\, X_{CO} - 1) + 2X_{CO}^2 \left[(a+1) - \ell n\, X_{CO}\right] - 1 = 0 \qquad (4.2.12)$$

From eqs. (4.2.8) and (4.2.12), it is evident that the dimensionless radii are functions of the dimensionless geometric parameter a. This in effect implies that the core size does not depend on the absolute dimensions of the chamber. In other words, two geometrically similar vortex chambers have the same X_{CE} and X_{CO}. Because,

$$a = f_n\left(\frac{R_E}{R_o}, \frac{A_{in}}{A_o}, \varphi\right),$$

X_{CE} and X_{CO} must vary with these parameters and are independent on the inlet volumetric flowrate. Since the core size does not depend strongly on the height of the main chamber it is assumed that $X_{CD} \cong X_{CE}$.

Analytical and experimental results of the core radius as a function of the contraction ratio (R_E/R_o) are presented in Fig. (4.2.2). The core size is seen to be strongly dependent on the ratio R_E/R_o, especially for smaller values of R_E/R_o. The smaller the contraction ratio the lesser the dimensionless core radius inside the chamber. A similar behaviour of X_{CO} with (R_E/R_o) is also evident from Fig. (4.2.3). The influence of area ratio (A_{in}/A_o) on X_{CD} is illustrated in Fig. (4.2.4). The two experimental points given in the graph correspond to areas (A_{in}) of 68.75 and 34.37 cm^2. Because of fixed inlet area ports, it was able to obtain only two experimental points with the aid of restrictions inserted at the inlets. The influence of small values of A_{in}/A_o on X_{CD} is of a more moderate nature than the effect of the corresponding values of contraction ratio. Both eqs. (4.2.8) and (4.2.12) suggest that the dimensionless core radii are not functions of the inlet volumetric flowrate. The

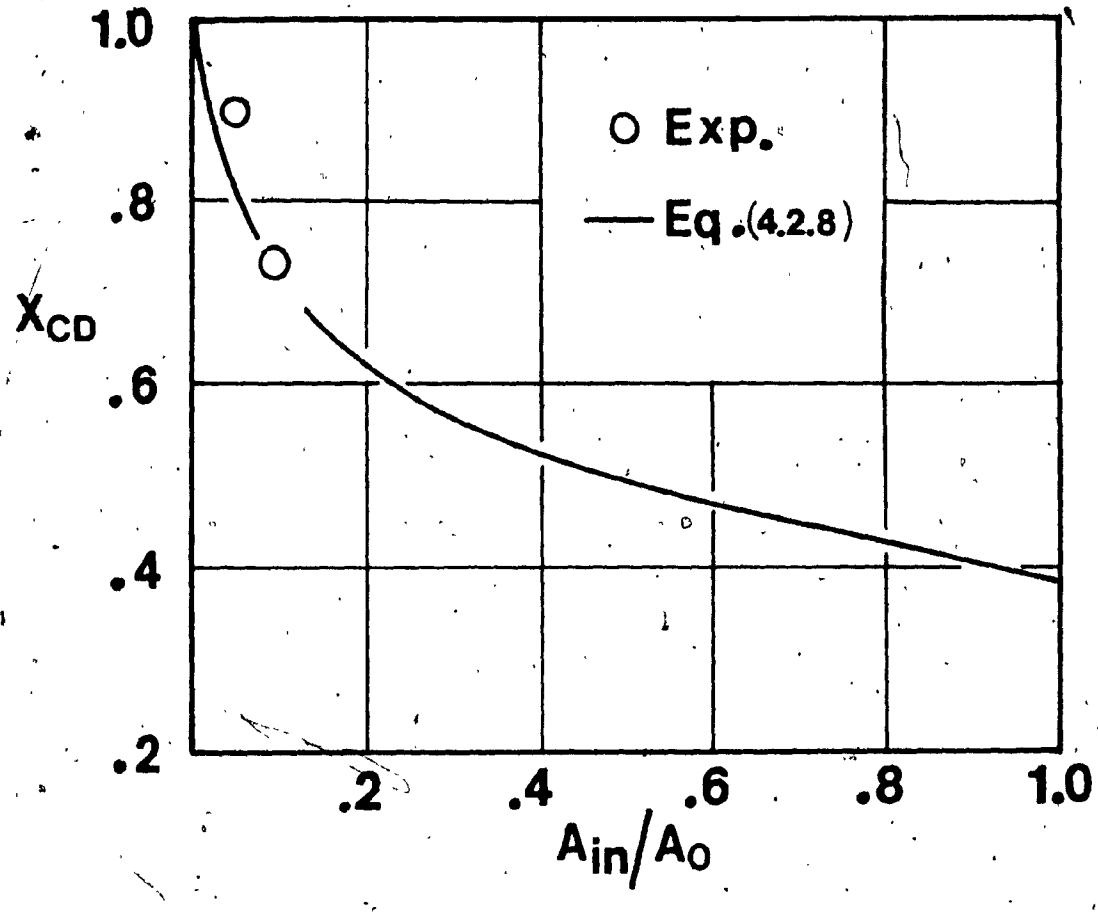

Fig. 4.2.4: Variation of X_{CD} with the Dimensionless Inlet Area ($A_o = 2\pi R_o^2$, $R_E/R_o = 0.3$).

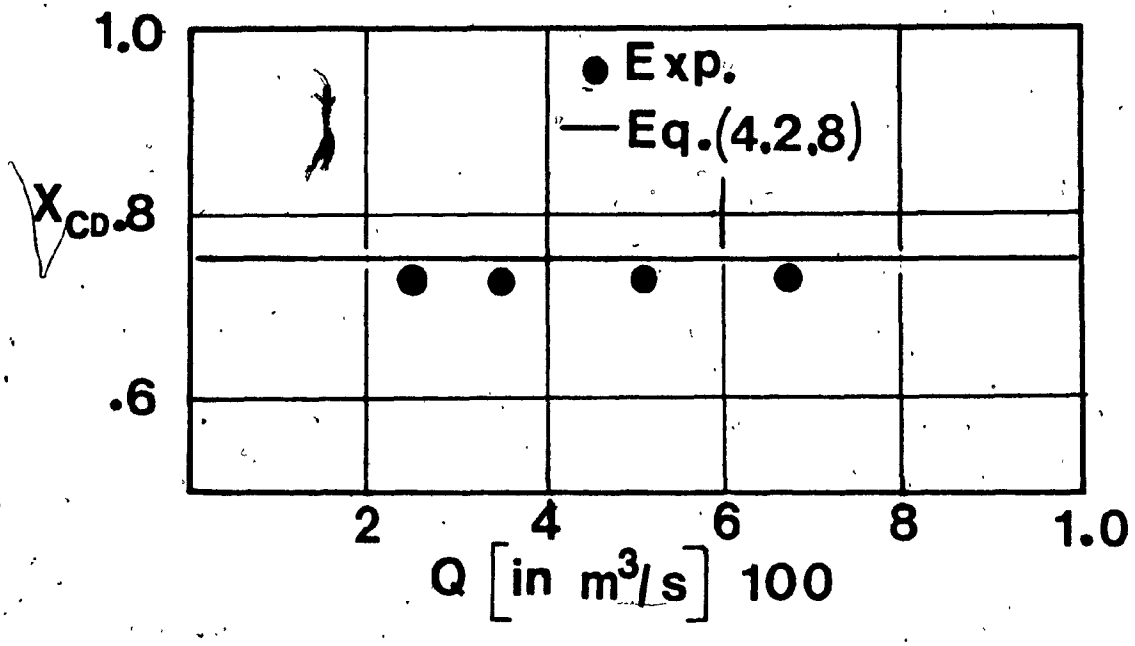

Fig. 4.2.5: Core Size on D-Plane vs. Q (R_E/R_0 = 0.3).

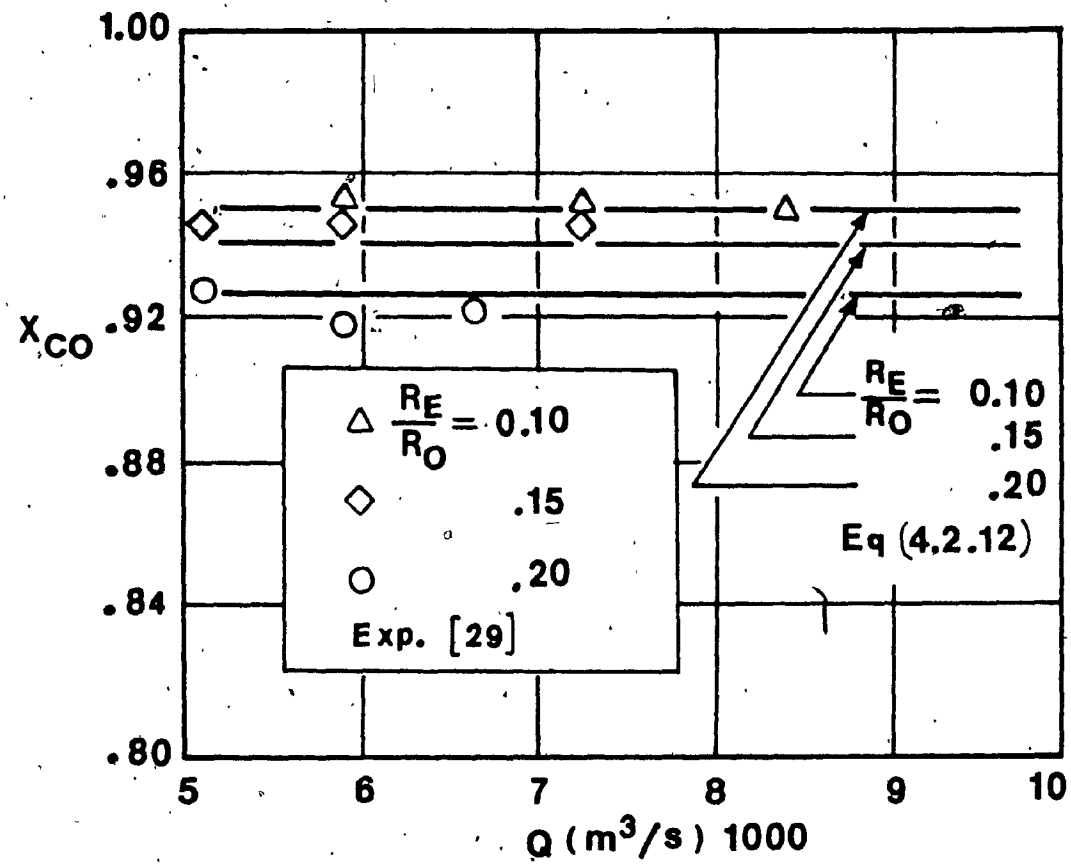

Fig. 4.2.6: Core Size on O-Plane vs. Q.

latter conclusion is confirmed by the experimental data presented in Figs. (4.2.5) and (4.2.6). The experimental results of Reydon and Gauvin [66], presented in Fig. (4.2.7) have also shown that X_{CD} is not a function of Q. Unfortunately, no detailed information concerning the boundary conditions at the inlet is given, thereby no quantitative comparison with the present theory is possible. Nonetheless, the analytical finding is qualitatively established. If X_{CD} is indeed not a function of Q, then the radial distribution of the dimensionless tangential velocity $V_\theta(r/R_o)/V_{\theta in}$, must not be a function of the inlet volumetric flowrate. This conclusion is confirmed by the experimental results presented in Figs. (4.2.8) and (4.2.9).

The effects of inlet swirl number, ($V_{\theta in}/V_{rin}$ or tan (90°-ψ), on the core radius X_{CO} are depicted in Figs. (4.2.10) and (4.2.11). It is seen that the effect of inlet swirl number on X_{CO} is similar to the variation of contraction ratio. An increase of the swirl at the inlet results in an increase of the core. For ψ = 90° (no swirl) there is no core. If $\psi \to o$ which implies an infinite swirl, X_{CO} approaches one asymptotically.

Due to the fact that the tangential velocity does not vary significantly with the height of the chamber, it was found that $V_\theta/V_{\theta in}$ can be approximated by eqs. (2.6.1) or (2.6.2) if the fluid residence time,

$$t_{res} = \frac{\pi R_o^2 H}{Q}$$

is substituted for time (t), $R_{CD} = R_i$ and $V_{\theta in} = V_{\theta o}$. The results of these curve fitting equations are given in Fig. (4.2.1). The curve shown by dashed lines, represents the tangential velocity when wall shear is absent while the other, corresponds to non-slip condition of the velocity

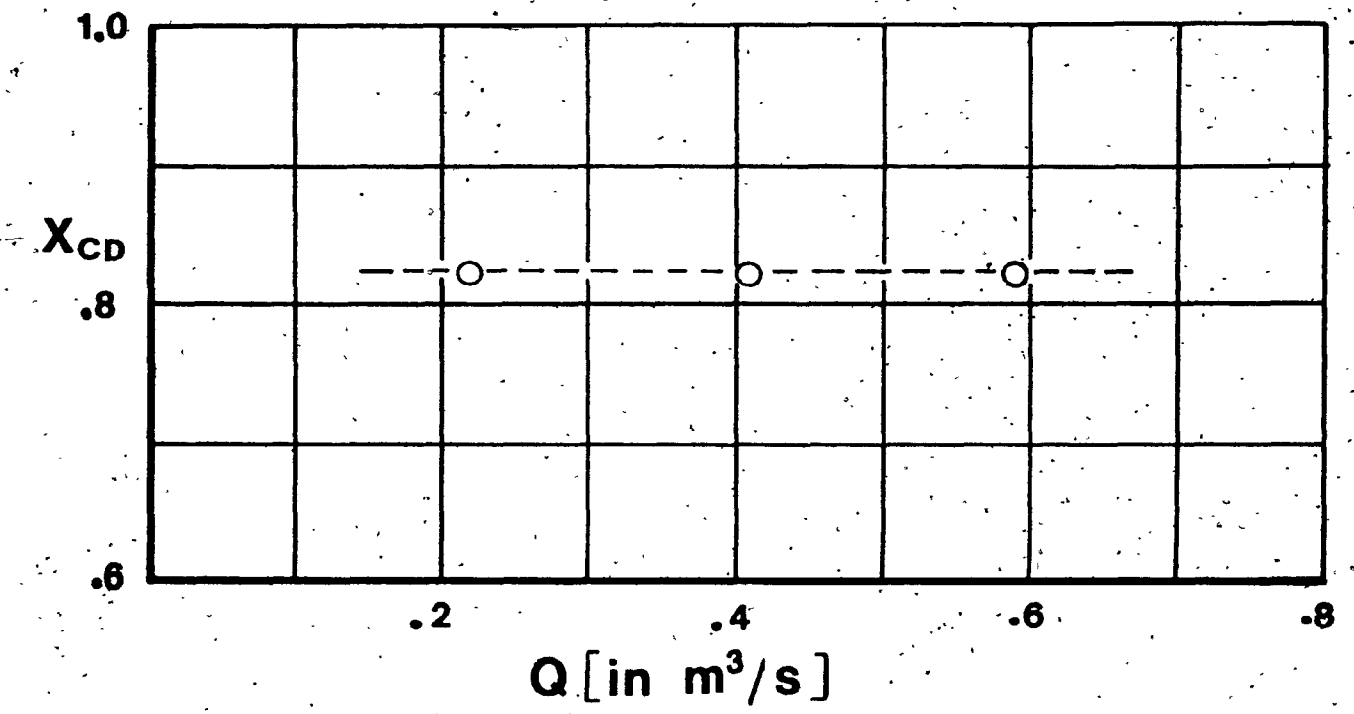

Fig. 4.2.7: Experimental Core Size vs. Q from Ref. [66] - [z_6 = 0.56, R_E/R_O = 0.21].

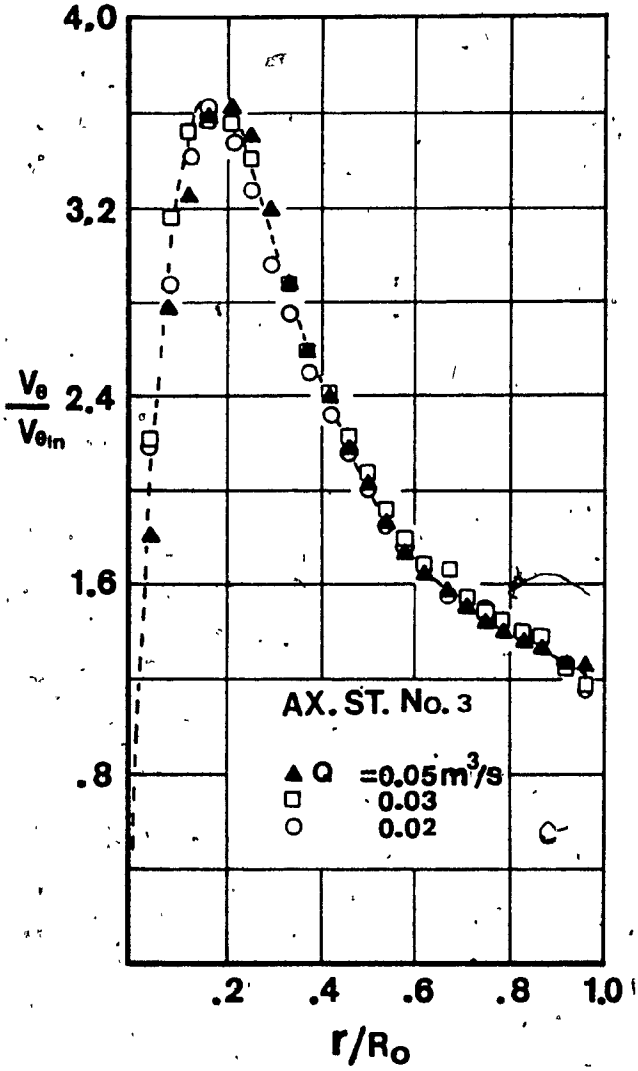

Fig. 4.2.8: Experimental Radial Distribution of the Tangential Velocity for Different Inlet Volumetric Flowrates.

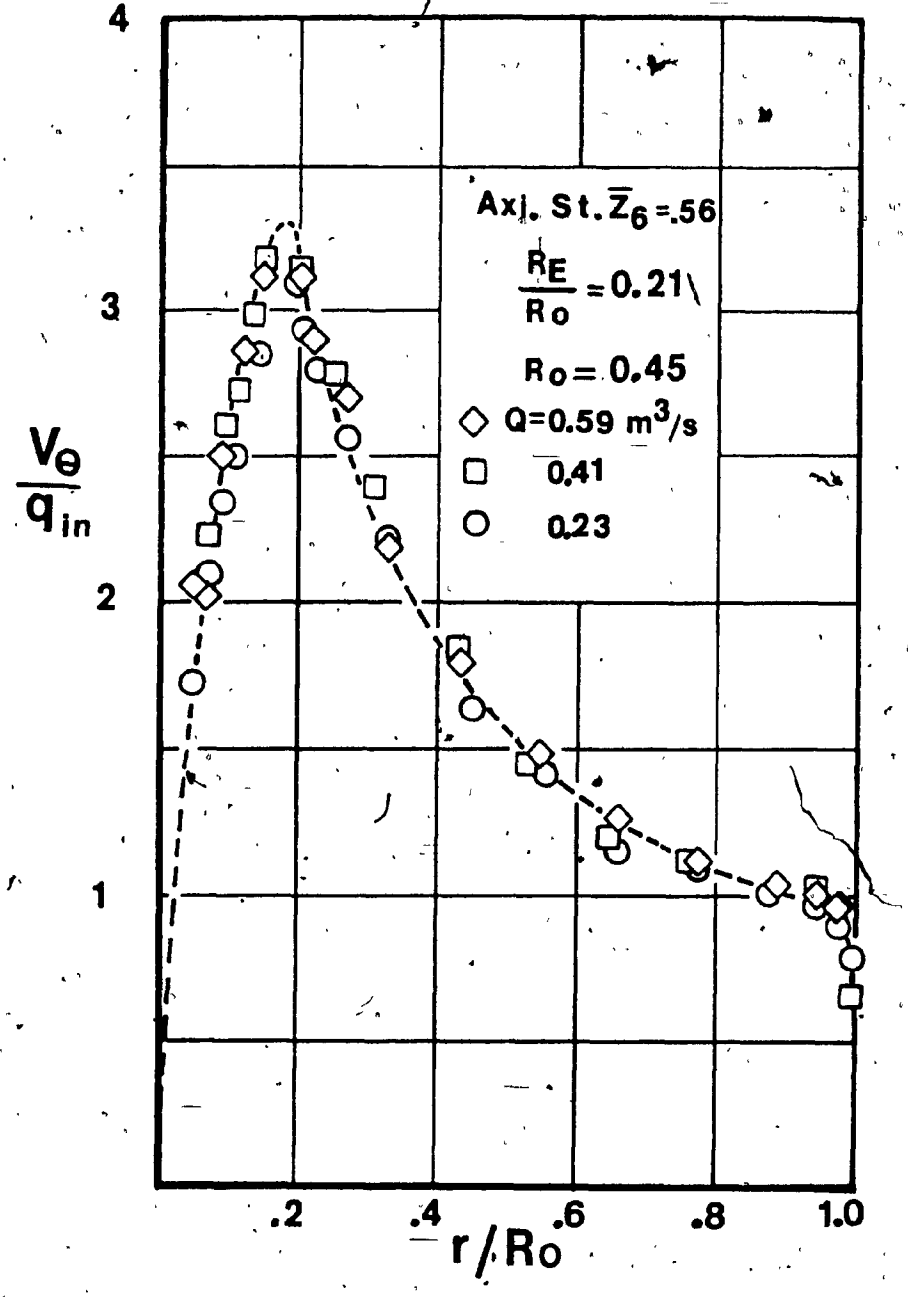

Fig. 4.2.9: Experimental Radial Distribution of the Tangential Velocity for Different Inlet Volumetric Flowrates from Ref. [66].

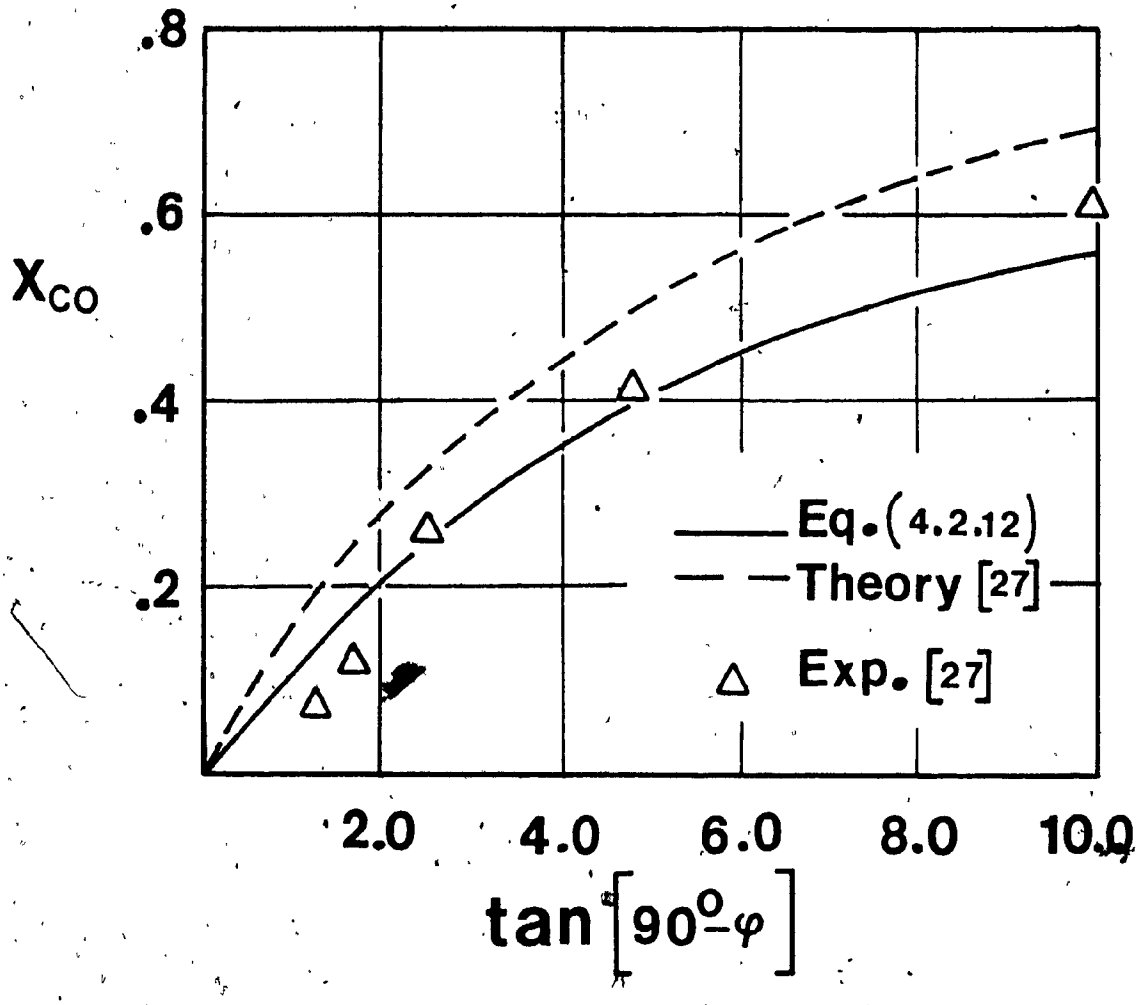

Fig. 4.2.10: Core Size on O-Plane vs. Inlet Swirl [R_E/R_o = 0.333].

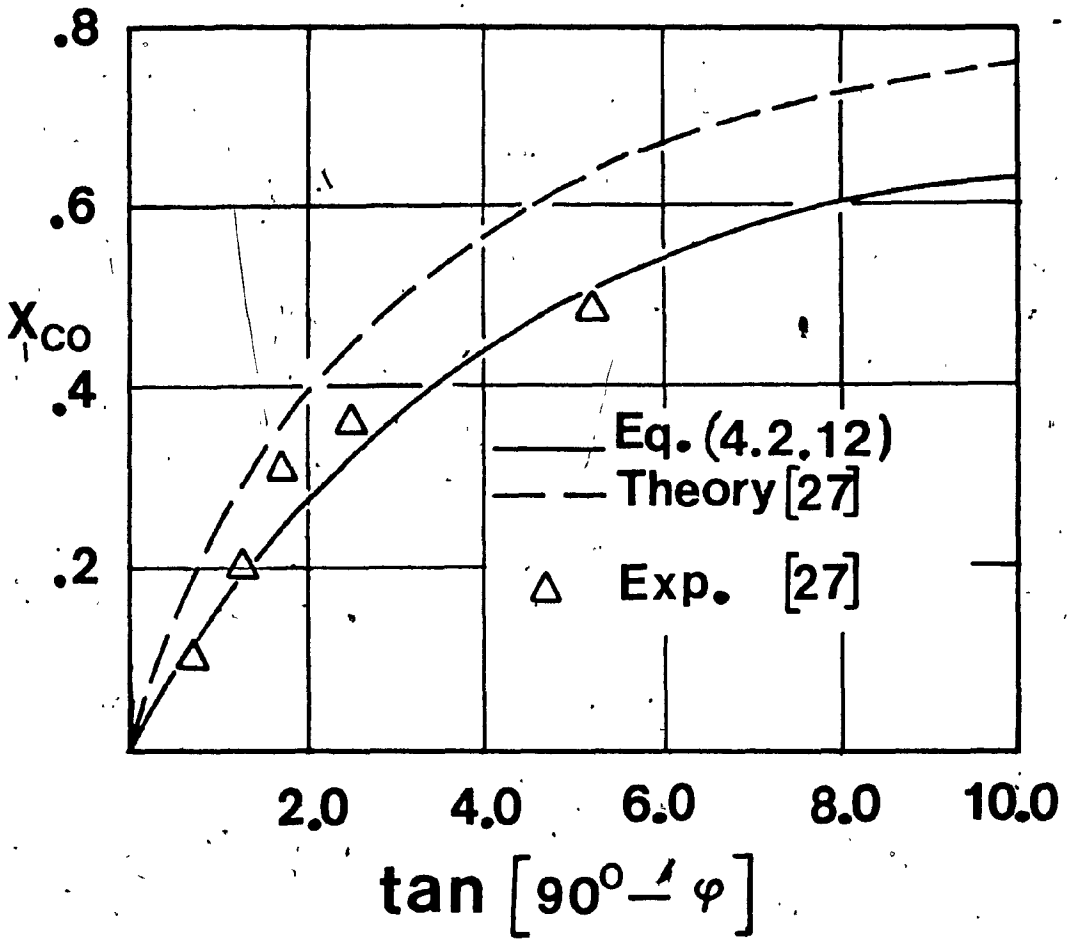

Fig. 4.2.11: Core Size on O-Plane vs. Inlet Swirl [R_E/R_O = 0.5].

on the wall.

4.3 The Static Pressure Drop and Radial Distribution

The static pressure drop across the chamber, from eq. (4.2.11) in terms of the flow coefficient is,

$$\Delta P = \frac{\rho}{2(C_Q A_{in})^2} Q^2 \tag{4.3.1}$$

where,

$$C_Q = \frac{1}{\sqrt{\left\{\left[\frac{\frac{A_{in}}{A_o}}{\left(\frac{R_E}{R_o}\right)^2 (1-X_{CO}^2)}\right]^2 - 1\right\} - \frac{2\cos^2\varphi \ln X_{CO}}{\left(\frac{R_E}{R_o}\right)^2 (1-X_{CO}^2)}}}$$

The flow coefficients obtained by others are summarized in Table 4.3.1. If eq. (4.3.1) is divided by the inlet radial dynamic pressure, yields,

$$\overline{\Delta P} = \left(\frac{1}{C_Q \sin\varphi}\right)^2 \tag{4.3.2}$$

where $\overline{\Delta P} = \frac{2\Delta P}{\rho V_{rin}^2}$

Application of eq. (4.2.1) on plane D, between the wall ($r = R_o$) and any radius, neglecting the radial velocity gives,

$$P_D(r) = P_D + \frac{\rho}{8\pi^2}\left[\left(\frac{\Gamma}{R_o}\right)^2 - \left(\frac{\Gamma}{r}\right)^2\right] \tag{4.3.3}$$

However,

$$P_D(r=R_o) = P_D = P_{in} + \frac{\rho}{2}\left[q_{in}^2 - V_{ZD}^2 - \left(\frac{\Gamma}{2\pi r}\right)^2\right] \tag{4.3.4}$$

where, $V_{zD} = \dfrac{Q}{\pi(R_o^2 - R_{CD}^2)}$

Table 4.3.1: Flow Coefficients

Ref.	C_Q
Levy and Shakespeare (Theoretical)	$C_Q = \dfrac{1}{\sqrt{\dfrac{1}{(R_E/R_o)^2 \tan^2\psi \; X_{CO}^2} - 1}}$
Tager [68] (Empirical)	$C_Q = \dfrac{1}{\sqrt{C_1^* \left(\dfrac{0.9}{R_E/R_o} - 1\right)}}$

*C_1 is obtained experimentally.

Incorporation of eqs. (4.3.2), (4.3.4) and continuity, into (4.3.3), followed by a number of tedious algebraic manipulations gives

$$\overline{\Delta P_D} = \frac{\left(\frac{A_{in}}{A_o}\right)^2}{\left(\frac{R_E}{R_o}\right)^4 (1 - X_{CO}^2)^2} \left\{1 - \left[\frac{1 - X_{CO}^2}{\left(\frac{R_o}{R_E}\right)^2 - X_{CE}^2}\right]^2\right\} \sec^2\psi$$

$$- \left[\frac{2 \ln X_{CO}}{\left(\frac{R_E}{R_o}\right)^2 (1 - X_{CO}^2)} + \frac{1}{\left(\frac{r}{R_o}\right)^2}\right] \cot^2\psi \qquad (4.3.5)$$

The above equation holds for $R_{CD} \leq r \leq R_o$.

If the flowfield inside the core is also dominated by the tangential velocity, then the static pressure in the core, can be approximately

obtained from the momentum equation,

$$\frac{\partial P}{\partial r} = \frac{\rho V_\theta^2}{r}$$

and the known value of the static pressure, from eq. (4.3.5), for $r = R_{CD}$. The radial distribution of the static pressure inside the core $0 \leq r \leq R_{CD}$ is then,

$$\overline{\Delta P_D} = \frac{\left(\frac{r}{R_o}\right)^2 \cot^2\phi}{\left(\frac{R_E}{R_o}\right)^4 X_{CE}^4} + \frac{\left(\frac{A_{in}}{A_o}\right)^2}{\left(\frac{R_E}{R_o}\right)^4 (1-X_{CO}^2)^2} \left\{1 - \left[\frac{1 - X_{CO}^2}{\left(\frac{R_o}{R_E}\right)^2 - X_{CE}^2}\right]^2\right\} \sec^2\phi$$

$$- \frac{2}{\left(\frac{R_E}{R_o}\right)^2} \left[\frac{\ell_n X_{CO}}{(1 - X_{CO}^2)} + \frac{1}{X_{CE}^2}\right] \cot^2\phi \qquad (4.3.6)$$

Making the same line of arguments the dimensionless pressure distribution on E-plane is,

$$\overline{\Delta P_E} = \frac{\left(\frac{A_{in}}{A_o}\right)^2}{\left(\frac{R_E}{R_o}\right)^4 (1 - X_{CO}^2)^2} \left\{1 - \left[\frac{1 - X_{CO}^2}{1 - X_{CE}^2}\right]^2\right\} \sec^2\phi$$

$$- \left[\frac{2\,\ell_n X_{CO}}{\left(\frac{R_E}{R_o}\right)^2 (1 - X_{CO}^2)} + \frac{1}{\left(\frac{r}{R_o}\right)^2}\right] \cot^2\phi \qquad (4.3.7)$$

for $R_{CE} \leq r \leq R_E$, and,

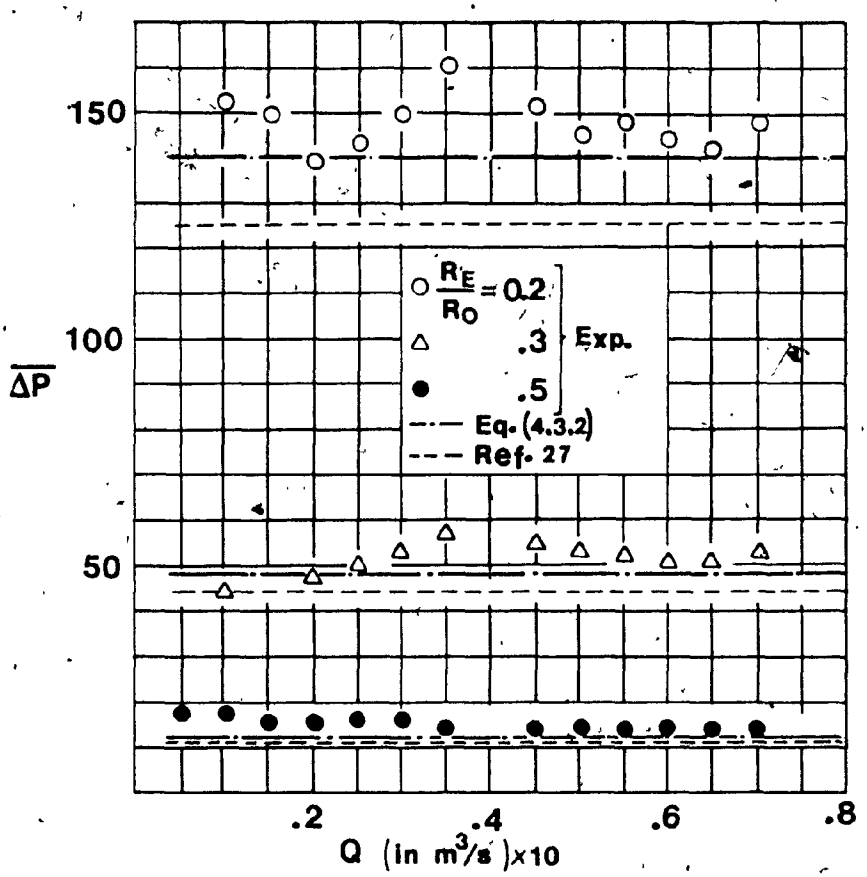

Fig. 4.3.1: Variation of the Dimensionless Pressure Drop Across the Chamber with the Inlet Volumetric Flowrate for Three Contraction Ratios.

$$\overline{\Delta P_E} = \frac{\left(\frac{r}{R_o}\right)^2 \cot^2\psi}{\left(\frac{R_E}{R_o}\right)^4 X_{CE}^4} + \frac{\left(\frac{A_{in}}{A_o}\right)^2}{\left(\frac{R_E}{R_o}\right)^4 (1 - X_{CO}^2)^2} \left\{ 1 - \left[\frac{1 - X_{CO}^2}{1 - X_{CE}^2}\right]^2 \right\} \sec^2\psi$$

$$- \frac{2}{\left(\frac{R_E}{R_o}\right)^2} \left[\frac{\ell n\, X_{C\theta}}{(1 - X_{CO}^2)} + \frac{1}{X_{CE}^2}\right] \cot^2\psi \qquad (4.3.8)$$

for $0 \leq r \leq R_{CE}$.

From eqs. (4.3.2), (4.3.5 - 4.3.8), it is clear that the dimensionless static pressure drop and radial distributions are only functions of the geometric parameters, R_E/R_o, A_{in}/A_o and ψ. It is therefore obvious that none of the parameters $\overline{\Delta P}$, $\overline{\Delta P_D}$ and $\overline{\Delta P_E}$ depend on Q. In Fig. (4.3.1), the experiment shows a small fluctuation of $\overline{\Delta P}$ about a mean value with Q. Nevertheless the agreement with the theoretical result is reasonably good. The independence of $\overline{\Delta P_E}$ and $\overline{\Delta P_D}$ on the inlet volumetric flowrate is depicted in Fig. (4.3.2). With the exemption of $Q = 0.02\ m^3/s$, where an approximate 11% maximum difference is shown, the rest confirms the finding. The experimental results of Ref. [66], depicted in Fig. (4.3.3), also reveal the same behaviour of the dimensionless pressure with the volumetric flowrate. Since the inlet radial velocity is not known, the total inlet velocity is used to dimensionalize the pressure. The pressure is seen, from both figures, to have a maximum value on the wall, and decreases towards the core radius. A further decrement of the pressure inside the core to sub-ambient values, due to solid body rotation (shown by dashed

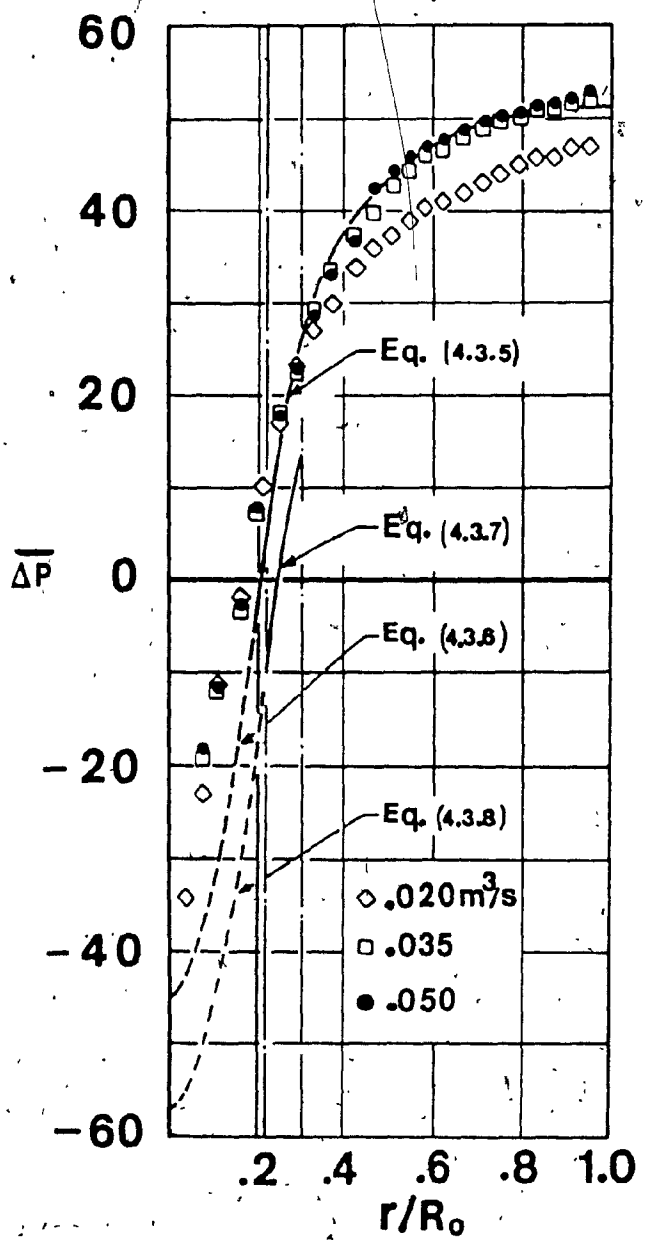

Fig. 4.3.2: Static Pressure Distribution Inside the Vortex Chamber (R_E/R_o = 0.3).

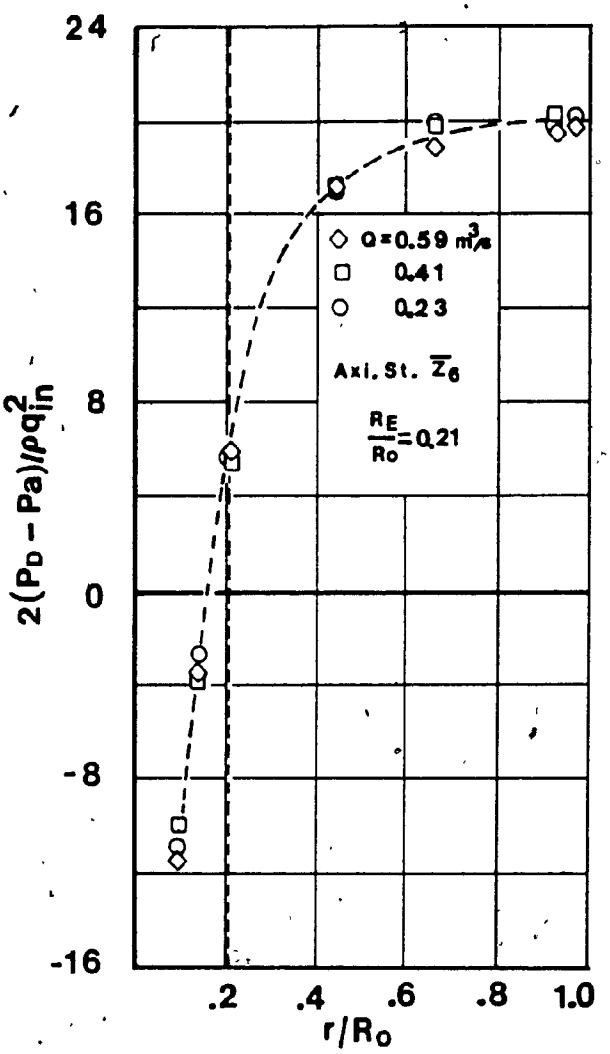

Fig. 4.3.3: Experimental Static Pressure Distribution Inside the Vortex Chamber from Ref. [66].

lines in Fig. (4.3.2), might cause the reverse flow near the axis of rotation. The agreement of the theoretical pressure distribution with the experiment, for the assumed potential flow region, is excellent which is an indication of the tangential velocity domination.
Because the tangential velocity does not depend strongly in the z-direction, $\overline{\Delta P_D}$, from Fig. (4.3.4), is shown not to be a function of z either. The effects of contraction ratio on $\overline{\Delta P}$ is illustrated in Fig. (4.3.5). The hyperbolic profile of $\overline{\Delta P}$ with R_E/R_o indicates that, as R_E/R_o decreases so does the outlet effective area, hence a drastic pressure drop across the chamber. The familiar parabolic behaviour of the pressure drop ΔP vs. Q, similar to the orifice equation, is shown in Fig. (4.3.6).

The influence of the inlet swirl on $\overline{\Delta P}$ is shown in Figs. (4.3.7) and (4.3.8). With the exception of small swirls for the rest, a fair agreement of the theory with the experiment is obtained. For low swirls, the dominating character of V_θ is not true any more and this is manifested by a poor agreement between the experimental and theoretical results. This is more profound in Fig. (4.3.5) where a larger exit is applied. For this case, the generated vortex is weaker and the dissipation is not dominated by the centrifugal effects.

4.4 The Aerodynamic Resistance of Vortex Chamber

In the design of every engineering system the aim is always the same; to achieve the goal with minimum energy cost. The total pressure drop in a vortex chamber, operating at sufficiently large swirls, can be high, unless precautions are taken to minimize it. To effectively achieve the latter goal, the parameters and their behaviour which influences the total pressure drop, must be clearly understood.

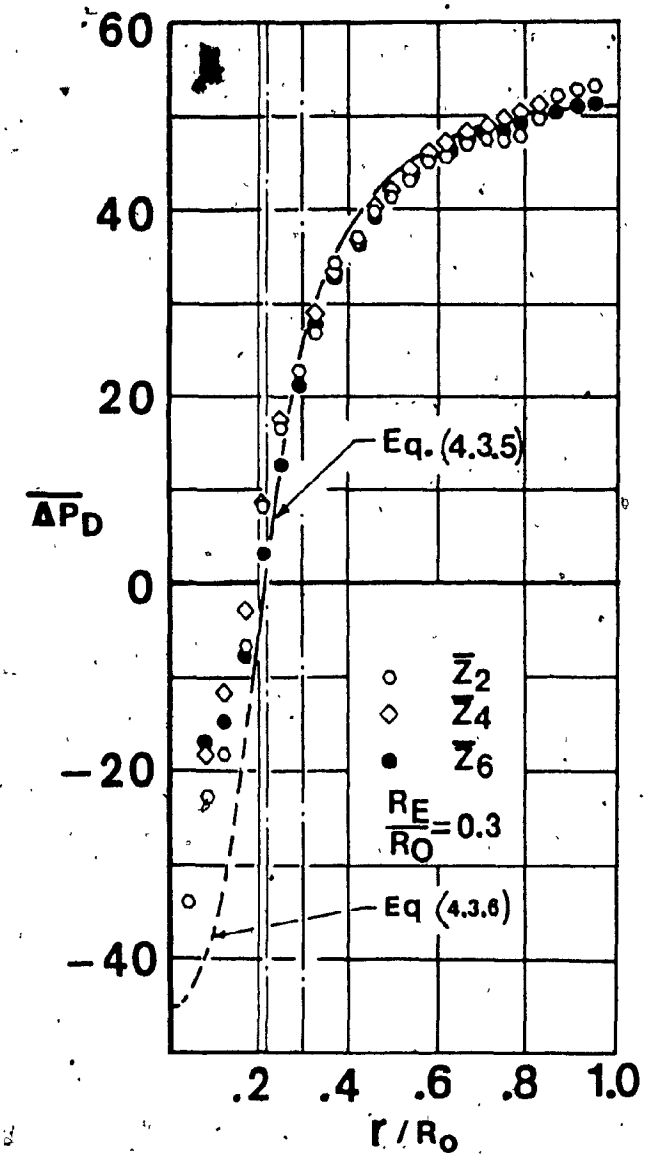

Fig. 4.3.4: Static Pressure Distribution for Different Axial Stations.

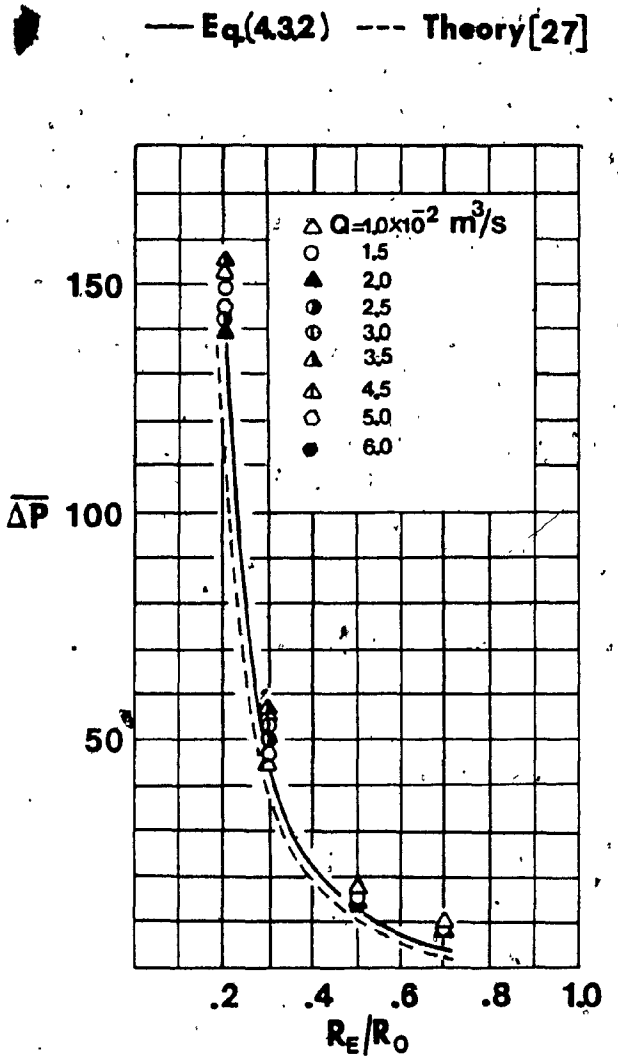

Fig. 4.3.5: Dimensionless Pressure Drop Across the Chamber vs. Contraction Ratio.

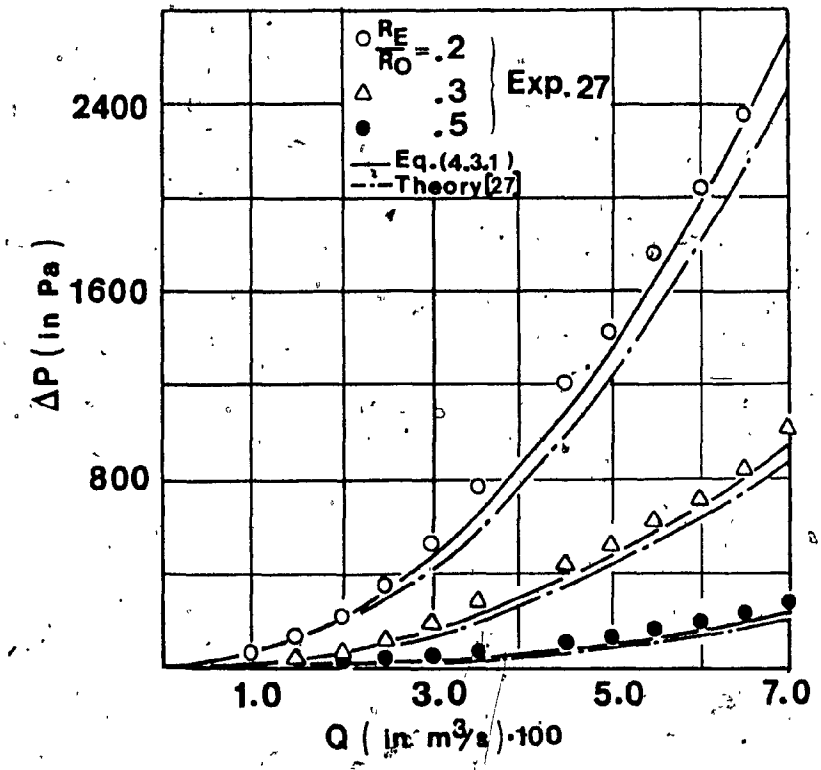

Fig. 4.3.6: ΔP vs. Q for Three Different Contraction Ratios.

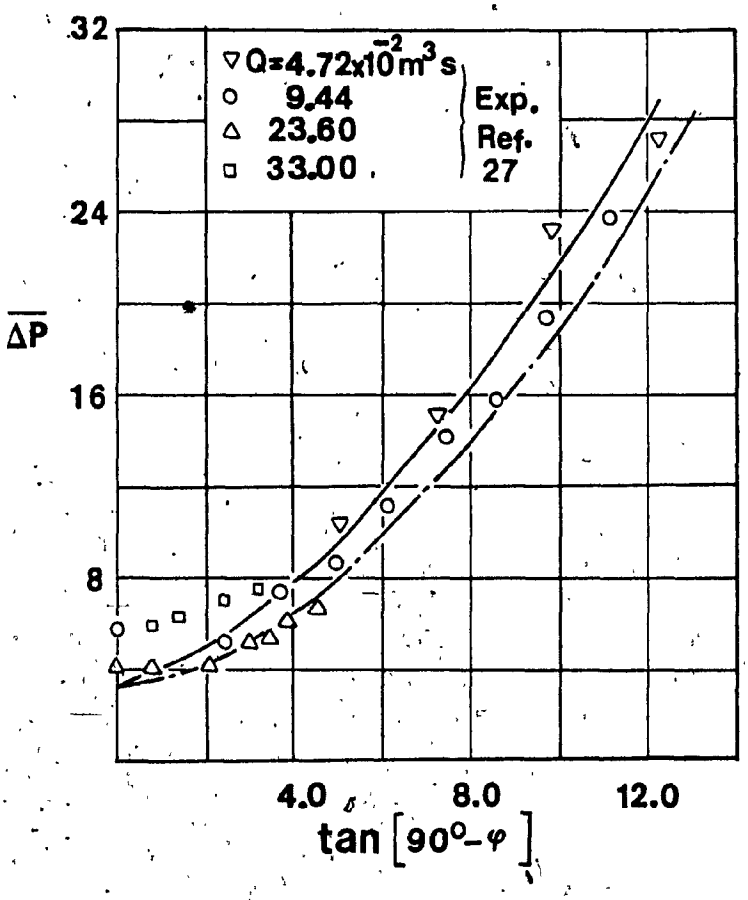

Fig. 4.3.7: Dimensionless Pressure Drop Across the Vortex Chamber vs. Inlet Swirl (R_E/R_o = 0.333), — Eq. (4.3.2), -·- Theory from Ref. [27].

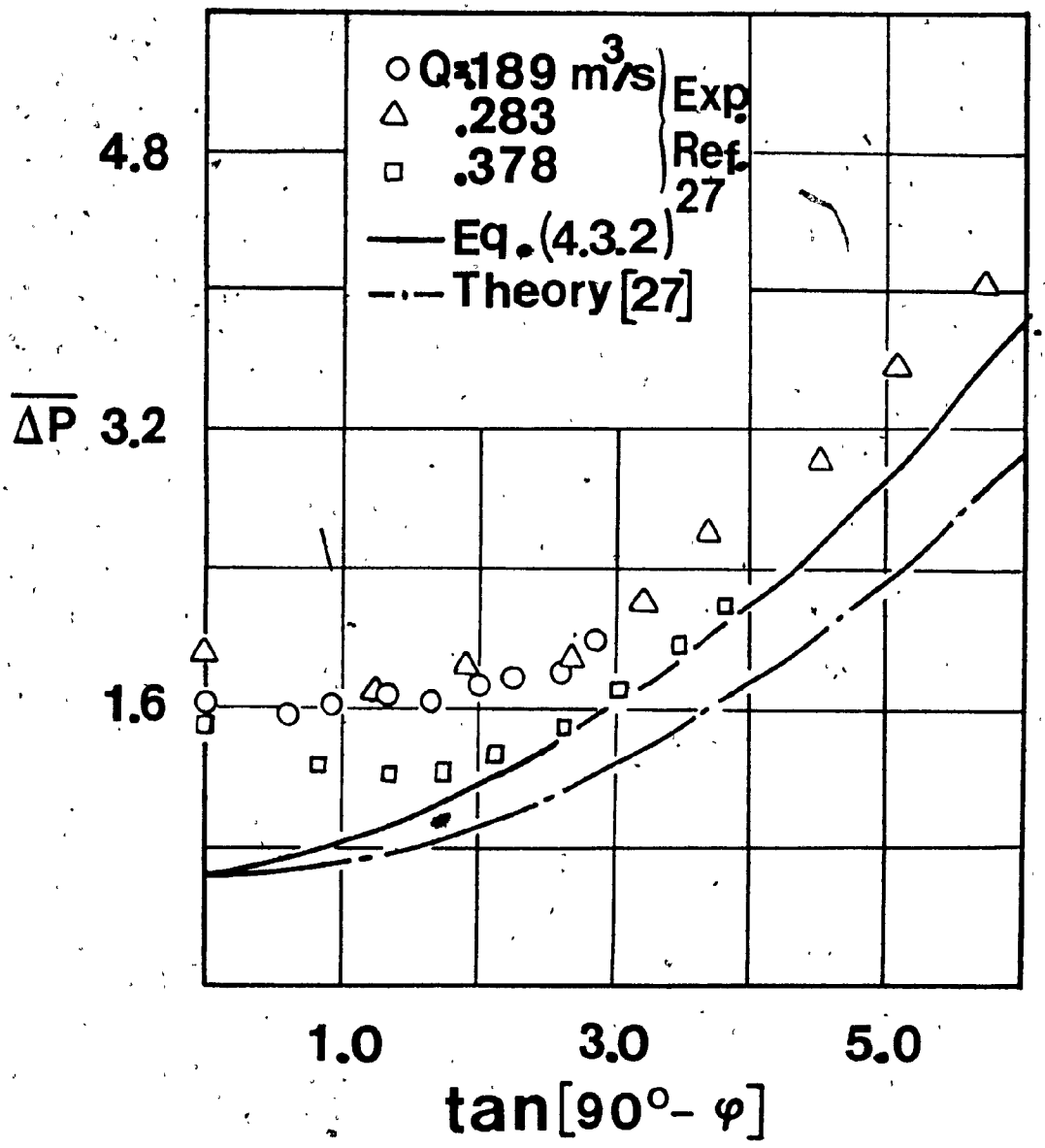

Fig. 4.3.8: Dimensionless Pressure Drop Across the Vortex Chamber vs. Inlet Swirl (R_E/R_0 = 0.5).

The absolute aerodynamic resistance of the chamber was expressed by Troyankin et al [69] by,

$$\Delta\tilde{P} = P_{stag_{(in)}} - P_a = Eu \frac{\rho}{2} V_{zch}^2 \qquad (4.4.1)$$

where, Eu is the Euler number and V_{zch} is the average axial velocity inside the chamber. Equation (4.4.1) gives the energy required to produce the desirable vortex flowfield inside the chamber, therefore it is a very useful parameter to study. From eq. (4.3.1) we obtain,

$$\Delta\tilde{P} = \frac{\rho}{2}\left(\frac{A_o}{A_{in}}\right)^2 \left[\frac{1}{C_Q^2} + 1\right] V_{zch}^2 \qquad (4.4.2)$$

Therefore, from the present analysis,

$$Eu\left(\frac{R_E}{R_o}, \frac{A_{in}}{A_o}, X_{CO}(a), \psi\right) = \frac{\left[\dfrac{\frac{A_{in}}{A_o}}{\frac{R_E}{R_o}^2 (1 - X_{CO}^2)}\right]^2 - \dfrac{2\cos^2\psi \ln X_{CO}}{\frac{R_E}{R_o}^2 (1 - X_{CO}^2)}}{\left(\frac{A_{in}}{A_o}\right)^2} \qquad (4.4.3)$$

The experimental study of Troyankin et al [69] revealed the following facts which are relevant to our study:

1) The dimensionless aerodynamic resistance does not depend on the absolute dimensions of the chamber and is identical for geometrically similar chambers.

2) The dimensionless aerodynamic resistance of a cyclone chamber decreases with an increase of the inlet area and the contraction ratio.

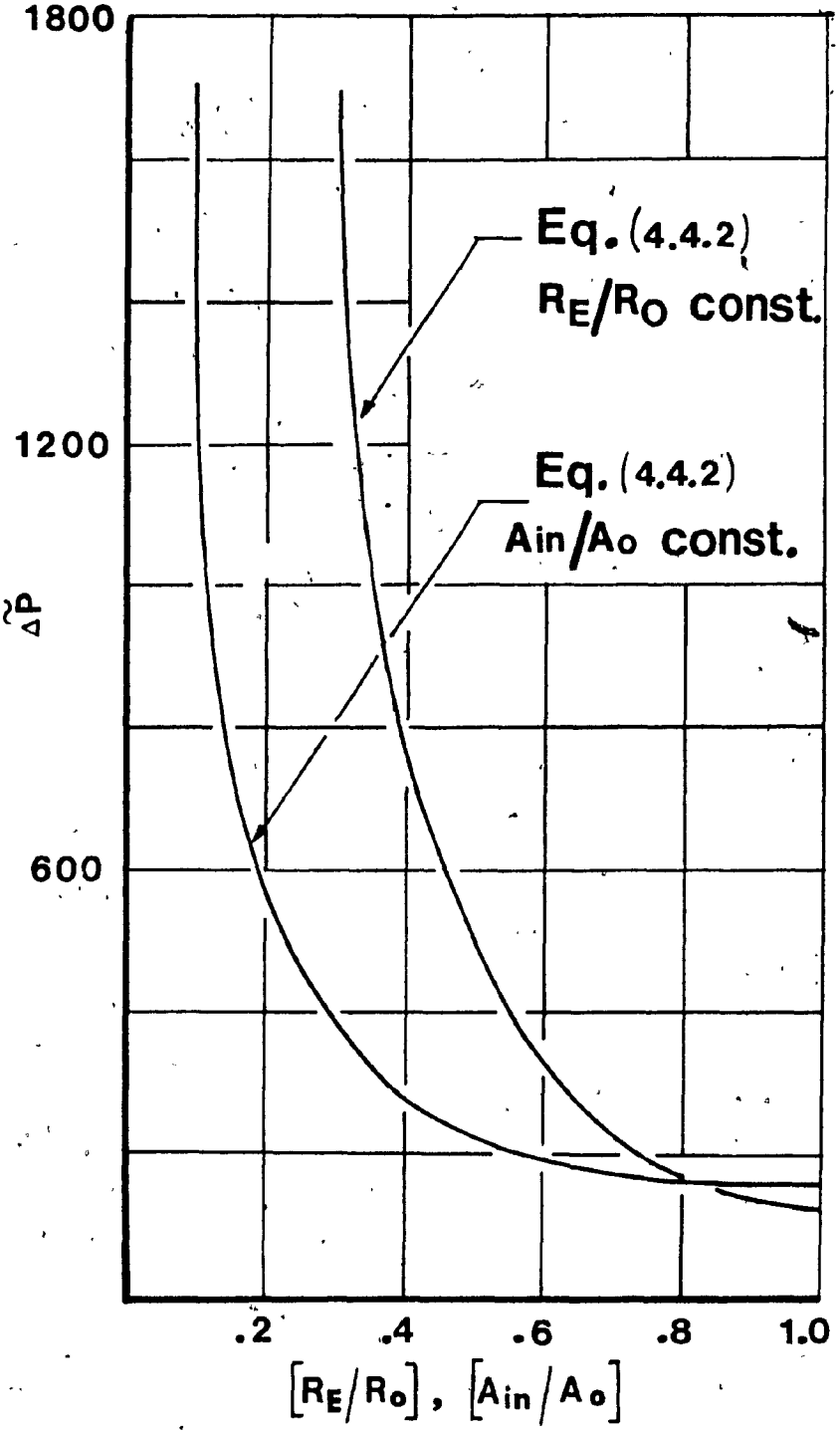

Fig. 4.4.1: $\tilde{\Delta P}$ vs. $[R_E/R_o]$ and $[A_{in}/A_o]$.

The first conclusion is evident from the eq. (4.4.3). Since $Eu(R_E/R_o, A_{in}/A_o, X_{CO}(a), \phi)$ does not depend on the absolute dimensions of the chamber, the dimensionless aerodynamic resistance is the same for geometrically similar chambers. The second experimental fact is clear from Fig. (4.4.1). Styles et al [70] also arrived at the same experimental conclusions.

4.5 Experimental Velocity Map within the Chamber

There are many difficulties associated with the radial velocity deduction from the experimentally obtained pitot-probe pressure difference data. As previously mentioned in Chapter 3, this velocity component is under the shadow of the large tangential velocity. In addition, there is a static pressure interference which has values of the same order of magnitude with the pressure difference $P_4 - P_5$, see Fig. (3.1.4),($P_4 - P_5$ makes the determination of the radial velocity possible). It has been shown in previous sections, that a static pressure field is developed inside the chamber, mainly to balance the centrifugal forces. Although the spacing of the pressure taps 4 and 5 (Δr = 1.5 mm) is indeed small, a probe immersed in the flowfield will read a pressure difference, $P_4 - P_5$, even if there is no radial velocity. For this reason, a correction due to this interference must be effected.

From eqs. (4.3.6) and (4.3.7) one can approximately obtain the necessary pressure difference correction Δh_c,

$$\Delta h_c = \left[\frac{\left(\frac{\Delta r}{R_o}\right)\left(\frac{r}{R_o}\right)}{\left(\frac{R_E}{R_o}\right)^4 X_{CD}^4}\right] \left(\frac{\rho_{air}}{\rho_{water}}\right) \frac{V_{rin}^2 \cot^2\phi}{g} \qquad (4.5.1)$$

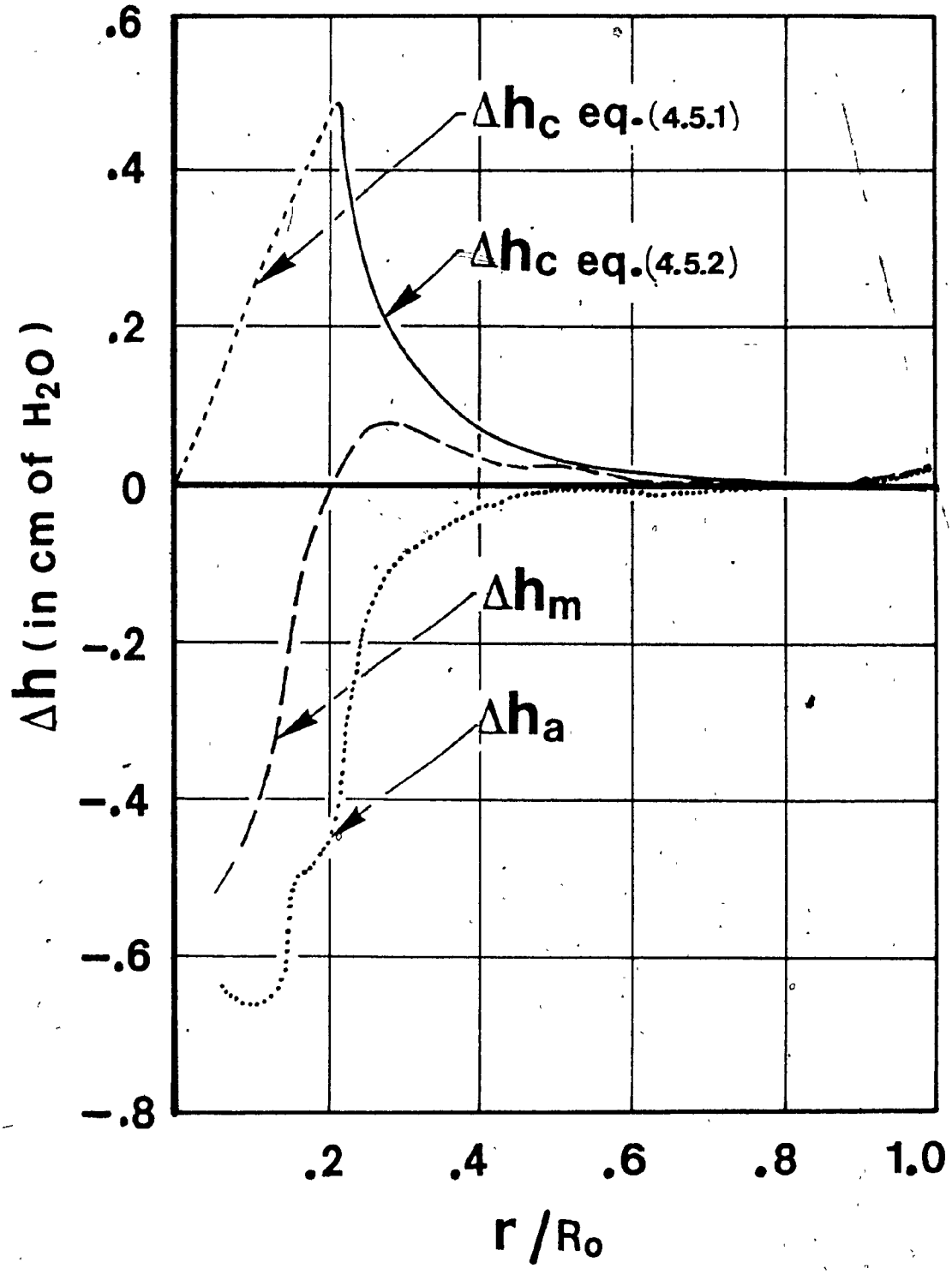

Fig. 4.5.1: Difference in Head Between Taps 5 and 4 of the Pitot-Probe (Δh_m = measured, Δh_c = correction, Δh_a = actual).

for $0 \leq \frac{r}{R_o} \leq \frac{R_{CD}}{R_o}$

and,

$$\Delta h_c = \left[\frac{V_{rin} \cot \psi}{\left(\frac{r}{R_o}\right)^2 - \frac{1}{4}\left(\frac{\Delta r}{R_o}\right)^2}\right] \left(\frac{\Delta r}{R_o}\right) \frac{\rho_{air}}{\rho_{water}} \left(\frac{r}{R_o}\right) \qquad (4.5.2)$$

for $\frac{R_{CD}}{R_o} \leq \frac{r}{R_o} \leq 1.0$

where,

$$\Delta h_c = (h_4 - h_5)_c = \frac{(P_4 - P_5)_c}{\gamma_{water}}$$

$$\gamma_{water} = \rho_{water}\, g.$$

It can be seen from Fig. (4.5.1), that the measured pressure difference $\Delta h_m = (h_4 - h_5)_m$, is of the same order of magnitude with the interfering static pressure Δh_c. Correcting the experimental results, the actual $\Delta h_a = (h_4 - h_5)_a$ is so small for $0.4 \leq \frac{r}{R_o} \leq 1.0$, that the values of the radial velocity in this region are uncertain For this reason, no radial velocity distributions inside the chamber are presented. Failing to effect this correction to the other velocities will produce no significant error.

The tangential velocity profiles in the chamber were presented and discussed in previous sections. The radial profiles of the dimensionless axial velocity are presented in a series of Figs. (4.5.2) to (4.5.6). All profiles possess two positive velocity peaks; one near the circumferential wall and the other in the neighborhood of the exit radius R_E. Two

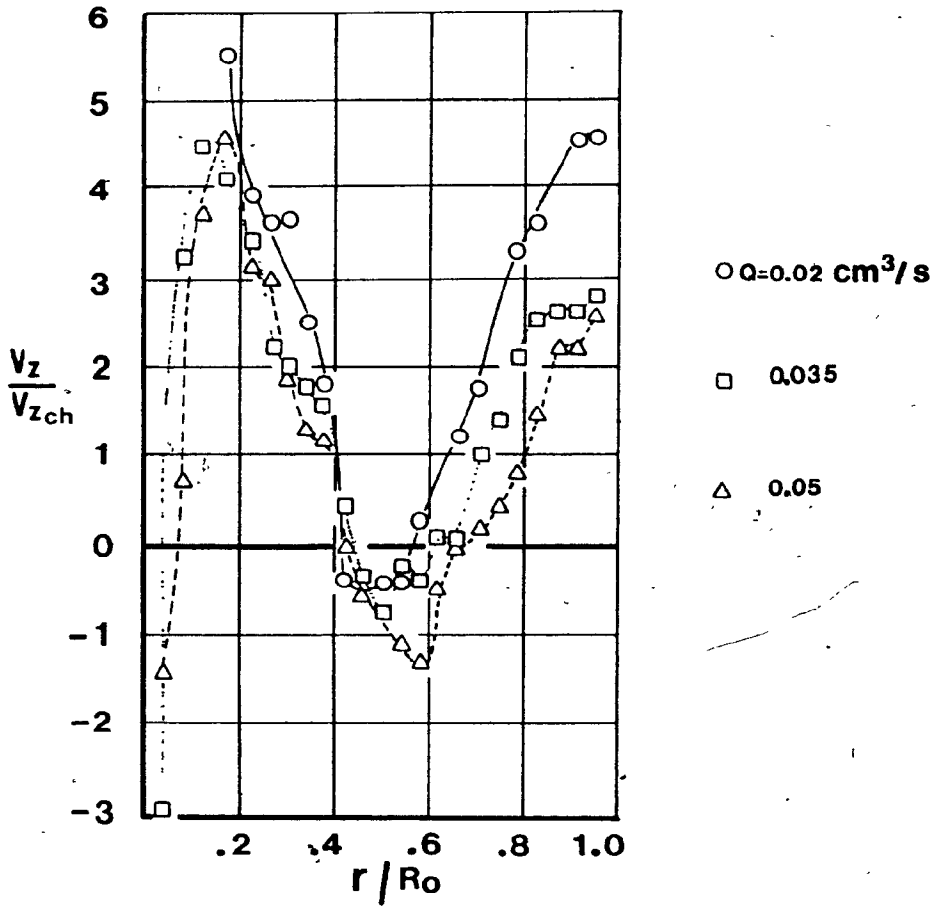

Fig. 4.5.2: Dimensionless Axial Velocity vs. Radius for the Axial Station $\bar{z}_2 = 0.285$.

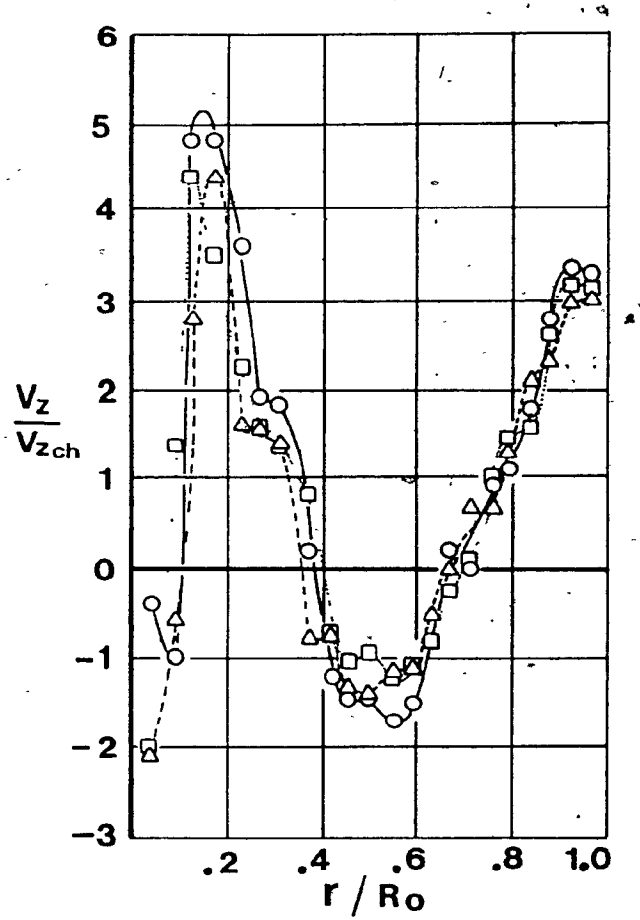

Fig. 4.5.3: Dimensionless Axial Velocity vs. the Radius for the Axial Station $\bar{z}_3 = 0.396$.

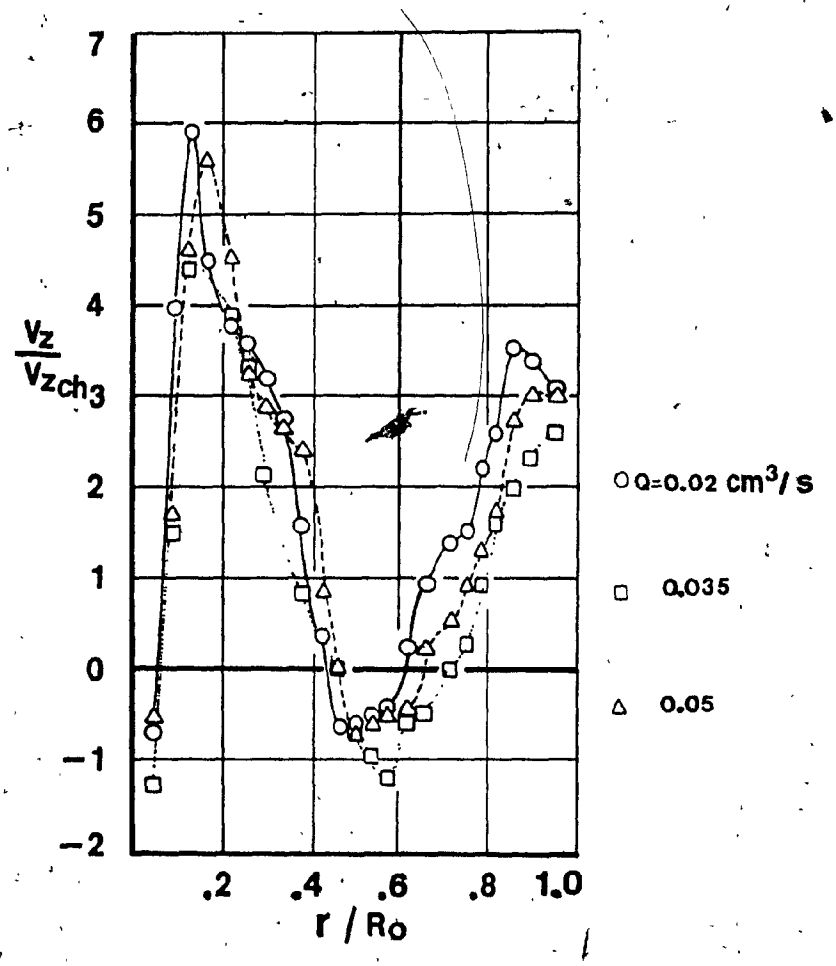

Fig. 4.5.4: Dimensionless Axial Velocity vs. the Radius for the Axial Station $\bar{z}_4 = 0.510$.

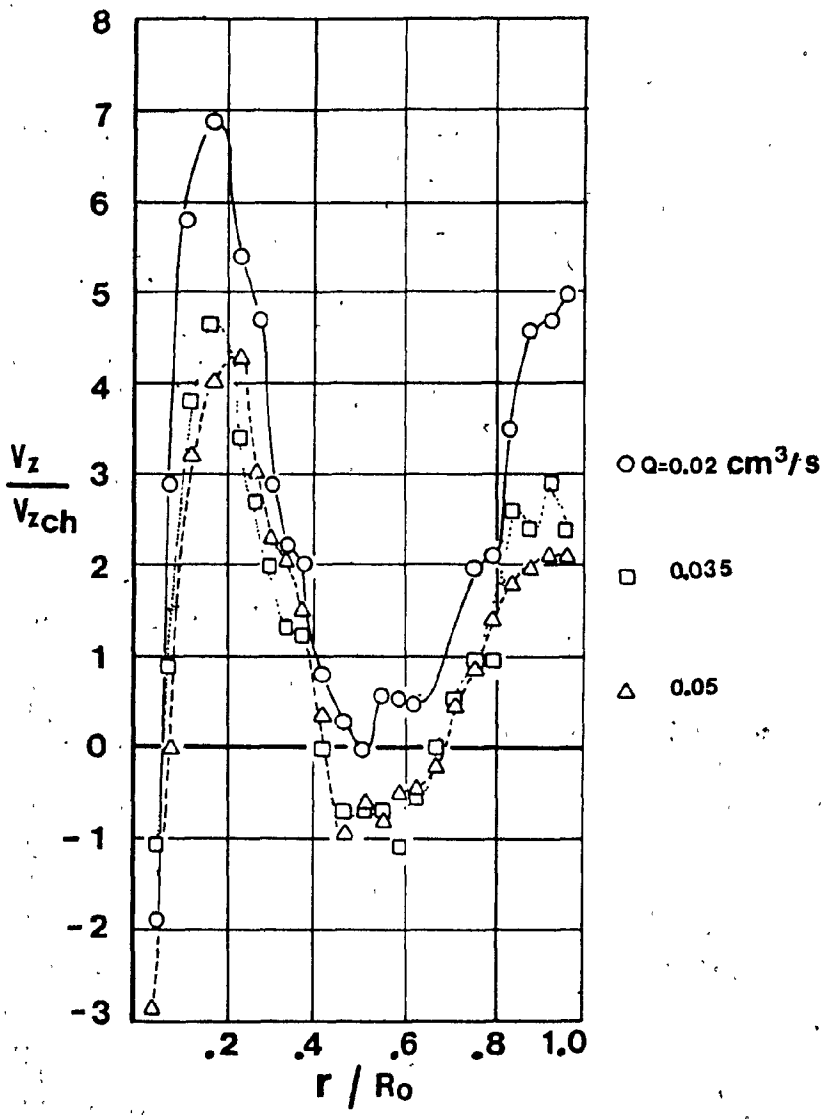

Fig. 4.5.5: Dimensionless Axial Velocity vs. the Radius for the Axial Station $\bar{z}_s = 0.618$.

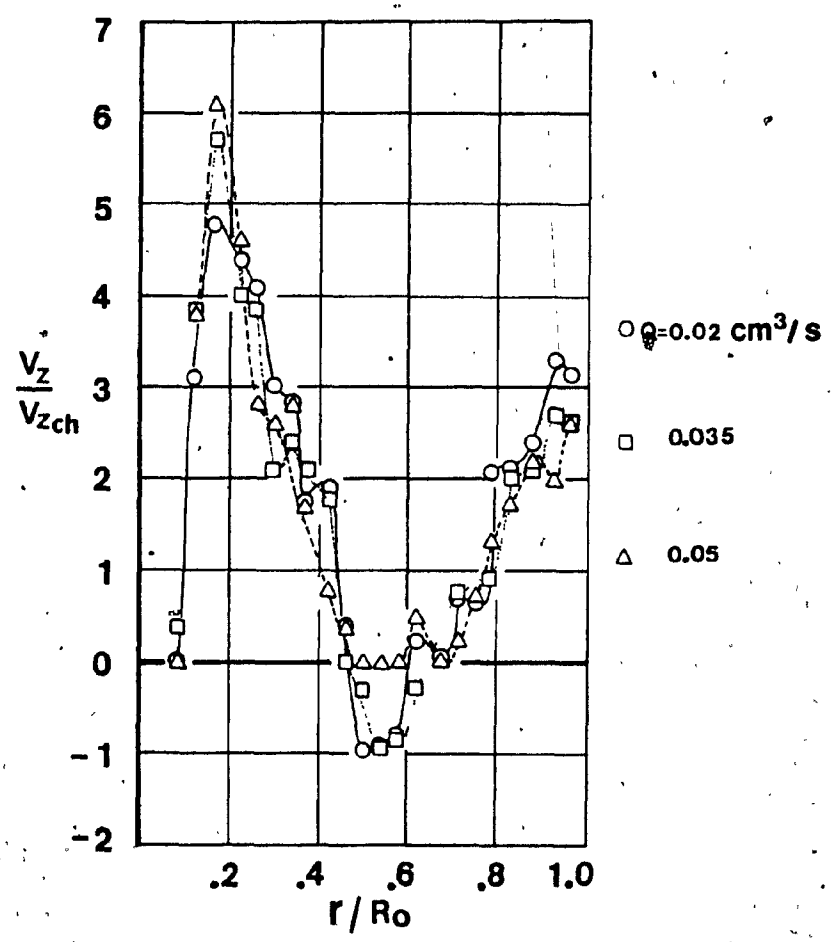

Fig. 4.5.6: Dimensionless Axial Velocity vs. the Radius for the Axial Station $\bar{z}_6 = 0.729$.

negative velocity areas exist; one due to the entrained flow near the axis of symmetry, the other in the area where the annular secondary flow is taking place. Let us consider the flow near the bottom plate. Inside the boundary layer the azimuthal velocity is reduced gradually to zero. The static pressure inside the boundary layer is the same as that outside. However, the static pressure inside the boundary layer no longer balances the centrifugal force. This static pressure deficit drives inwards part of the fluid supplied by the inlet port. The stream will continue to flow towards the centerline until it meets the entrained stream. At this point, the two streams combine, change direction, and flow towards the exit, producing the positive axial velocity peak near $r/R_o = 0.2$. Most of the fluid at the inlet unable to flow through the bottom plate, decides to find the outlet following closely along the cylindrical wall. In doing so, the path chosen presents no major centrifugal opposition. The latter explains the positive axial velocity peak near the circumferential wall. Taylor-Goertler [71,72] vortex flow, arising from the monotonically decreasing tangential velocity [51,73] is also expected to be present very near the circumferential wall.

4.6 The Reverse Flow Radius Inside the Core

For sufficiently large inlet swirl numbers, a reverse flow near the exit and close to the axis or rotation is present. The vacuum created inside the core, due to rotation drives the ambient air into the chamber. From the experimental results of Kwok [29], one notices that the static pressure outside the core radius R_{CO} is approximately equal to the ambient. Inside the core, the static pressure decreases noticeably. The parabolic profile of the pressure close to the axis of

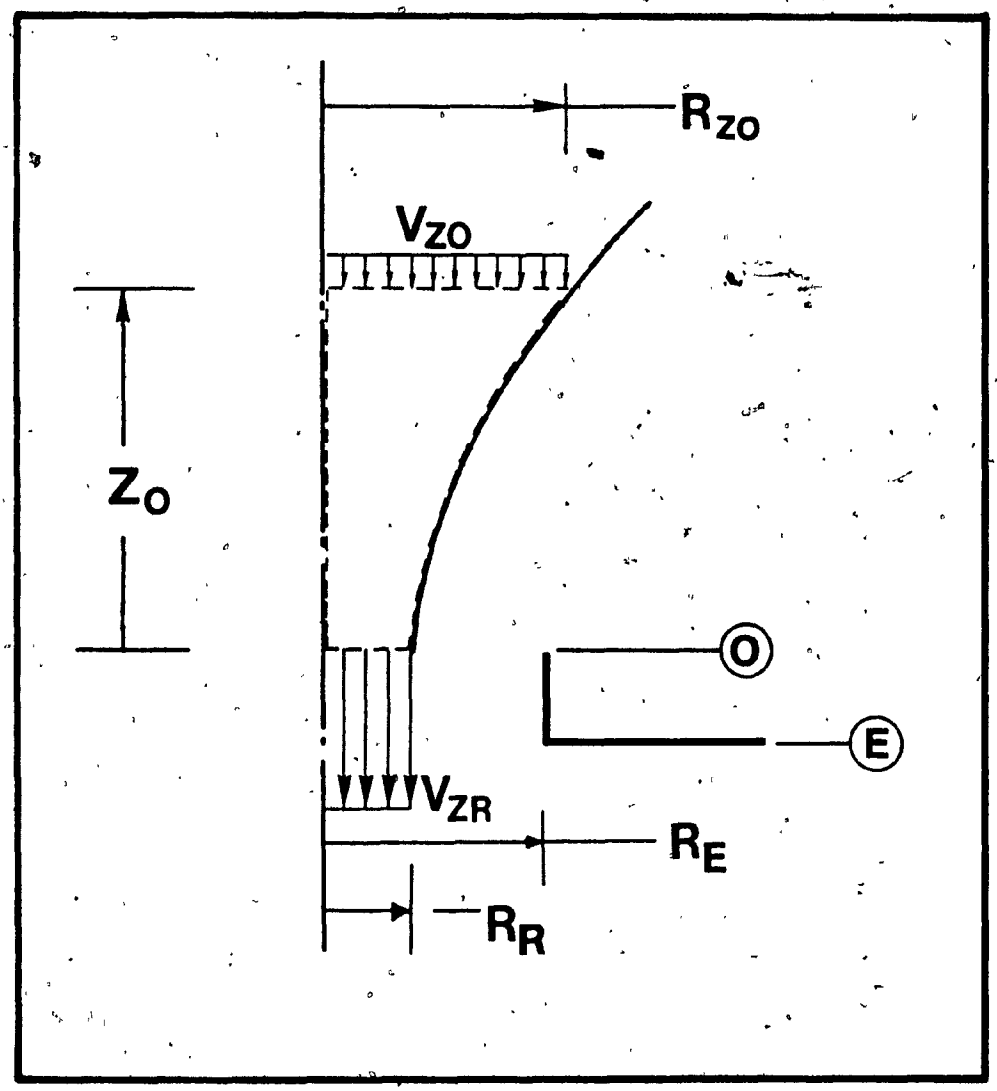

Fig. 4.6.1: Artificial Depiction of the Entrained Flow at the Outlet.

symmetry, suggests a strong influence of the pressure by the solid body rotation. If a funnel effect is assumed to take place, the reverse flowfield must resemble that of Fig. (4.6.1). The radial velocity at $Z_0 = 0$ will be approximately zero while a large average axial velocity V_{ZR} must be present. If the static pressure at $r = R_{CO}$ is P_a, it will be below the ambient in the interval $[0, R_{CO}]$.

$$P_R(r) = \frac{\rho m^2}{2} (r^2 - R_{CO}^2) + P_a \qquad (4.6.1)$$

where,

$$m = \frac{\Gamma}{2\pi R_{CO}^2}$$

As $Z_0 \to \infty$, $P_{ZO} \to P_a$ and $V_{ZO} \to 0$.

The energy equation (4.2.11) for the control volume shown in Fig. (4.6.1) by dashed lines is,

$$\lim_{Z_0 \to \infty} \iint_{A_{ZO}} \left(P_{ZO} + \rho \frac{q_{ZO}^2}{2}\right) V_{ZO}\, d A_{ZO} = \iint_{A_R} \left(P_R + \rho \frac{q_R^2}{2}\right) V_{ZR}\, d A_R + \mathring{F} \qquad (4.6.2)$$

The left hand side integral gives,

$$\lim_{Z_0 \to \infty} \iint_{A_{ZO}} \left(P_{ZO} + \rho \frac{q_{ZO}^2}{2}\right) V_{ZO}\, d A_{ZO} = P_a Q_R$$

Then eq. (4.6.2) becomes,

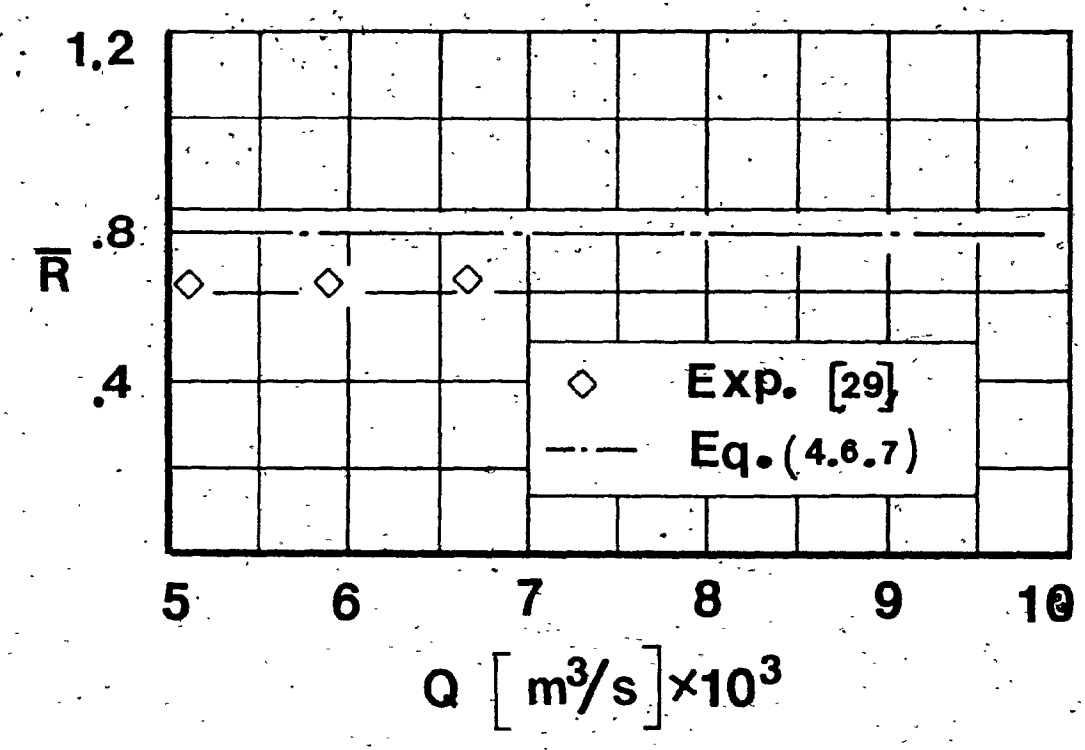

Fig. 4.6.2: The Reverse Flow Radius vs. the Inlet Volumetric Flowrate for $R_E/R_0 = 0.1$.

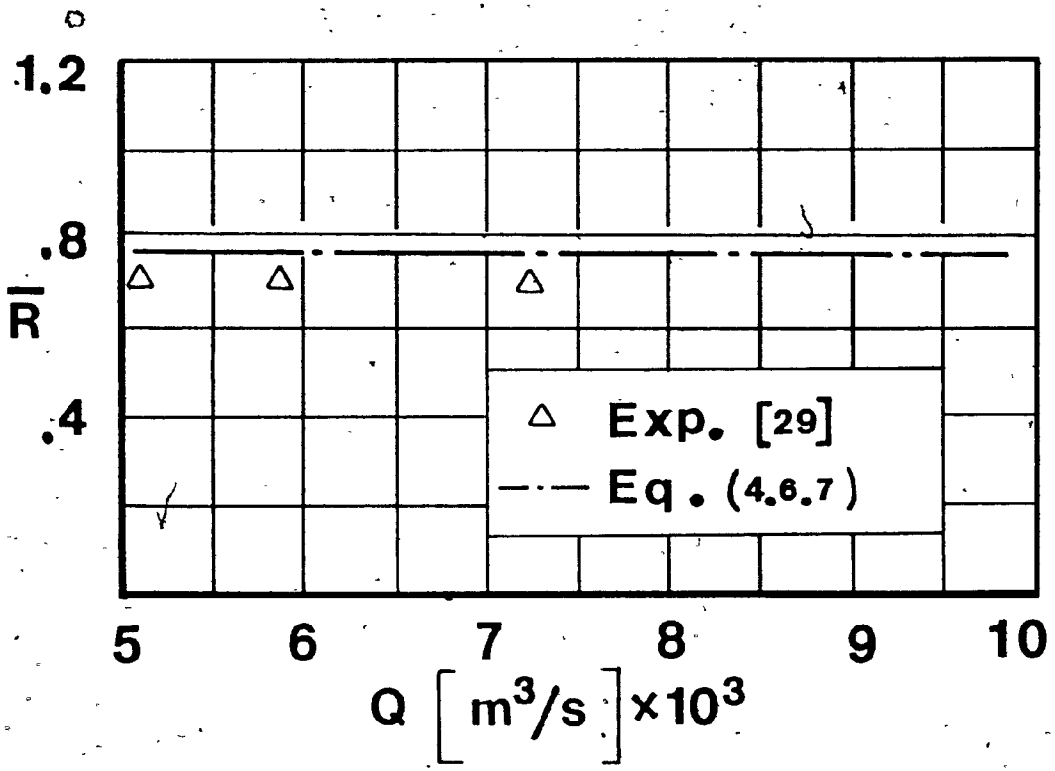

Fig. 4.6.3: The Reverse Flow Radius vs. the Inlet Volumetric Flowrate for $R_E/R_o = 0.15$.

$$\iint_{A_R} \left(P_R + \rho \frac{q_R^2}{2}\right) V_{ZR}\, d A_R = P_a Q_R - \dot{F} \qquad (4.6.3)$$

Incorporating eq. (4.6.1) into (4.6.3) yields,

$$\int_0^{R_R} \left(P_a + \rho \frac{m^2}{2}(r^2 - R_{CO}^2) + \frac{\rho}{2} q_R^2\right) 2\pi V_{ZR} r dr = P_a Q_R - \dot{F} \qquad (4.6.4)$$

where,

$$q_R^2 = V_R^2 + m^2 r^2.$$

$\dot{F}$ is the rate of energy which is lost to friction in bringing the fluid from "infinity" into the chamber. To evaluate $\dot{F}$ the detailed fluid structure inside the control volume is required. In this analysis $\dot{F}$ is neglected. Performing the integration in eq. (4.6.4) followed by a series of algebraic manipulations one obtains,

$$V_R = m\sqrt{R_{CO}^2 - R_R^2} \qquad (4.6.5)$$

From continuity,

$$V_R = \frac{Q_R}{\pi R_R^2}$$

and eq. (4.6.5),

$$Q_R = \pi m R_E^3 \bar{R}^2 \sqrt{(X_{CO}^2 - \bar{R}^2)} \qquad (4.6.6)$$

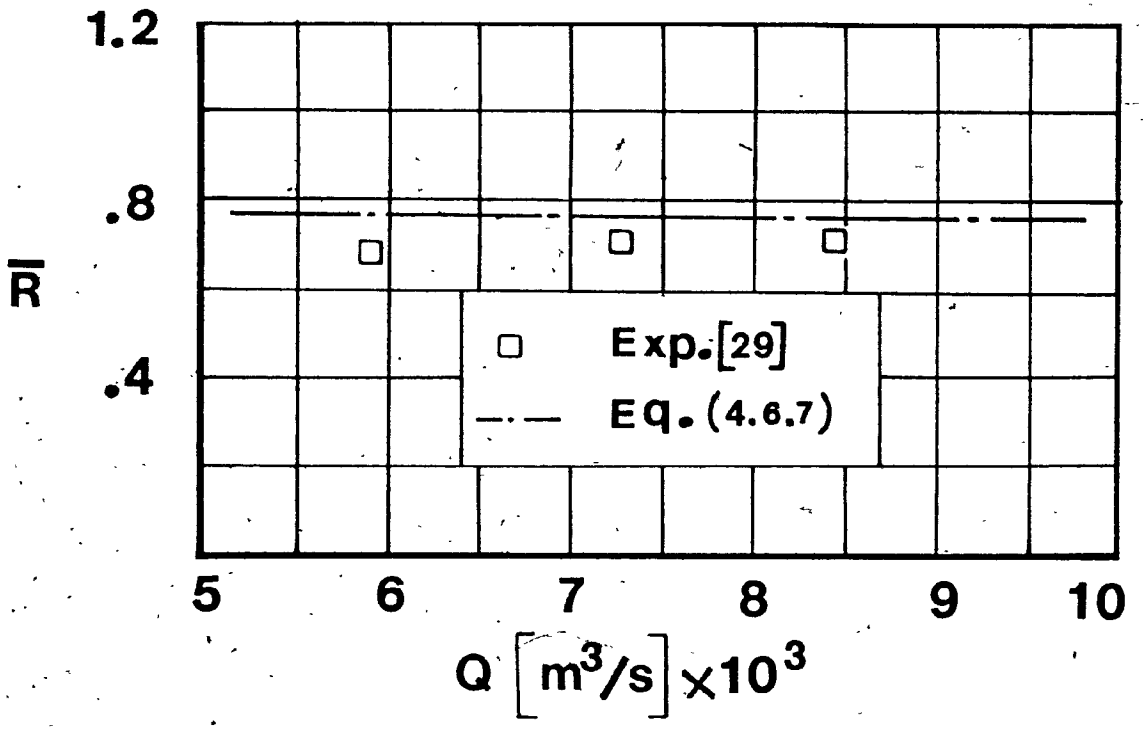

Fig. 4.6.4: The Reverse Flow Radius vs. the Inlet Volumetric Flowrate for R_E/R_o = 0.2.

where,

$$\bar{R} = \frac{R_R}{R_E}$$

Study of eq. (4.6.6) shows that;

(i) $\bar{R} \to 0$, $Q_R \to 0$

(ii) $\bar{R} \to X_{CO}$, $Q_R \to 0$.

Therefore, there must exist an $\bar{R}$ in $(0, X_{CO})$ where Q_R attains a maximum value. This is given by,

$$\bar{R} = 0.816\, X_{CO} \qquad (4.6.7)$$

If indeed $\bar{R}$ is equal to $0.816\, X_{CO}$, it must not be a function of the inlet volumetric flowrate. This deduction is evident from the figures (4.6.2) - (4.6.4). The agreement of the experimental results of Kwok [29] with eq. (4.6.7) is reasonable. There is only an approximate 10% difference between the theory and the experiment. On the other hand, $\bar{R}$ must vary with the inlet swirl number. In Fig. (4.6.5) this effect is investigated. Experimental evidence [Ref. 27], shows that a "dimp" is developed in the axial velocity near the axis when swirl is applied, which grows as the swirl is enhanced. Eventually, if the swirl strength increases sufficiently, the "dimp" will develop into a reverse flow. Equation (4.6.7) indicates that a reverse flow will be present even with a very small swirl. In this respect, the present theory fails. The reason lies in the viscous effects which were neglected. However, if the reverse flow is present, eq. (4.6.7) predicts well the real case.

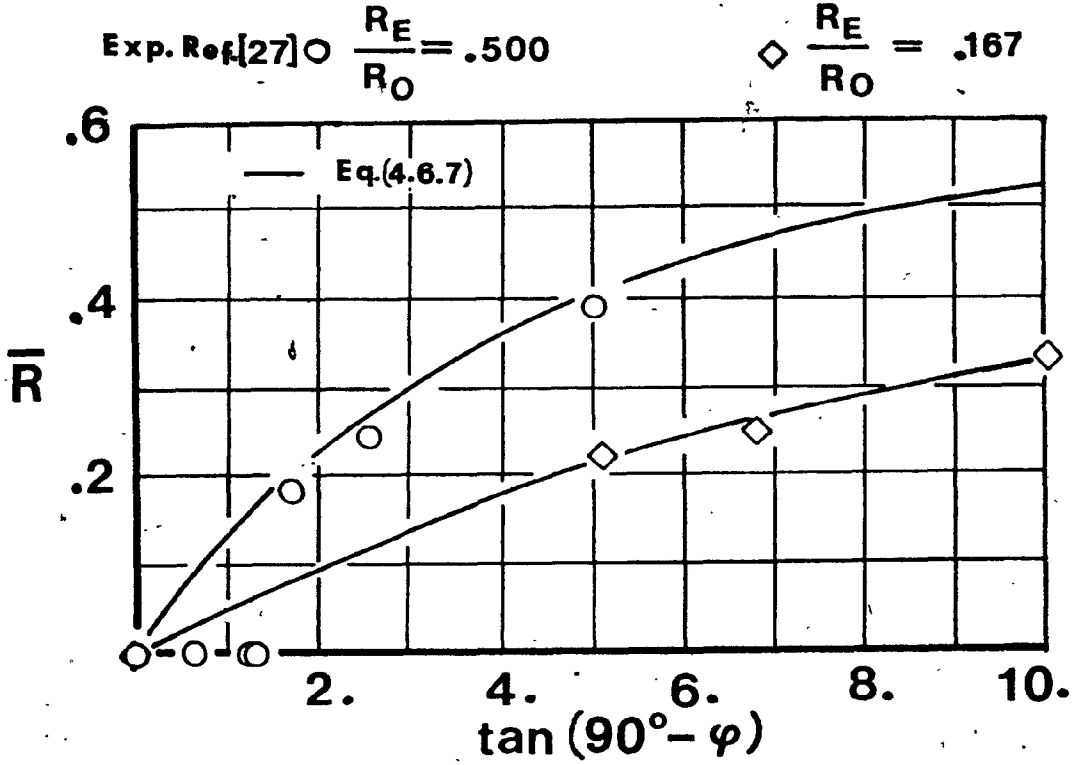

Fig. 4.6.5: The Reverse Flow Radius vs. the Inlet Swirl.

4.7 On the Reduction of Pressure Drop Across the Vortex Chambers

In Fig. (4.3.5), the dimensionless pressure drop across the chamber vs. the contraction ratio was presented. Their hyperbolic relation shows a drastic pressure drop for small values (R_E/R_o) as the effective exit area decreases. In addition, the strong dissipative source due to vigorous mixing of the ambient air and the exhausting vortex flow, plus the energy loss in bringing the entrained flow from "infinity" into the chamber, enhance further $\overline{\Delta P}$. Consider the energy balance over the control surface of Fig. (4.7.1),

$$\dot{E}_{in} = \Delta\dot{E}_R + \dot{E}_O + \dot{F} \tag{4.7.1}$$

where,

$$\Delta\dot{E}_R = \dot{E}_{RO} - \dot{E}_{Rin}$$

If we assume that $Q_{Rin} = Q_{RO}$ and $Q = Q_O$, $\Delta\dot{E}_R$ must be greater than zero to reflect the fact that, energy dissipated in bringing the entrained flow from outside, must be supplied at the inlet. Using a plug to prevent the reverse flow from taking place, gives,

$$\dot{E}_{in}' = \dot{E}_O + \dot{F}' \tag{4.7.2}$$

In the absence of the violent mixing of the entrained and exhausting flows, it is possible to produce an $\dot{F}'$ which is smaller than $\dot{F}$. From the above, $\dot{E}_{in}'$ must then be smaller than $\dot{E}_{in}$. Therefore plugging the flow at the exit could cause a reduced $\overline{\Delta P}$ for the same inlet volumetric flowrate. The latter hypothesis is confirmed by the experimental results shown in Fig. (4.7.2). As the conical plug is lowered, partial reduction of the reverse flow is achieved, which is manifested by a corresponding reduction

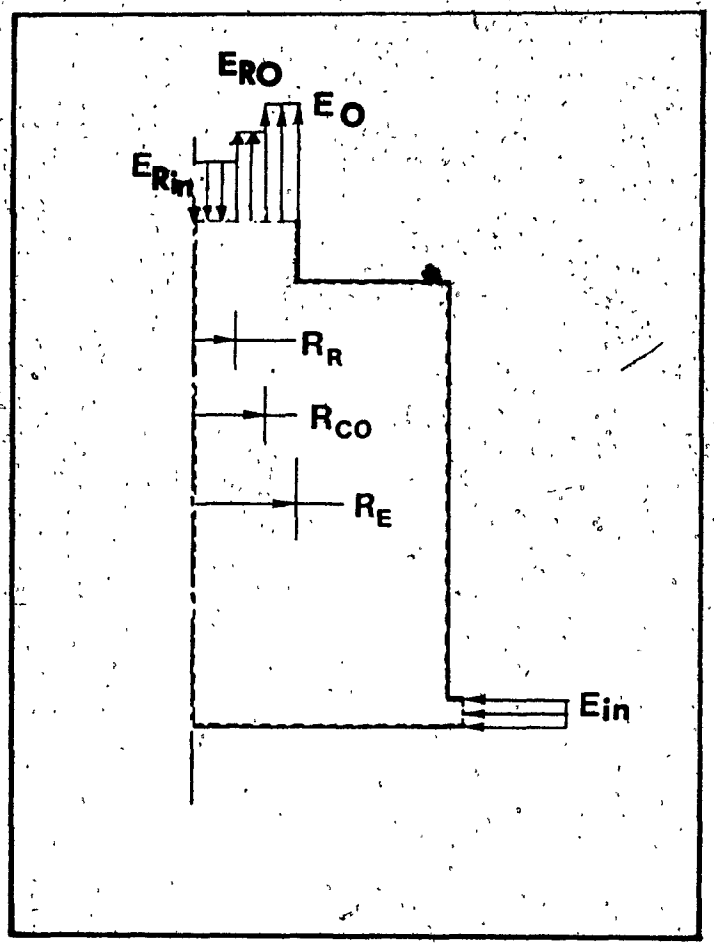

Fig. 4.7.1: Overall Energy Distribution.

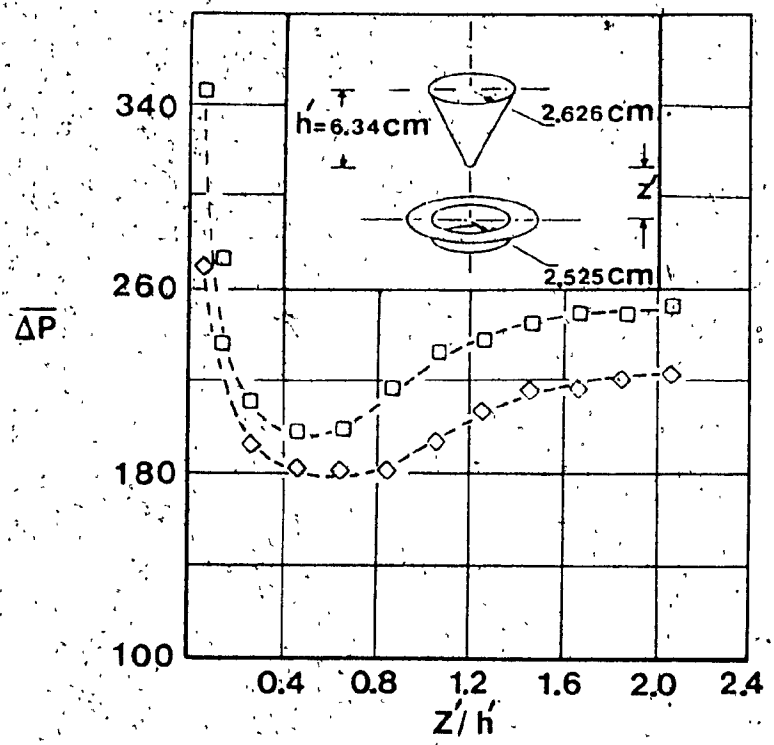

Fig. 4.7.2: Pressure Drop Across the Chamber vs. Plug Position (□, Q = 0.035 m^3/s ◇, Q = 0.050 m^3/s).

in static pressure drop across the chamber. When the optimum position of the cone is reached, $\overline{\Delta P}$ is at its minimum. Any further decrease of (Z'/h'), from the optimum, results in a drastic increase of $\overline{\Delta P}$, as the solid plug virtually covers the outlet area beyond the core. It is also worthwhile to mention that the noise level reduces considerably as the optimum "plug" position is reached. However the noise continues to decrease past (Z'/h') opt.

A tube with smoke supply was inserted in various key places of the flowfield near the exit, without and with the plug at optimum position. With an undisturbed exit flow, the smoke was drawn into the chamber and mixed violently with the internal flow. With the plug in optimum position, smoke supplied near the top of the cone never found a way into the chamber. Inside the core, a secondary flow is still present but its strength has been diminished. With the minimal mixing of the ambient and internal flows a 17% pressure drop reduction was possible. This is the case for a contraction ratio equal to 0.16. However, the effectiveness of the plug was found to vary with R_E/R_o. For example, if R_E/R_o is equal to 0.2 only a 5% reduction of $\overline{\Delta P}$ is possible, and for 0.3 the reduction is hardly significant. This is not an unexpected outcome. The intensity of the reversed flow depends on the magnitude of the vacuum created within the chamber. This in turn is affected by the size of the exit port, since the latter controls the point of maximum velocity which always occurs at a radius smaller than R_E. Therefore, to reduce $\overline{\Delta P}$ via a plug, the contribution of the reverse flow on the overall flowfield pressure drop must become significant.

The optimum $\overline{\Delta P}$ was found not to be affected by the geometry of

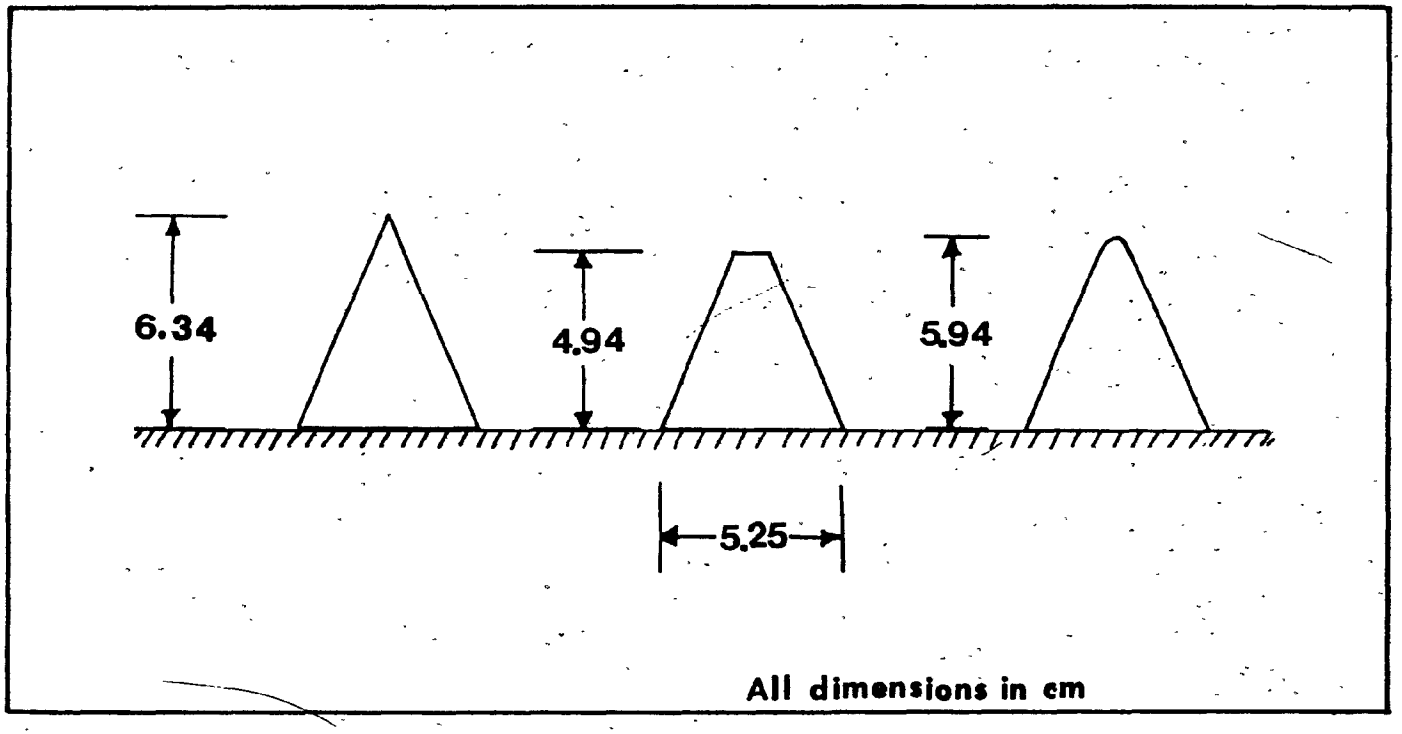

Fig. 4.7.3: Different Tip Configuration of the Cone.

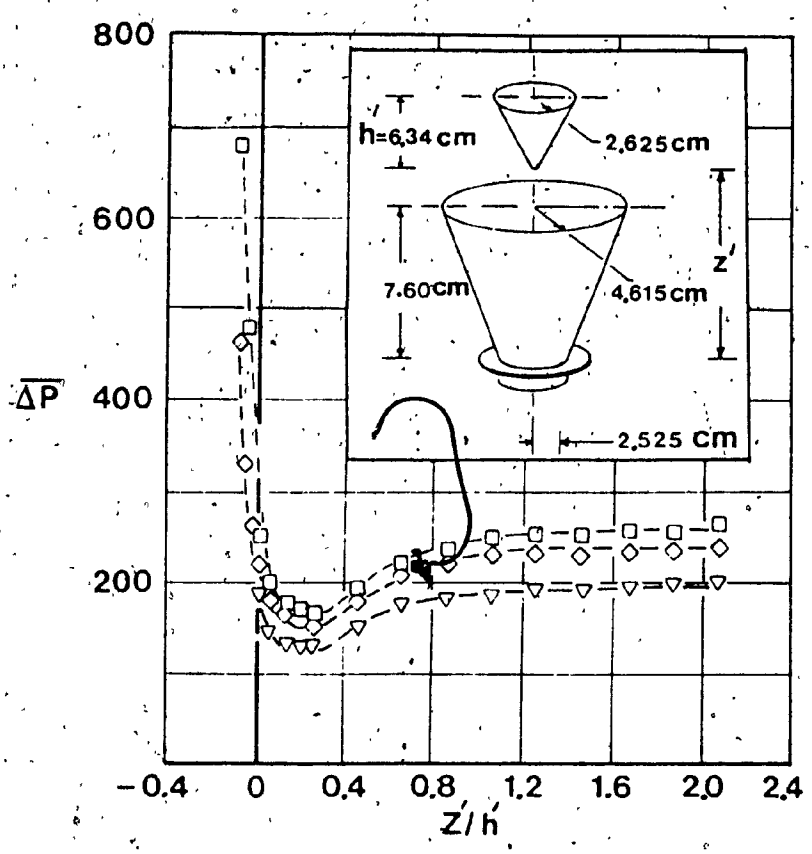

Fig. 4.7.4: Pressure Drop Across the Chamber vs. Plug Position with Diffuser (□, Q = 0.035 m^3/s, ◇, Q = 0.050 m^3/s, Δ, Q = 0.066 m^3/s).

the tip of the cone. Different tip geometries tested are given in Fig. (4.7.3). However, the optimum $\overline{\Delta P}$ is found to be further reduced by a combination of a conical diffuser and a plug as Fig. (4.7.4) illustrates. It can be seen that, although $\overline{\Delta P}$ of the undisturbed exit flow is slightly higher than in Fig. (4.7.2) the possible percentage reduction of the pressure drop across the chamber is now approximately twice.

CHAPTER 5

APPROXIMATE AIR VELOCITY MAPPING IN THE VORTEX CHAMBER

CHAPTER 5

APPROXIMATE AIR VELOCITY MAPPING IN THE VORTEX CHAMBER

Confined vortex flows possess theoretical difficulties which are not present in other flowfields. The dominating azimuthal fluid motion and the secondary flows in the chamber, make even a numerical flow-pattern characterization a formidable endeavour indeed. Here, consideration is given to an approximate solution of the viscous equations of fluid motion in a vortex chamber. To obtain the solution, the extended two-dimensional axisymmetric Los Alamos Sola numerical algorithm [74] was used, borrowing also some ideas from the Imperial College TEACH Program [45]. The former treats the transient case, while the latter, the steady state directly.

The solutions obtained show velocity distributions inside the vortex chamber. The difference between viscous and potential results are outlined. The numerical simulation of the flowfield is found to be conformal qualitatively using previously known experimental facts.

5.1 The Mathematical Model

A schematic of the mathematical model used to simulate the physical problem is illustrated in Fig. (5.1.1). Fluid, of uniform velocity, is admitted into the chamber through swirl vanes which regulate the vortex strength and are located around the lower periphery of the cylindrical wall. The outlet port is placed in the middle of the upper plate.

The equations describing the fluid motion in conservative form, i.e. in terms of the divergence of momentum flux, are,

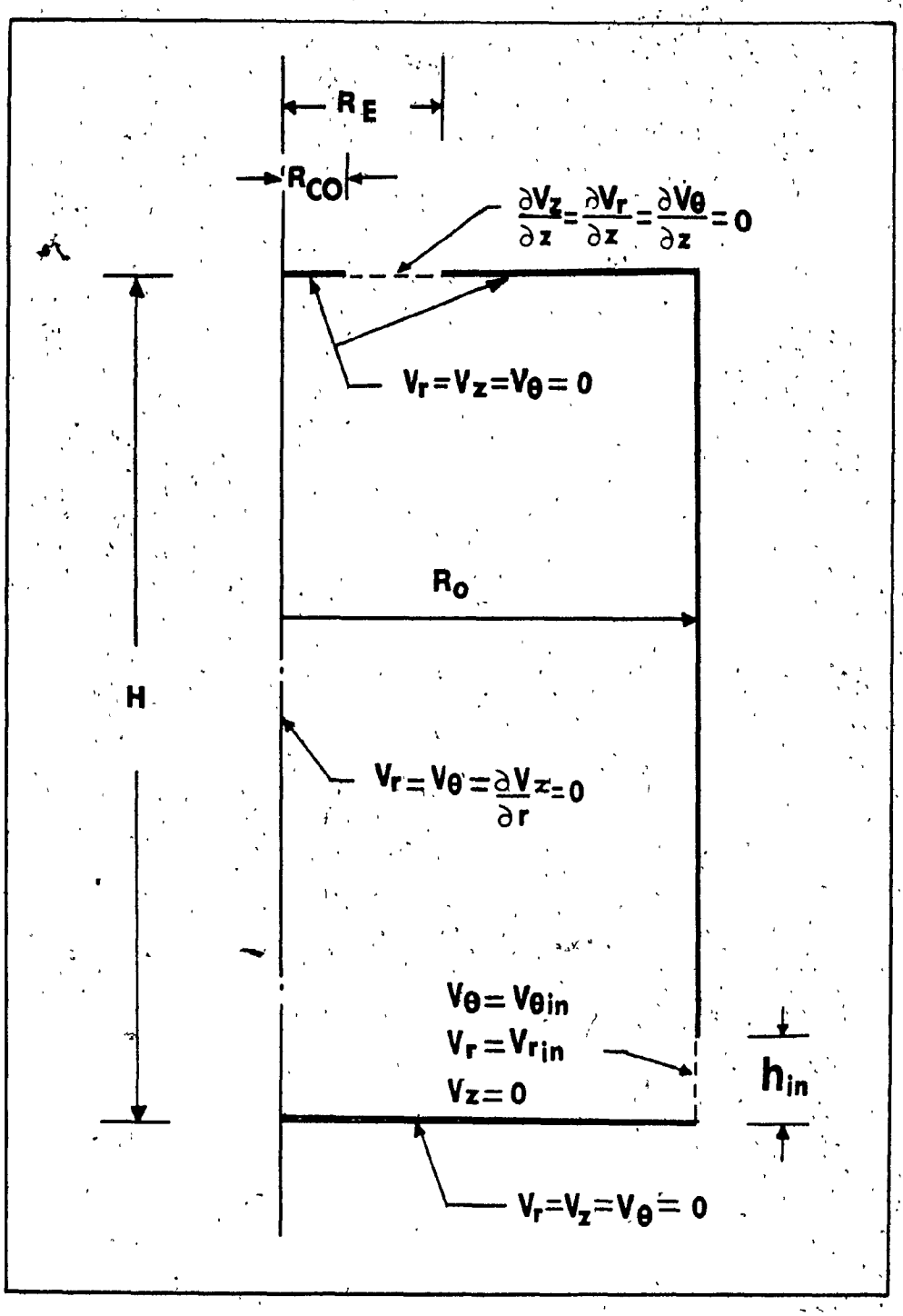

Fig. 5.1.1: Mathematical Model of the Vortex Chamber.

r-momentum

$$\frac{\partial V_r}{\partial t} + \frac{\partial V_r^2}{\partial r} + \frac{\partial V_r V_z}{\partial z} + \frac{V_r^2 - V_\theta^2}{r} = -\frac{\partial \hat{P}}{\partial r} + \nu \left[\nabla^2 V_r - \frac{V_r}{r^2}\right] \qquad (a)$$

θ-momentum

$$\frac{\partial V_\theta}{\partial t} + \frac{\partial V_r V_\theta}{\partial r} + \frac{\partial V_z V_\theta}{\partial z} + \frac{2 V_r V_\theta}{r} = \nu \left[\nabla^2 V_\theta - \frac{V_\theta}{r^2}\right] \qquad (b)$$

z-momentum

$$\frac{\partial V_z}{\partial t} + \frac{\partial V_r V_z}{\partial r} + \frac{\partial V_z^2}{\partial z} + \frac{V_r V_z}{r} = -\frac{\partial \hat{P}}{\partial z} + \nu \nabla^2 V_z \qquad (c)$$

continuity

$$\frac{\partial V_r}{\partial r} + \frac{V_r}{r} + \frac{\partial V_z}{\partial z} = 0 \qquad (5.1.2)$$

where,

$$\nabla^2 = \frac{\partial^2}{\partial r^2} + \frac{1}{r}\frac{\partial}{\partial r} + \frac{\partial^2}{\partial z^2}$$

and $\hat{P} = P/\rho$.

Preference of the conservative form of the momentum equations is based on accuracy reasons. It is known that this type of formulation results in more accurate computing methods [75]. The above equations are also true for an artificially enhanced viscosity in the flowfield to represent turbulence, see Appendix C. However, in this way, turbulence is incorporated into the model rather crudely; the flow is supposed to behave as a laminar flow with an artificially larger viscosity. Even so, the level of

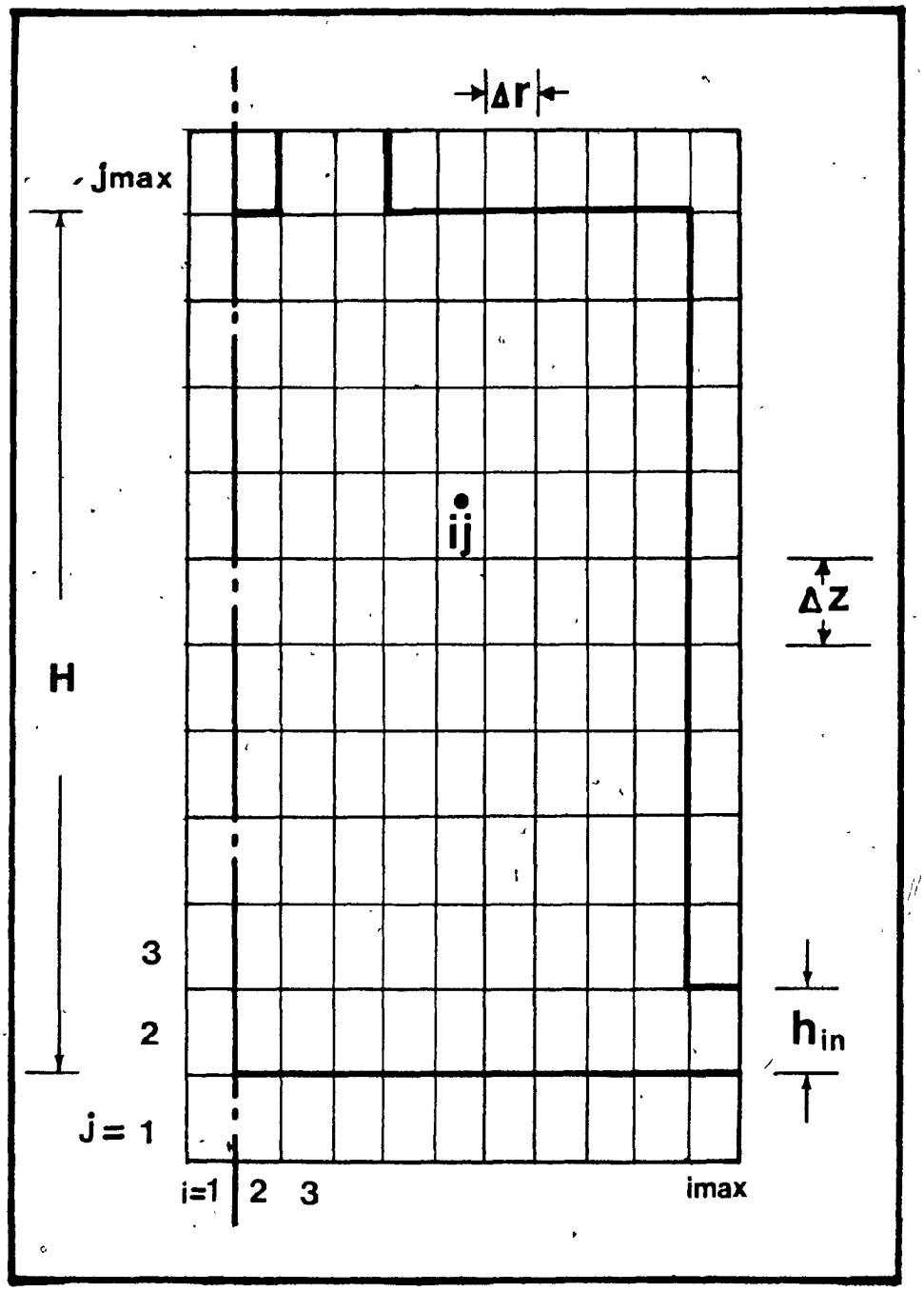

Fig. 5.2.1: The Grid System.

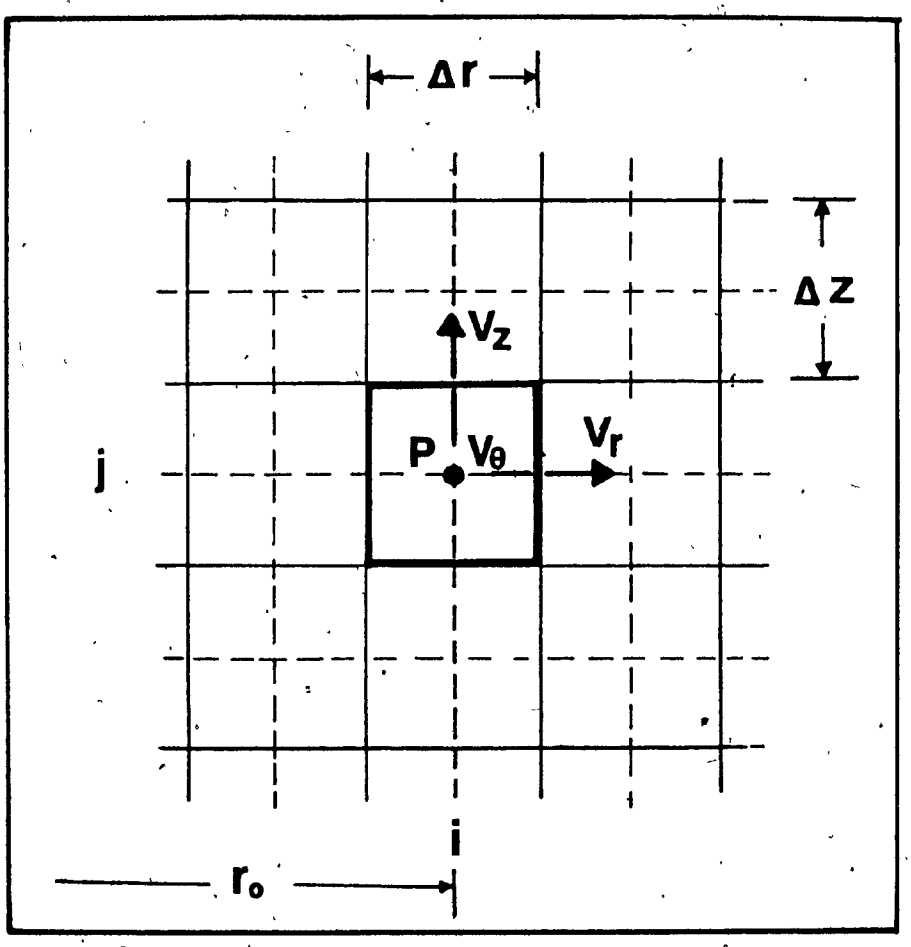

Fig. 5.2.2: Arrangement of Finite Difference Variables in a Typical Cell.

accuracy which resulted from this kind of assumption in a similar study [76], was quite satisfactory. Utilization of the so called "two equations" model of turbulence gave no significant improvements on the predicted flow. Modifications of the empirical constants to account for the bending of the streamlines, caused a distortion of the flowfield near the exit [8]. Although the "two equations" model has provided a good approximation to a variety of practical engineering problems, it fails in the presence of a dominant tangential velocity.

5.2 The Finite Difference Equations

Mathematically, the transport equations are parabolic in time and a transient time-marching technique is used here. The selection of the transient approach to study the steady-state condition of the present flowfield, came as a natural follow-up of previous work [76-78].

The grid system covering the domain of interest on a meridional plane appears in Fig. (5.2.1). A layer of fictitious cells on all sides surrounds the flow domain. In these cells the boundary conditions are stored. A single computational cell is magnified in Fig. (5.2.2) illustrating how the dependent variables are arranged. The values of static pressure and tangential velocity are stored in the center of each cell while the radial and axial velocities are displaced half a cell interval as shown. Thus, normal (to the wall) velocities lie directly on the physical boundaries, which simplifies the application of the boundary conditions.

Following the Los Alamos SOLA method, the momentum equations are discretized into a finite difference form. The method uses Forward-Time, Centered-Space (FTCS) explicit in time difference scheme. The usual one-

sided, first time derivatives and centered first and second derivatives are used in representing these equations. A certain amount of upstream differencing is given to the convective terms (donor cell method) to remove the inherent unconditional instability in case a small viscosity is used. That is, if V is any velocity component, the donor cell approach requires,

$$\frac{\partial V}{\partial r} = \begin{cases} \left.\frac{\partial V}{\partial r}\right|_{r_o} - \frac{\alpha \Delta r}{4} \left.\frac{\partial^2 V}{\partial r^2}\right|_{r_o} & \text{if } V_{i,j} \geq \frac{V_{i+1,j} + V_{i-1,j}}{2} \\ \left.\frac{\partial V}{\partial r}\right|_{r_o} + \frac{\alpha \Delta r}{4} \left.\frac{\partial^2 V}{\partial r^2}\right|_{r_o} & \text{if } V_{i,j} < \frac{V_{i+1,j} + V_{i-1,j}}{2} \end{cases}$$

A similar representation of the convective terms is applied on the z-direction. The coefficient α is a constant taking values in the interval [0,1]. A value of zero gives merely central differencing while a value of one gives full upstream differencing.

Therefore, the following are the difference equations representing the transport equations:

$$\begin{aligned} V_{r_{i,j}}^{n} &= V_{r_{i,j}} + \Delta t \left\{ \frac{1}{\Delta r} \left(\hat{P}_{i,j} - \hat{P}_{i+1,j} \right) + S_{i,j}^{V_r} \right\} \\ V_{\theta_{i,j}}^{n} &= V_{\theta_{i,j}} + \Delta t \, S_{i,j}^{V_\theta} \qquad (5.2.1) \\ V_{z_{i,j}}^{n} &= V_{z_{i,j}} + \Delta t \left\{ \frac{1}{\Delta z} \left(\hat{P}_{i,j} - \hat{P}_{i,j+1} \right) + S_{i,j}^{V_z} \right\} \end{aligned}$$

where,

$$S^{V_r}_{i,j} = - FVRR - FVRZ - FVRC + VISR$$

$$S^{V_\theta}_{i,j} = - FV\theta R - FV\theta Z - FV\theta C + VIS\theta$$

$$S^{V_z}_{i,j} = - FVZR - FVZZ - FVZC + VISZ.$$

and the source terms FVRR, FVRZ, etc are defined in Appendix D. Superscripts blank and n are used to denote values at time-level t and $t+\Delta t$ respectively.

Although eq. (5.2.1) enables one forward time-step to be accomplished, the newly calculated velocities will not, in general, satisfy the continuity requirement, expressed in central finite form,

$$\frac{1}{\Delta r}\left(V^n_{r_{i,j}} - V^n_{i-1,j}\right) + \frac{1}{\Delta z}\left(V^n_{z_{i,j}} - V^n_{z_{i,j-1}}\right)$$

$$+ \frac{1}{2\Delta r(i-1.5)}\left(V^n_{r_{i,j}} + V^n_{r_{i-1,j}}\right) = 0 \qquad (5.2.2)$$

This incompressibility constraint is imposed by iteratively adjusting the cell pressure. That is, if the divergence, div, of a cell is positive, there is a net flow emanating from that cell. This is corrected by reducing the cell pressure. On the other hand if div < 0, an increase in pressure is necessary.

When the cell pressure changes by $\Delta\hat{P}$, the velocity components on the four faces must be adjusted according to,

$$
\begin{aligned}
V_{r_{i,j}}^{n,\ell+1} &= V_{i,j}^{n,\ell} + \frac{\Delta t \Delta \hat{P}}{\Delta r} \\
V_{r_{i-1,j}}^{n,\ell+1} &= V_{r_{i-1,j}}^{n,\ell} - \frac{\Delta t \Delta \hat{P}}{\Delta r} \\
V_{z_{i,j}}^{n,\ell+1} &= V_{z_{i,j}}^{n,\ell} + \frac{\Delta t \Delta \hat{P}}{\Delta z} \\
V_{z_{i,j-1}}^{n,\ell+1} &= V_{z_{i,j-1}}^{n,\ell} - \frac{\Delta t \Delta \hat{P}}{\Delta z}
\end{aligned}
\qquad (5.2.3)
$$

where ℓ and $\ell+1$ indicate previous and updated velocities respectively. Substituting eq. (5.2.3) into (5.2.2) and making a number of obvious rearrangements one obtains,

$$
\mathrm{div}^{\ell} = -2 \left(\frac{\Delta t \Delta \hat{P}}{\Delta r^2} + \frac{\Delta t \Delta \hat{P}}{\Delta z^2} \right)
$$

The divergence after the velocity correction is zero ($\mathrm{div}^{\ell+1} = 0$). Then the amount of pressure change is:

$$
\Delta \hat{P} = - \mathrm{div}^{\ell} / (2\Delta t \, (1/\Delta r^2 + 1/\Delta z^2)) \qquad (5.2.4)
$$

Pressure update iteration continues until the divergence of all the cells is less than some prescribed small positive quantity ε. An over-relaxation factor ω near 1.8 is often applied to eq. (5.2.4) to reduce the number of iterations.

5.3 Boundary Conditions

In the previous section, the finite difference equations approximating the governing partial differential equations were presented.

However, the values of the dependent variables on the boundaries must also be included. For this reason, a single layer of fictitious cells is placed around the flow region thus utilizing the value on the boundary.

Rigid wall boundaries are defined in such a way as to coincide with cell boundaries. For interior normal velocity calculations, zero normal values on the rigid wall are assumed. Interior tangential (to the wall) velocity calculations use the fictitious values which are placed in the surrounding layer of complimentary cells. Specification of these is after each time-step and after each sweep of the domain during the pressure correction iteration. The tangential (to the wall) velocity component has a vanishing gradient across a non-slip boundary. This is achieved by setting the external values of the velocity equal to the negative of their immediate associated interior values. The free-slip boundary is met by setting the external tangential velocity value equal to their immediate associated interior values.

Specifications of normal velocities at an outflow boundary often possess a problem, and it can have a detrimental upstream influence. One might merely impose the normal gradient of continuative condition and set these values to their immediate upstream values. When primary interest is being focused on the final steady-state, a constant value may be added to each such extrapolated value. This will result in a more rapid convergence. The constant value is chosen so as to make the total outlet flux equal to the total inlet flux, thus satisfying the continuity. Outlet boundary specification is imposed, only each time-step and not after each pass through the mesh during the pressure iteration.

On the axis of symmetry, the usual zero normal velocity and free-

slip axial velocity specifications are applicable while the swirl velocity is given a definite zero value via no-slip condition.

5.4 Stability Considerations

Numerical solution of the partial differential equations is not always successful. Often the solution is dominated by a monotonic or oscillatory error growth, and the final solution in no way resembles the solution expected from the partial differential equations. To avoid this difficulty, stability considerations and appropriate restrictions have to be applied [42]. Since a non-linear theoretical stability analysis is non-existent, simple heuristic methods with numerical experimentation were found to give very reasonable stability criteria [ ].

Having chosen the grid size, the time increment must be restricted in three ways, and a suitable amount of upstream differencing must be effected.

(i) Since the finite difference equations assume fluxes only between neighbouring cells.

$$\Delta t < \min \left(\left| \frac{\Delta r}{V_r} \right| , \left| \frac{\Delta z}{V_z} \right| \right)$$

(ii) When the kinematic viscosity is non-zero, momentum must not diffuse more than approximately one cell in one time-step for which a linear analysis shows

$$\Delta t < \frac{1}{2\nu} \left(\frac{\Delta r^2 \, \Delta z^2}{\Delta r^2 + \Delta z^2} \right)$$

(iii) When the time-step is so restricted, the required amount of upstream (donor cell) differencing must be achieved by choosing a value

slightly greater than (typically 1.2 to 1.5 times) the larger of the right-hand side members of

$$1 > \alpha > \max\left(\left|\frac{V_r \Delta t}{\Delta r}\right|, \left|\frac{V_z \Delta t}{\Delta z}\right|\right)$$

where the maximum is taken over all cells. If α is chosen to be too large, stability is being achieved at the introduction of an unnecessarily large amount of diffusion, like truncation errors known as numerical smoothing.

5.5 Computation Procedure

The finite difference equations along with the boundary and initial conditions constitute the necessary elements in synthesizing an algorithm which gives solutions to the given problems. The computational procedure consists of the following steps:

(i) Set initial conditions, read necessary constants.

(ii) Update the velocity.

(iii) Set boundary conditions.

(iv) Correct the pressure and velocities in order to satisfy cell continuity.

(v) March time one time-step and return to step (ii). Repeat the process until steady-state is achieved.

The pressure iteration procedure continues until the divergence of all computational cells is less than ε.

5.6 Results and Discussions on Approximate Velocity Mapping

Predictions were made for the Concordia's cyclone chamber with the plug covering the vortex core. The specifications for the numerical

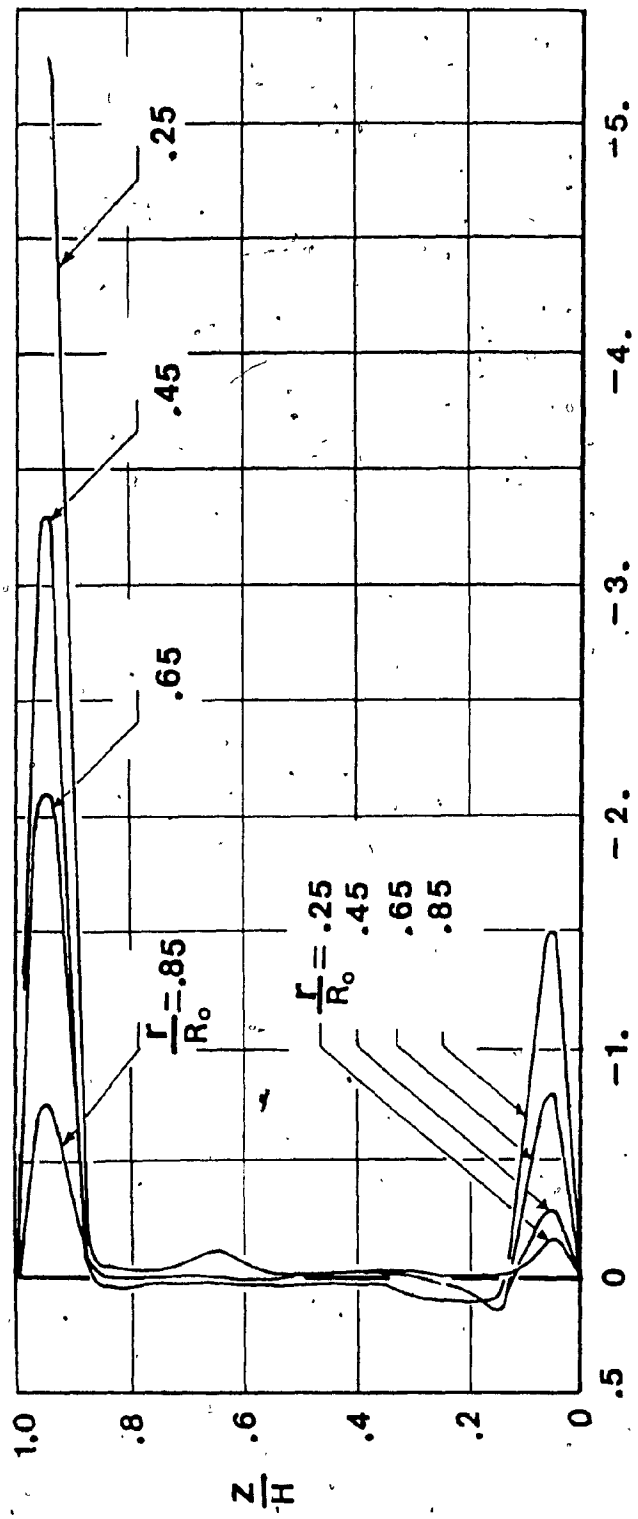

Fig. 5.6.1: Axial Distributions of the Radial Velocity in Different Radial Stations.

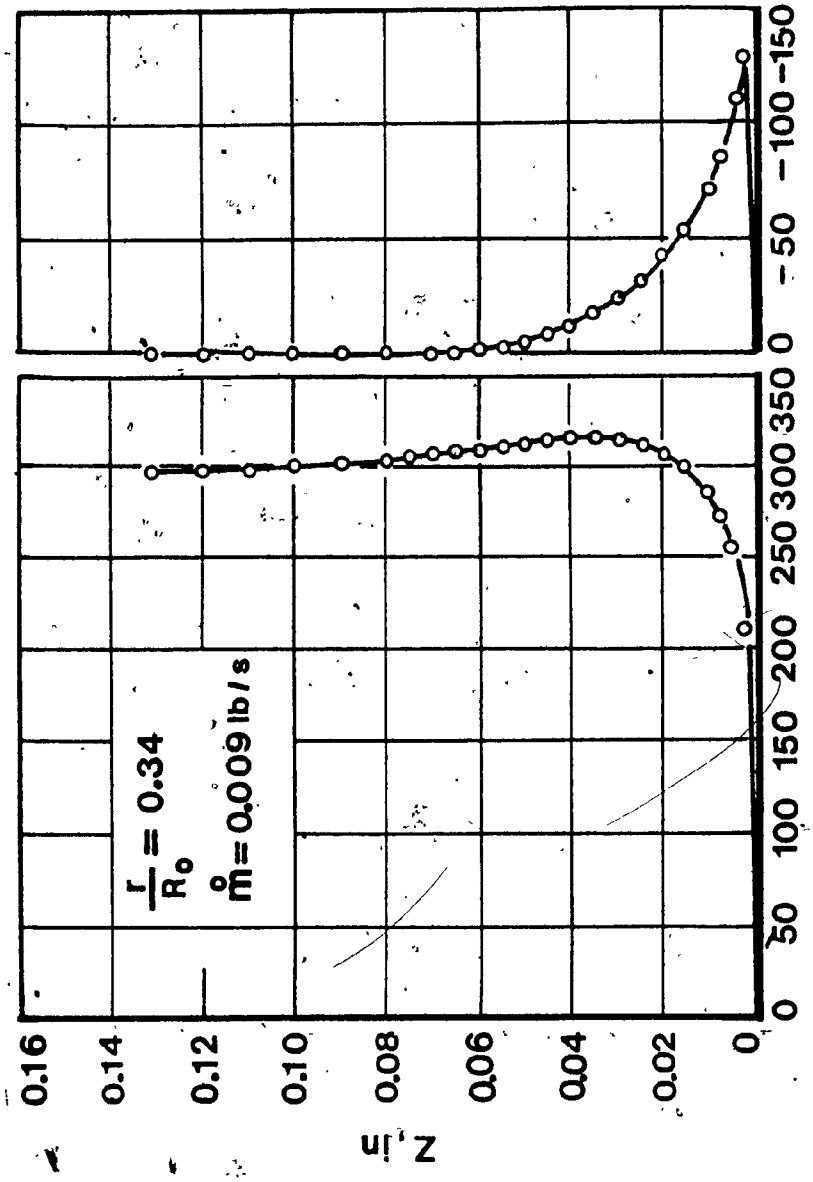

Fig. 5.6.2: Typical Experimental Axial Distributions of the Tangential and Radial Velocities [79].

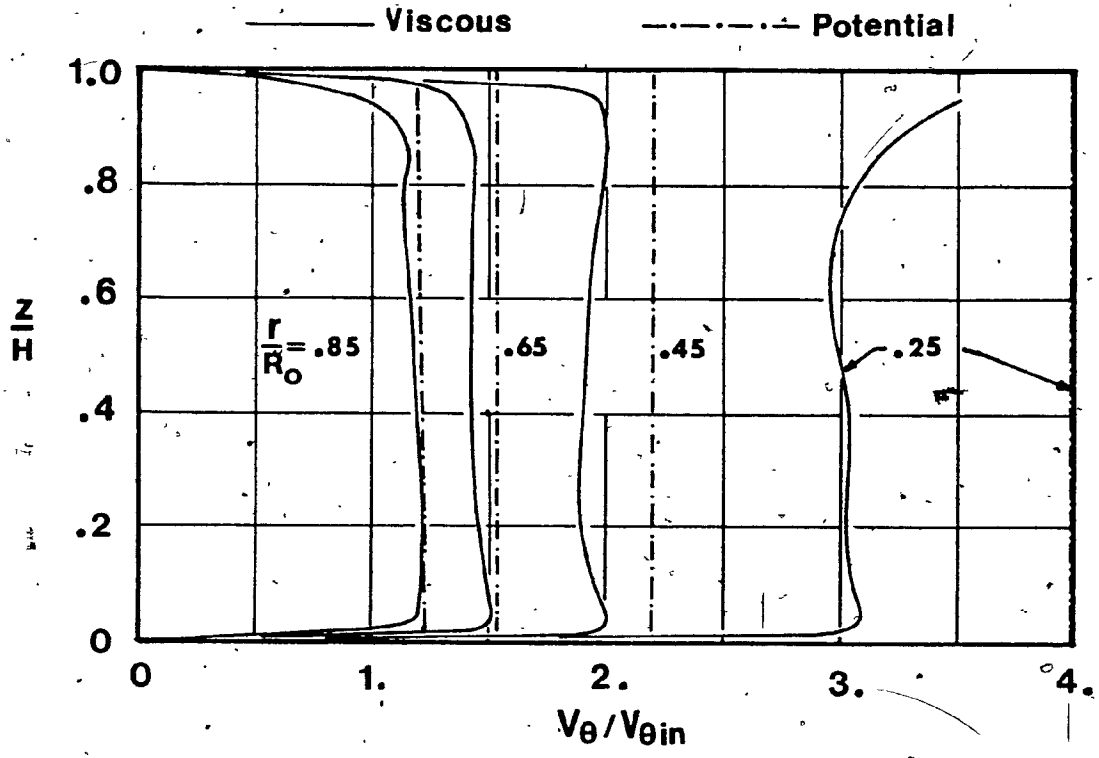

Fig. 5.6.3: Axial Distributions of the Tangential Velocity in Different Axial Stations.

problem are given in Table 5.6.1. The flowfield was marched 1500 time frames which corresponds to approximately twice the fluid transient time. The solution was obtained utilizing a CDC Cyber 174 computer and required computational time in the neighbourhood of 900 CP seconds.

In vortex chambers with small aspect ratios ($H/2R_o$), it is not surprising to find the narrow vortex flowfield dominated by the end plate boundary layers. However, the numerical simulations depicted in Fig. (5.6.1) show that even a large aspect ratio chambers, like the present ($H/2R_o = 1.5$), are also dominated by the end plate effects. It can be seen that most of the mass flow passes through by way of the two boundary layers. Indeed, experiments performed by Kendal [79], have shown that this phenomenon is also present, see Fig. (5.6.2), even in large aspect ratio ($H/2R_o = 1.0$) vortex chambers. Another important feature of the flowfield evident from Kendals [79] experimental results are the two tangential velocity peaks near the top and bottom plates. The latter experimental observation also appears in the numerical results presented in Fig. (5.6.3).

Most often numerical solutions like experiments do not give explanations as to why a specific phenomenon exists but they rather reveal its presence. An attempt will be made here to qualitatively explain the source of origin of the two tangential velocity peaks.

The theoretical work of Koval and Michailov [80] has shown that the radial distribution of the tangential velocity for a viscous swirling fluid, depends on the average radial velocity. This influence of the tangential velocity, is depicted in Fig. (5.6.4) where the radial distributions of the fluids circulation and velocity are given as a function of

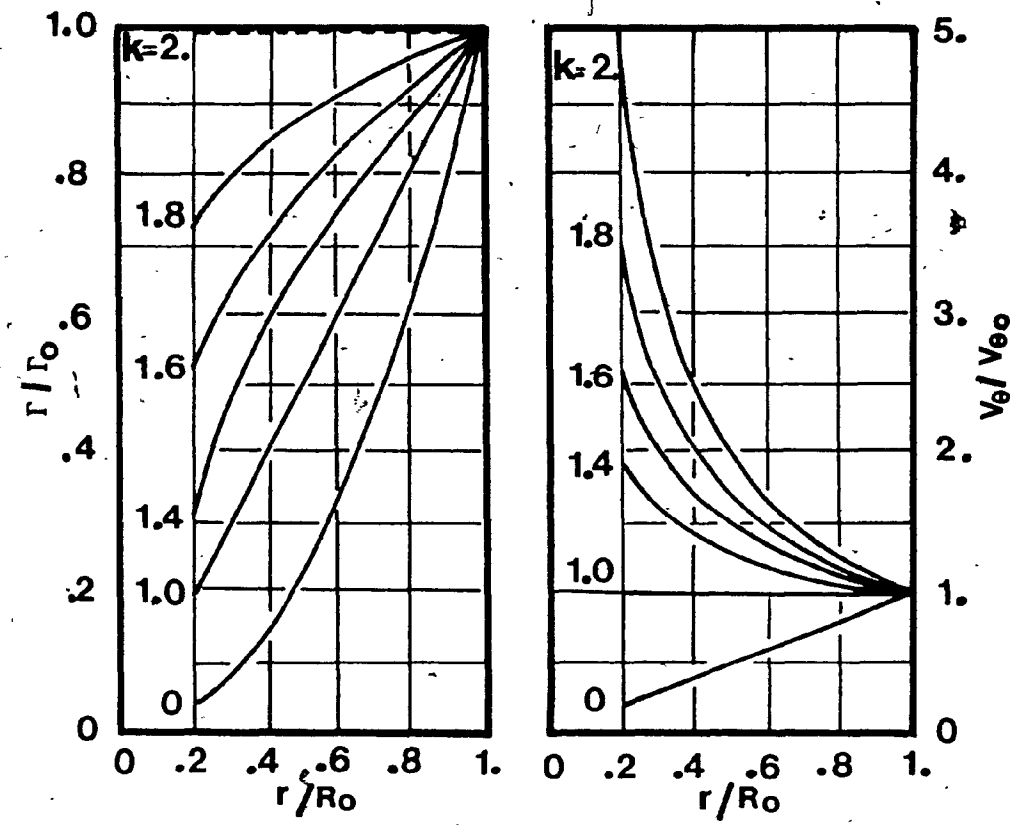

Fig. 5.6.4: Circulation and Tangential Velocity vs. the Radius for Different Values of Parameter k. [80]

parameter $k = \dot{m}_{local}/2\pi d\nu = \bar{V}_r r$. Since $\bar{V}_r$ of the main flow (m.f) is much smaller than $\bar{V}_r$ within the end plate boundary layers (b.ℓ), then

$$k_{(b.\ell)} > k(m.f)$$

Therefore, due to the large average radial velocity inside the boundary layers, a fluid particle is possible to better conserve its circulation Γ, than that moving in the main flow, and thus produces those two peculiar tangential velocity peaks.

The radial distributions of the tangential velocity for different axial stations are shown in Fig. (5.6.5). It is evident, as was also the case in the experimental results for the flow without the plug, that the velocity resembles the Rankine's (free-forced) vortex, and furthermore, the velocity does not vary significantly along the axial direction.

The two axial velocity peaks with the region of axial velocity depression nearly midway to the radius, first encountered in Chapter 4, are also present in Figs. (5.6.6) to (5.6.9). The potential flow solution*, represented in the same figures with dashed lines, indicates an almost constant axial velocity along the radius, with the exception in the vicinity of the outlet, where a peak is developed, as the fluid senses the exit port.

All the previous results were obtained assuming non-slip conditions for the velocities on the solid walls. With free-slip condition of the tangential velocity on the circumferential wall of the chamber, completely different axial velocity profiles were obtained. As it can be seen from Fig. (5.6.10), the annular reverse flow region is moved near the

*See Appendix E for details.

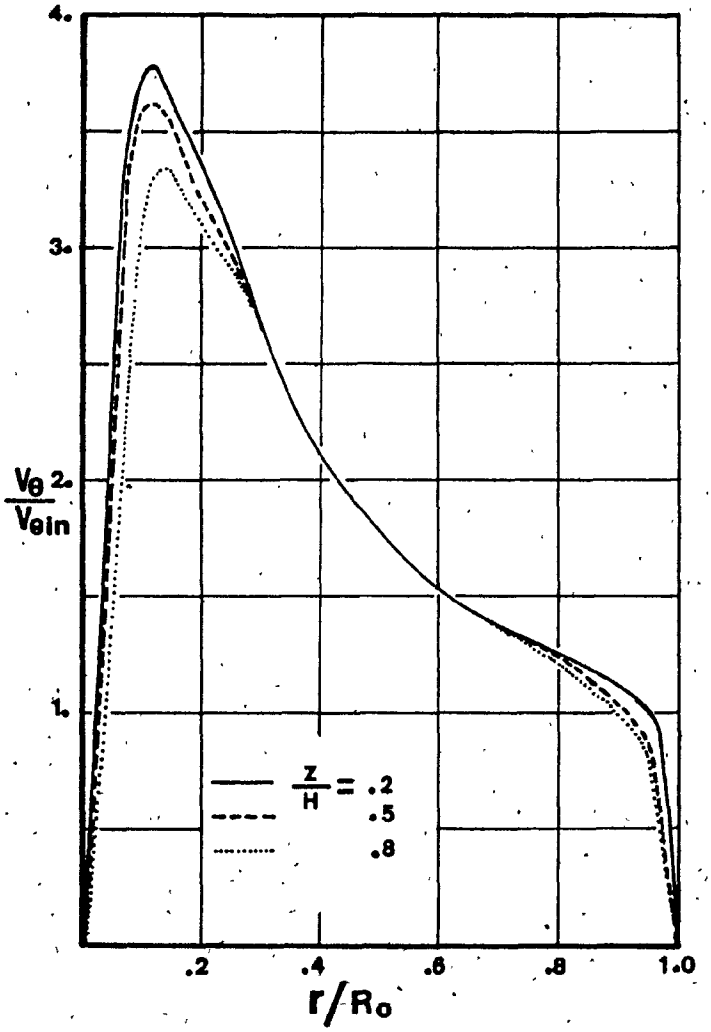

Fig. 5.6.5: Radial Distribution of the Tangential Velocity in Different Axial Stations.

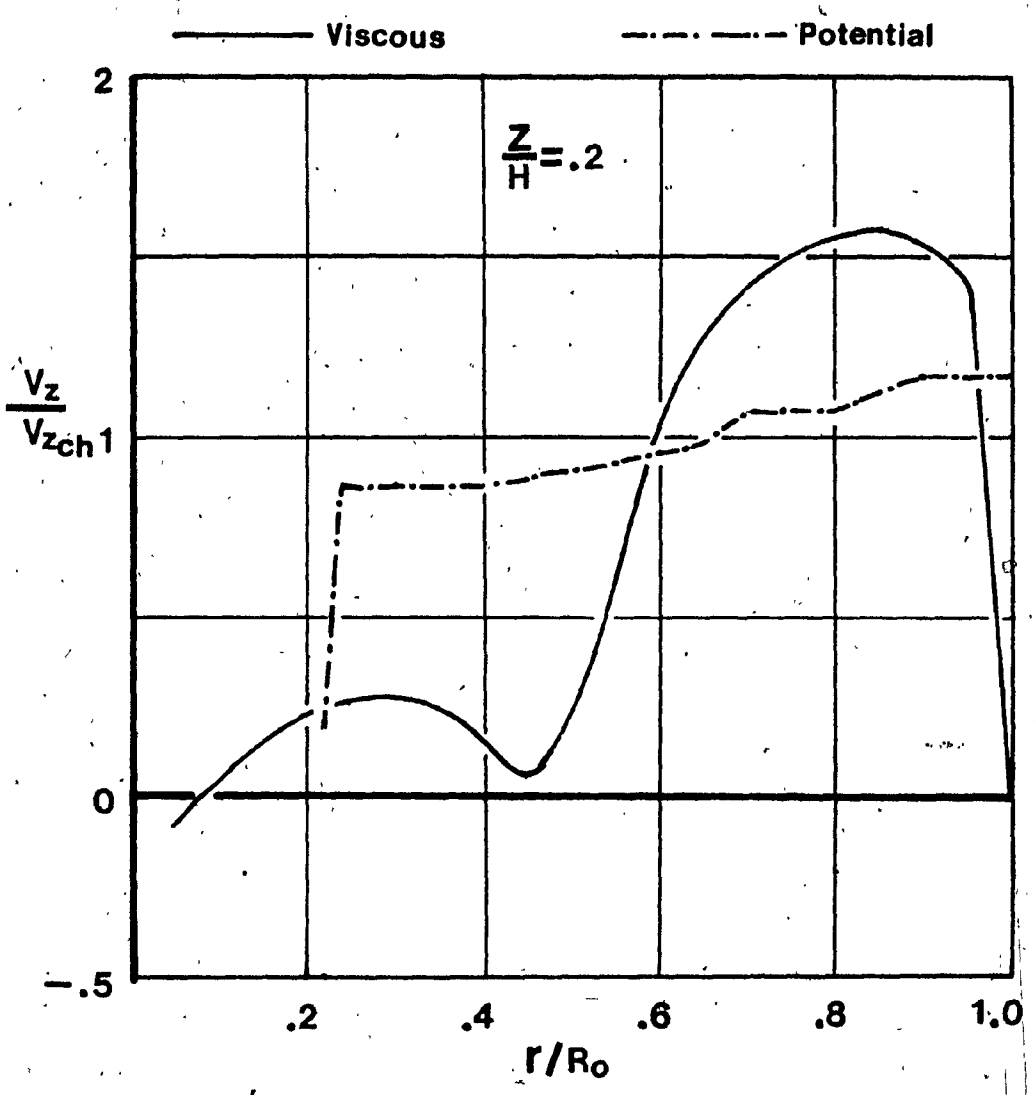

Fig. 5.6.6: Axial Velocity vs. the Radius for z/H = 0.2.

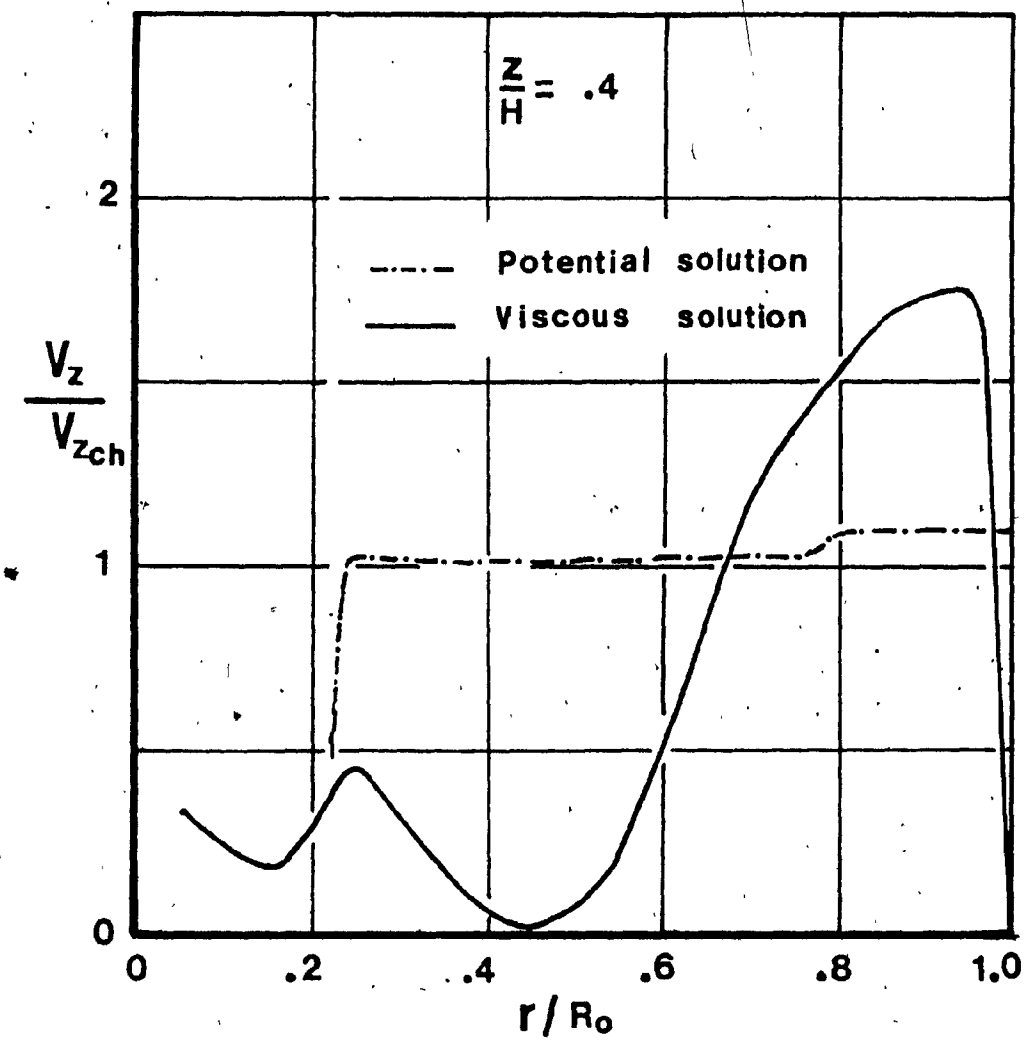

Fig. 5.6.7: Axial Velocity vs. the Radius for z/H = 0.4.

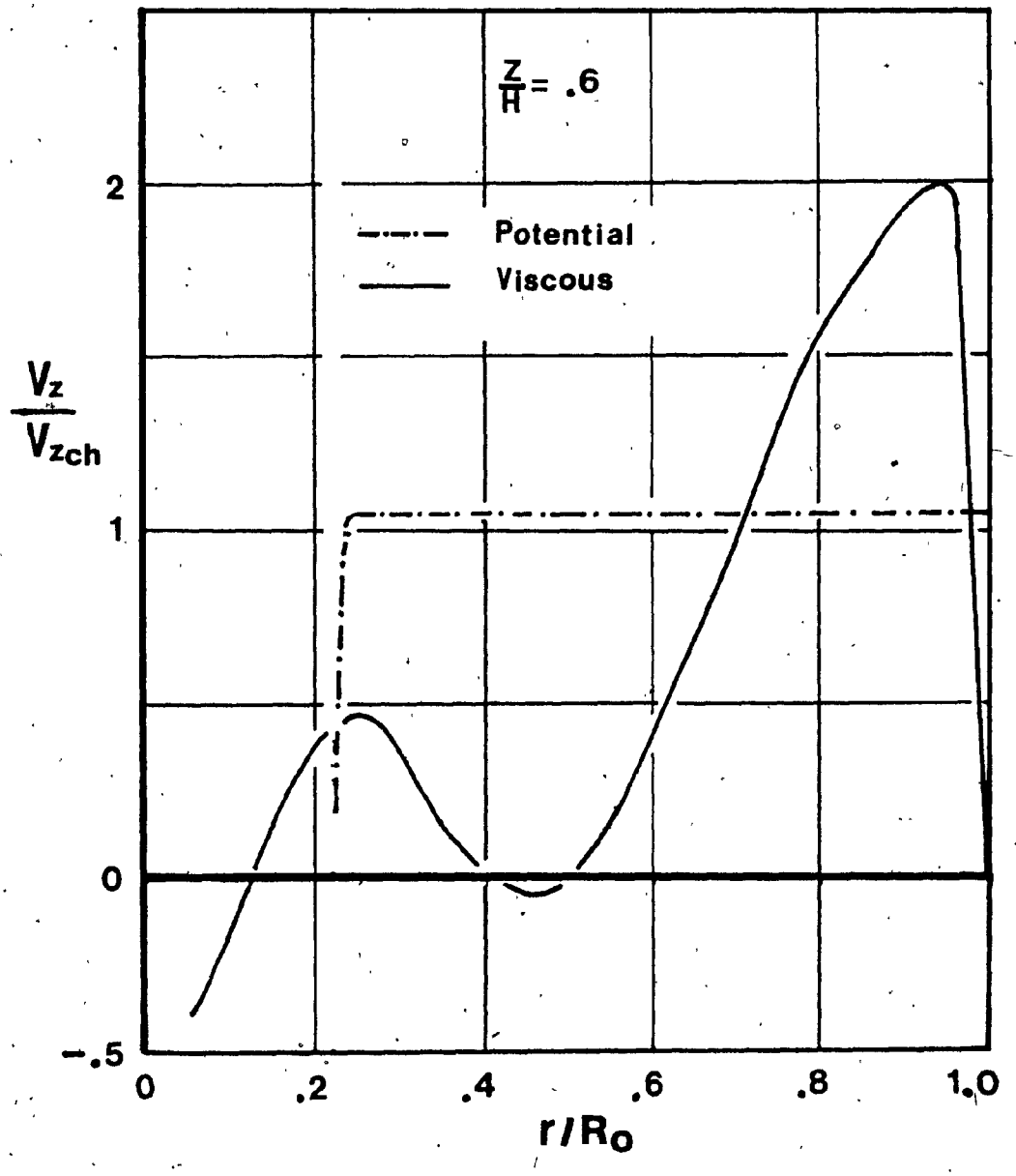

Fig. 5.6.8: Axial Velocity vs. the Radius for z/H = 0.6.

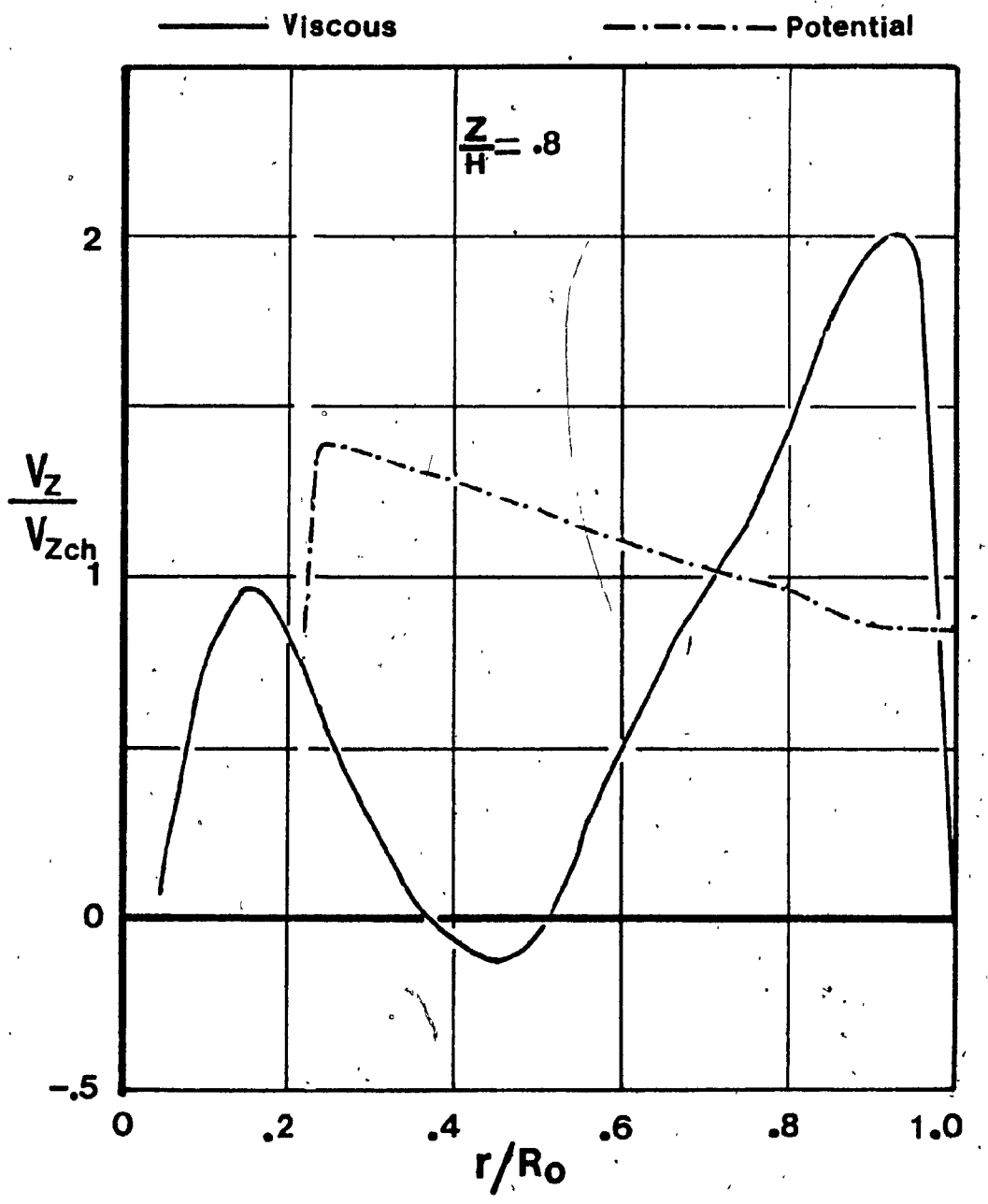

Fig. 5.6.9: Axial Velocity vs. the Radius for z/H = 0.8.

circumferential wall, and most of the fluid finds the exit via an area close to the axis of rotation. Therefore, numerical evidence suggests that, the non-slip condition of the tangential velocity on the circumferential wall, encourages the main fluid mass to exit the chamber through the top plate, and is responsible for the annular recirculatory flow area midway on the radius of the vortex chamber.

TABLE 5.6.1: Specifications for the Numerical Problem

Parameter	Value
$H/2R_o$	1.5
$\Delta r, \Delta z, \Delta t$	0.015, 0.046, 0.0025 [m,m,sec] (respectively)
h_{in}	0.046 m
imax, jmax, IOUT, IP	12, 12, 4, 2
ν_{eff}*	1.02×10^{-4} m^2/s
Q	0.023 m^3/s
$V_{\theta in}$	6.16 m/s

*Effective viscosity comparable to that of silicon oil (1.35×10^{-4} m^2/s).

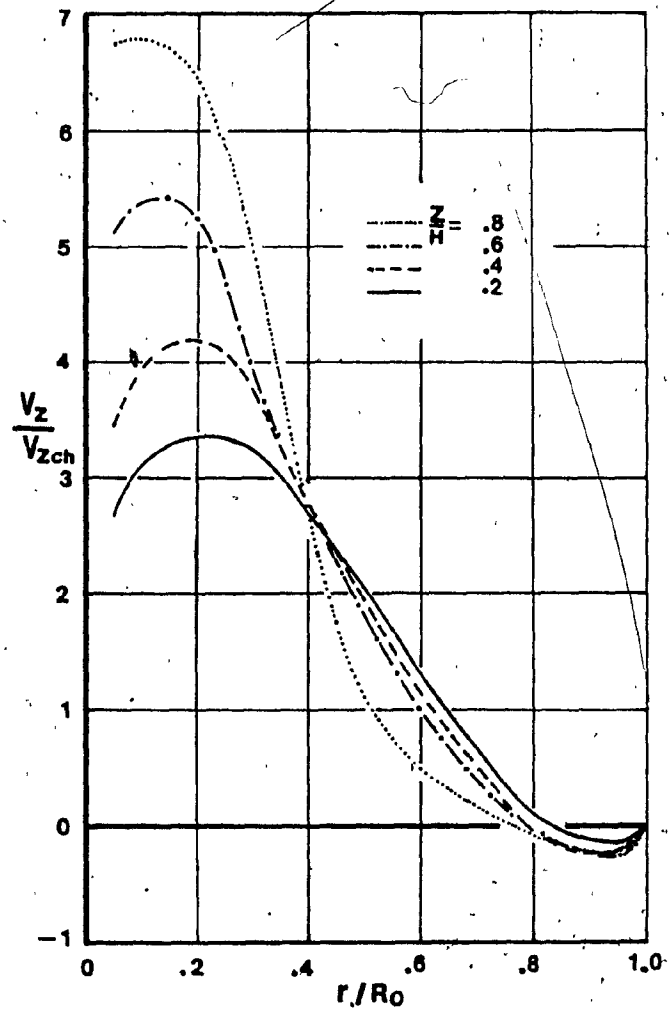

Fig. 5.6.10: Axial Velocity vs. the Radius with Free-Slip on the Circumferential Wall.

CHAPTER 6

CONCLUSIONS

CHAPTER 6

CONCLUSIONS

Theoretical and experimental work on confined vortex flows were presented. It was shown that simple vortex to evolve, need energy to be externally provided. Based on variational principles, extrema were shown to exist in this case followed by the Helmholtz minimum viscous dissipation condition for the steady-state. The latter was achieved through the necessary condition (Euler-Lagrange equation) and the sufficient condition (second variation of viscous dissipation integral). Based on these theoretical considerations, it became apparent that the solid body rotation, for the fluid motion resembling the Rankine's vortex, is essential for minimum viscous dissipation in the field. The required energy that must be supplied externally to the fluid, for a forced vortex to evolve, was analytically obtained via the integral energy equation. Next, it was shown that viscous dissipation is absent in those flowfields were under a permissible coordinate transformation they become hydrostatic fields. The two potential vortex motions, i.e. viscous potential and inviscid potential vortices, were shown to exist under different flow conditions. Exact solutions for the confined Rankine's vortex decay were also presented.

An analytical model to study selected fluid parameters in vortex chambers was developed. It was shown that the dimensionless quantities (a) core size, (b) static pressure drop across the chamber, (c) radial static pressure distribution and (d) radius of the reverse flow at the exit, were shown to be functions of the chamber geometry only. The derived equations provide the means for flow parameters of practical

importance, like the aerodynamic resistance of the chamber, to be accurately calculated. In addition, it was experimentally shown, that the pressure drop across the chamber, can be effectively minimized, using a solid cone to prevent the reverse flow at the exit.

Next, a numerical solution to the viscous equations for the flow in a vortex chamber was presented. The numerical method utilized the forward time centered space finite differences formulation, with the attention focused toward the steady-state flowfield condition. Predictions have shown the main flow to be dominated by the end plate boundary layers. The Rankine's velocity profile for the tangential component and the reverse flow region midway the radius of the chamber were also present. Furthermore, the numerical simulations indicated that the non-slip condition of the velocity on the circumferential wall, encourages the main fluid mass to exit the chamber through an area close to the top plate and is responsible for the annular recirculatory flow region taking place midway on the radius of the vortex chamber.

The presented analytical results and experimental evidence for the chamber flows compare well with each other as well as with that appearing in the literature. The difference between viscous flowfield potential flow solutions were outlined. Finally, the numerical results were found to be in qualitative agreement with previously known experimental findings.

REFERENCES

REFERENCES

1. Küchemann, D., "Report on the I.U.T.A.M. Symposium on Concentrated Vortex Motions in Fluids", J. Fluid Mech., Vol. 21, Part 1, 1965, pp. 1-20.

2. Aristotle, "Physical Treatises", Book 3 on Metereologica, Translated by Webster, E.W., in "Great Books of the Western World", Vol. 8, Encyclopedia Britanica, Inc., 23rd Printing, 1980, pp. 475 and 476.

3. Hoerner, S.F., "Fluid-Dynamic Drag", Published by the author, 1965. Also, "Del Moto e Misura Dell'Acqua", edited by Carusia and Favaro, Bologna, 1923.

4. Robertson, J.M., "Hydrodynamics in Theory and Application", Prentice-Hall, Inc., Englewood Cliffs, N.J., 1965.

5. Zemansky, N.W., "Heat and Thermodynamics", McGraw-Hill Inc., fifth edition, New York, 1968.

6. Samaras, D.G., "Theory of Ion Flow Dynamics", Dover Publications Inc., New York, 1971.

7. Simiu, E. and Scanlan, R.H., "Wind Effects on Structures: An Introduction to Wing Engineering", John Wiley and Sons, New York, 1978.

8. Gupta, A.K., Lilley, D.G. and Syred, N., "Swirl Flows", Abacus Press, Energy and Engineering Series, Tunbridge Wells, U.K., 1984.

9. Lay, J.E., "An Experimental and Analytical Study of Vortex-Flow Temperature Separation by Superposition of Spiral and Axial Flows, Part 1 and 2", Trans. ASME/Journal of Heat Transfer, 1959, pp. 202-221.

10. Stephan, K., Lin, S., Durst, M., Huang, F. and Seher, D., "An Investigation of Energy Separation in a Vortex Tube", Int. J. Heat Mass Transfer, Vol. 26, No. 3, 1983, pp. 341-348.

11. Ranque, G.J., "Method and Apparatus for Obtaining From a Fluid Under Pressure Two Currents of Fluids at Different Temperatures", U.S. Patent Office No. 1,952,281, 1934.

12. Ragsdale, R.G., "NASA Research on the Hydrodynamics of the Gaseous Vortex Reactor", NASA TN D-288, 1960.

13. McLafferty, G.H. and Bauer, H.E., "Studies of Specific Nuclear Light Bulb and Open-Cycle Vortex-Stabilized Gaseous Nuclear Rocket", NASA CR-1030, 1968.

14. Taplin, L.B. and McFall, R.H., "Vortex Amplifiers and Circuits", Bendix Technical Journal, Vol. 1, No. 4, Winter, 1969.

15. Lilley, D.G., "Fluid Dynamic Combustor Research Problems", Paper Presented for discussion at DOD Colloquium on Gas Turbine Combustor Modelling, held at Purdue University, West Lafayette, Indiana, September 5 and 6, 1979.

16. Lefebre, A.H., Ibtahim, A.R.A.F. and Benson, N.C., "Factors Affecting Fresh Mixture Entrainment in Bluff-Body Stabilized Flames", Combustion and Flame, Vol. 10, 1966, pp. 231-239.

17. Syred, N. and Beer, J.M., "Combustion in Swirling Flows: A Review", Combustion and Flame, Vol. 23, 1974, pp. 143-201.

18. Krepec, T. and Kwok, C.K., "Problems Encountered in the Development of a Double Cyclone Furnace", 16-th South-Eastern Seminar on Thermal Sciences in 1982 in Miami, Florida, U.S.A.

19. Krepec, T. and Kwok, C.K., "Preliminary Investigations of a Double Vortex Combustion Chamber", 1981 Fall Meeting of Combustion Institute, Eastern Section, Pittsburgh, U.S.A.

20. Georgantas, A., Krepec, T. and Kwok, C.K., "Flow Pattern Investigations in a Model of a Double Vortex Combustion Chamber", Presented in 1982 Spring Technical Meeting of Combustion Institute, Canadian Section, Banff, Alberta.

21. Georgantas, A., Krepec, T., and Kwok, C.K., "Investigation of Double Vortex Structure and its Ability to Retain Fuel Particles in a Cyclone Combustion Chamber", Presented in 1983 Fall Technical Meeting of the Combustion Institute, Eastern Section, Providence, Rhode Island.

22. Odgers, J. and Kretschmer, D., "The Effects of Fuel Properties on Atomisation and Evaporation", Paper Presented at the Fourth Symposium on Gas Turbine Operations and Maintenance, Sponsered by NRC, Toronto, Ontario, Canada, September 21 and 22, 1981.

23. Baluev, E.D. and Troyankin, Y.V., "Study of the Aerodynamic Structure of Gas Flow in a Cyclone", Thermal Engineering, Vol. 14, 1967, pp. 84-87.

24. Vatistas, G.H., Lin, S. and Kwok, C.K., "An Analytical and Experimental Study on the Core-Size and Pressure Drop Across a Vortex Chamber", AIAA 17th Fluid Dynamics Plasma Dynamics and Plasma Dynamics Conference, Snowmass, Colorado, June 25-27, 1984.

25. Lewellen, W.S. "A Review of Confined Vortex Flows", NASA Contractor Report (NASA CR-1772), July, 1971.

26. Binnie, A.M. and Hookings, G.A., "Laboratory Experiments on Whirlpools", Proceedings of the Royal Society, Series A, Vol. 205, 1951, p. 530.

27. Shakespeare, W.J. and Levy, E.K., "Pressure Drop in a Confined Vortex with High Flow Rate", Paper Presented at the Winter Annual Meeting of ASME, Chicago, Illinois, November 1980.

28. Savino, J.M., and Keshock, E.G., "Experimental Profiles of Velocity Components and Radial Pressure Distributions in a Vortex Contained in a Short Cylinder Chamber", NASA TN D-3072, October 1965.

29. Kwok, C.K., "Vortex Flow in a Thin Cylindrical Chamber and Its Application in Fluid Amplifier Technology", Ph.D. Thesis, McGill University, Montreal, 1966.

30. Syred, N., Dahmen, K.R., Styles, A.C. and Najim, S.E., "A Review of Combustion Problems Associated with Low Calorific Value Fuels", Journal of the Institute of Fuel, Vol. 1, No. 405, December 1977, pp. 195-207.

31. Kalishevkii, L.L. and Ganchev, B.G., "A Study of Combustion in a Horizontal Cyclone Furance", Thermal Engineering, Vol. 12, 1965, p. 96.

32. Troyankin, Y.U. and Baleuv, E.D., "The Aerodynamic Resistance and Efficiency of a Cyclone Chamber", Thermal Engineering, Vol. 16, 1969, p. 29.

33. Ustimenko, B.P. and Buchman, M.A., "Turbulent Flow Structure in a Cyclone Chamber", Thermal Engineering, Vol. 15, 1968, p. 64.

34. Styles, A.C., Syred, N. and Najim, S.E., "Turbulent Flow Structures and Recirculation Patterns Associated with Cyclone Combustors and Their Effect on Flame Stabilization", Proceedings of the Symposium on Turbulent Shear Flows, April 1977, p. 725.

35. Styles, A.C., Syred, N. and Najim, S.E., A Study of Modulable Cyclone Combustors Using Gaseous Fuels", Journal of the Institute of Fuel, December 1979, pp. 159-168.

36. Najim, S.E., Styles, A.C. and Syred, N., "Stabilization of Low Calorific Value Gases in a Cyclone Combustor", AIAA Journal of Energy, Vol. 5, No. 1, January-February, 1981, pp. 43-50.

37. Vogelpohl, G., "Die Strömung der Wirbelquelle zwischen ebenen Wänden mit Berücksichtigung der Wandreibung", ZAMM, 24, 289, 1944.

38. Ostrach, S. and Loper, D.E., "An Analysis of Confined Vortex Flows". 3rd Aerospace Sciences Meeting, AIAA Paper No. 66-88, New York, January 24-26, 1966.

39. Wormley, D.N., "An Analytical Model for the Incompressible Flow in Short Vortex Chamber", Trans. ASME, J. of Basic Engineering, Paper No. 68-WA/FE-17, 1968.

40. Kwok, C.K., Thin, N.D. and Lin, S., "An Investigation of Confined Vortex Flow Phenomena", Trans. J. of Basic Engineering, ASME, September 1972, pp. 689-696.

41. Lilley, D.G. and Vatistas, G.H., "Flow Prediction in Cyclone Chambers", Report Presented at the Combustion Institute, Canadian Section, Meeting, University of Ottawa, Ottawa, Canada, May 4-5, 1978.

42. Vatistas, G.H., "Computational Flow Prediction in Cyclone Chambers", Master of Engineering Thesis, Concordia University, Mechanical Engineering Department, 1980.

43. Harlow, F.H. and Nakayama, P.I., "Transport of Turbulence Energy Decay Rate", Phys. Fluids, Vol. 10, 1967, p. 2323.

44. Jones, W.P. and Launder, B.E., "The Prediction of Laminarization with a Two-Equation Model of Turbulence", Int. J. Heat Mass Transfer, Vol. 15, 1972, pp. 301-314.

45. Gosman, A.D. and Pun, W.M., Lecture Notes for Course Entitled, "Calculation of Recirculating Flows", Report HTS/74/2, Department of Mechanical Engineering, Imperial College, London, 1974.

46. Gibson, M.M., "An Algebraic Stress and Heat-Flux Model Turbulent Shear Flow with Streamline Curvature", Int. Journal of Heat and Mass Transfer, Vol. 21, 1978, pp. 1609-1617.

47. Launder, B.E., Priddin, C.H. and Sharma, B.I., "The Calculation of Turbulence Boundary Layers on Spinning and Curved Surfaces", ASME Trans. J. of Fluids Engineering, Vol. 99, March 1977, pp. 231-238.

48. Helmholtz, "Zur Theorie der Stationären Ströme in Reibenden Flüssigkeiten", Verh. Naturhist, Med. Ver. Heidelberg, Vol. V, October 1869.

49. Reileigh, Lord, "Scientific Papers", Vol. 6, Dover Publications, 1964.

50. Zierep, J., "Viscous Potential Vortex", Archives of Mechanics (Archivinum Mechaniki Stosowanej), 36, 1, 1984.

51. Chandrashekhar, S., "Hydrodynamic and Hydromagnetic Stability", Oxford Press, 1969, pp. 273-381.

52. Yuan, S.N., "Fundamentals of Fluid Mechanics", Prentice-Hall Inc., Englewood Cliffs, N.J., 1967.

53. Lamb, H., "Hydrodynamics", Cambridge University Press, Sixth edition, Cambridge, 1945.

54. Weinstock, R., "Calculus of Variations with Applications to Physics and Engineering", Dover Publications, 1974.

55. Davis, H.T., "Introduction to Nonlinear Differential Equations", Dover Publications, 1962.

56. Batchelor, G.K.,"An Introduction to Fluid Dynamics", Cambridge University Press, 1970.

57. Rayleigh, Lord, "The Theory of Sound", Vol. 1, Dover Publications, 1945.

58. Kreyszig, E., "Advanced Engineering Mathematics", Third Edition, John Wiley and Sons, Inc., New York, 1972.

59. Prandtl and Tietjens, "Fundamentals of Hydro- and Aeromechanics", Dover Publications, Inc., New York, 1934.

60. Doebelin, E.O., "Measurement Systems", McGraw-Hill, Inc., New York, 1975.

61. Georgantas, A.I., "Experimental Investigation Confined Vortex Flow in a Cylindrical Chamber of Aspect Ratio 1.5", M.Eng. Thesis, Concordia University., Montreal, Canada, November 1983.

62. Head, V.P. and Hatboro, P.A., "Coefficient of Float-Type Variable Area Flowmeters", Trans. ASME, August 1954, pp. 851-862.

63. Rhode, D.L., Lilley, D.G. and MacLaughlin, D.K., "mean Flowfields in Axisymmetric Combustor Geometries with Swirl", (AIAA 82-0177), Paper Presented at the AIAA 20th Aerospace Science Meeting, Orlando, Florida, January 1982.

64. Folsom, R.G., "Review of the Pitot Tube", Trans. ASME, October 1956, p. 1450.

65. Gupta, A.K. and Lilley, D.G., "Flowfield Modeling and Diagnostics", Abacus Press, Tunbridge Wells, Keng, England, 1982.

66. Reydon, R.F. and Gauvin, W.H., "Theoretical and Experimental Studies of Confined Vortex Flows", The Canadian Journal of Chemical Engineering, Vo.. 59, February 1981, pp. 14-23.

67. Ogawa, A., "Estimation of the Collection Efficiencies of the Three Types of the Cyclone Dust Collectors from the Standpoint of the Flow Pattern in the Cylindrical Cyclone Dust Collectors", JSME, Vol. 27, No. 223, January 1984, pp. 64-69.

68. Tager, S.A., "Calculating the Aerodynamic Resistance of Cyclone Combustion Chambers", Teploenergetika, Vol. 7, 1971, pp. 88-91.

69. Troyankin, Y.V. and Baluev, E.D., "The Aerodynamic Resistance and Efficiency of a Cyclone Chamber", Teploenergetika, Vol. 16, 1969, pp. 29-32.

70. Styles, A.C., Syred, N. and Najim, S., "A Study of a Modulable Cyclone Combustor using Gaseous Fuel", Paper presented at the Spring Meeting of the Central Section of the Combustion Institute, NASA Lewis Research Center, March 1977.

71. Taylor, G.I., "Stability of a Viscous Liquid Contained Between Two Rotating Cylinders", Phil, Trans. Roy. Soc. London, A223, 1923, pp. 289-343.

72. Goertler, H., "On the Three-Dimensional Instability of Laminar Boundary Layers on Concave Walls", NACA-TM-1375, June 1954.. Translated version of "Uber dreidimensionale Instabilität laminarer Grenzschichten an Konkaven Wänden. Nachr. Wiss. Ges. Gottingen, Math. Phys. Klasse, Neue Folge 2, No. 1, 1940.

73. Synge, J.L., "The Stability of Heterogeneous Liquids", Trans. Roy. Soc. of Canada, Vol. 27, 1933, pp. 1-18.

74. Hirt, C.W., Nichols, B.D. and Romero, N.C., "SOLA: A Numerical Solution Algorithm for Transient Fluid Flows", Report LA-5882, Los Alamos Scientific Laboratory and the University of California, Los Alamos, N.M., 1975.

75. Harlow, F.H., "The Particle in Cell Computing Method for Fluid Dynamics", Methods in Computational Physics, Academic Press, Vol. 3, 1964, pp. 319-343.

76. Vatistas, G.H., Lin, S., Kwok, C.K. and Lilley, D.G., "Bluff-Body Flameholder Wakes: A Simple Numerical Method", Paper AIAA-82-1177, Presented at AIAA/ASME/SAE 18th Joint Propulsion Conference, Cleveland, Ohio, U.S.A., June 1982.

77. Kwok, C.K. and Vatistas, G.H., "A Computer Study of Multi-Stable Cyclone Furnace Aerodynamics", Paper Presented in ASME International Computer Technology Conference, San Francisco, Calif., U.S.A., 1980.

78. Lilley, D.G. and Vatistas, G.H., "Fundamental Concepts for Fully Three-Dimensional Chemically Reacting Flowfield Predictions", ASME Computer Technology Conference, Minneapolis, Minn., U.S.A., September 27-30, 1981.

79. Kendall, J.M., "Experimental Study of a Compressible Viscous Vortex", JPL Tech. Report No. 32-290, June 1962.

80. Koval, V.P. and Michailov, S.L., "Velocity and Pressure Distribution of Liquid in a Swirl Chamber", Teploenergetika, Vol. 19, 1972, p. 25.

APPENDIX A

APPENDIX A

A.1 The Second Variation of an Integral

Consider the integral,

$$I = \int_{R_1}^{R_2} f(r, V_\theta, V_\theta') \, dr \tag{A.1}$$

Let $\eta(r)$ be a function with continuous second derivatives which vanish at $r = R_1$ and $r = R_2$. If ϵ is a small parameter, then,

$$V_\theta(r,\epsilon) = V_\theta(r) + \epsilon\eta(r) \tag{A.2}$$

represents a family of curves which pass through the end points (r_1, V_{θ_1}) and (r_2, V_{θ_2}). First differentiation of eq. (A.2) gives,

$$\frac{\partial}{\partial r} V_\theta(r,\epsilon) = V_\theta'(r) + \epsilon\eta'(r) \tag{A.3}$$

Incorporating eqns. (A.2) and (A.3) into (A.1) one obtains the integral,

$$I(\epsilon) = \int_{R_1}^{R_2} f(r, V_\theta + \epsilon\eta, V_\theta' + \epsilon\eta') \, dr \tag{A.4}$$

The first variation of (A.4) gives,

$$\frac{dI(\epsilon)}{d\epsilon} = \int_{R_1}^{R_2} \left\{ \frac{\partial f}{\partial V_\theta} \eta(r) + \frac{\partial f}{\partial V_\theta'} \eta'(r) \right\} dr \tag{A.5}$$

The second variation is,

$$\frac{d}{d\varepsilon}\left[\frac{dI(\varepsilon)}{d\varepsilon}\right] = \int_{R_1}^{R_2} \frac{d}{d\varepsilon}[G]\, dr \qquad (A.6)$$

where,

$$G = \frac{\partial f}{\partial V_\theta}\, \eta(r) + \frac{\partial f}{\partial V'_\theta}\, \eta'(r)$$

However,

$$\frac{d}{d\varepsilon}[G] = \frac{\partial}{\partial V_\theta}[G]\frac{\partial V_\theta}{\partial \varepsilon} + \frac{\partial}{\partial V'_\theta}[G]\frac{\partial V'_\theta}{\partial \varepsilon} = \frac{\partial^2 f}{\partial V_\theta^2}[\eta(r)]^2$$

$$+ 2\frac{\partial^2 f}{\partial V_\theta \partial V'_\theta}\eta(r)\eta'(r) + \frac{\partial^2 f}{\partial V'^2_\theta}[\eta'(r)]^2 \qquad (A.7)$$

With the aid of eq. (A.7) and (A.6), the second variation of the integral for $\varepsilon \to 0$, is,

$$\left.\frac{d^2 I}{d\varepsilon^2}\right|_{\varepsilon \to 0} = \int_{R_1}^{R_2} \left\{\frac{\partial^2 f}{\partial V_\theta^2}[\eta(r)]^2 + 2\frac{\partial^2 f}{\partial V_\theta \partial V_\theta'}\eta(r)\eta'(r)\right.$$

$$\left. + \frac{\partial^2 f}{\partial V'^2_\theta}[\eta'(r)]^2\right\} dr \qquad (A.8)$$

APPENDIX B

APPENDIX B

B.1 Decay of Rankine's Vortex

(1) Free-Slip at the Wall

Under the transformation,

$$\tilde{V}_\theta(t,r) = V_{\theta o}\left(\frac{r}{R_o}\right) - V_\theta(t,r) \tag{B.1}$$

eq. (2.2.5) transforms to,

$$\frac{\partial \tilde{V}_\theta}{\partial t} = \nu\left(\frac{\partial^2 \tilde{V}_\theta}{\partial r^2} + \frac{1}{r}\frac{\partial \tilde{V}_\theta}{\partial r} - \frac{\tilde{V}_\theta}{r^2}\right) \tag{B.2}$$

The boundary and initial conditions for the problem are,

(i) $\tilde{V}_\theta = 0$ for $r = 0$ and $t \geq 0$

(ii) $\tilde{V}_\theta = 0$ for $r = R_o$ and $t \geq 0$

(iii) $$\tilde{V}_\theta(o,r) = \begin{cases} \left(\frac{V_{\theta o}}{R_o} - \frac{\Gamma}{2\pi R_i^2}\right) r & \text{for } 0 \leq r \leq R_i \\ \left(\frac{V_{\theta o}}{R_o} r - \frac{\Gamma}{2\pi r}\right) & \text{for } R_i \leq r \leq R_o \end{cases}$$

where Γ is the circulation of the vortex filament, $\Gamma = 2\pi V_{\theta_o} R_o$.

(iv) $\lim_{t \to \infty} \tilde{V}_\theta = 0$

Assume,

$$V_\theta(t,r) = T(t)\,R(r) \tag{B.3}$$

Inserting eq. (B.3) into eq. (B.2) yields,

$$\frac{dT}{dt} - \lambda \nu T = 0 \tag{B.4}$$

$$\frac{d^2R}{dr^2} + \frac{1}{r}\frac{dR}{dr} - \left(\lambda + \frac{1}{r^2}\right) R = 0 \tag{B.5}$$

Where λ is the separation constant. Based on physical grounds,

$$\lambda = - m^2$$

Then, from eqs. (B.4) and (B.5) we have respectively,

$$T(t) = A\, e^{-m^2 \nu t} \tag{B.6}$$

and

$$R(r) = B J_1 (mr) + D N (mr) \tag{B.7}$$

Neuman's function is not finite for $r = 0$. This will violate the physical assumption that the velocity is finite in space and time. Therefore, constant D must be forced to zero, or,

$$R(r) = B J_1 (mr) \tag{B.8}$$

Utilization of (ii) and eq. (B.8) yields,

$$J_1(mR_o) = 0 \quad \text{or} \quad m = \frac{\alpha_n}{R_o} \qquad (n = 1,2,3,\ldots)$$

where α_n are the roots of J_1.

From linearity of eq. (B.1) we have,

$$\tilde{V}_\theta(t,r) = \sum_{n=1}^{\infty} A_n J_1 \left(\alpha_n \frac{r}{R_o}\right) e^{-\left(\frac{\alpha_n}{R_o}\right)^2 \nu t} \tag{B.9}$$

Equation (B.9) satisfies all the conditions except (iii). In order to evaluate the coefficients A_n, the initial condition (iii) is used,

$$\tilde{V}_\theta(0,r) = \sum_{n=1}^{\infty} A_n J_1\left(\alpha_n \frac{r}{R_o}\right).$$

$$A_n = \frac{\int_0^{R_o} r\, \tilde{V}_\theta(0,r)\, J_1\left(\alpha_n \frac{r}{R_o}\right) dr}{\int_0^{R_o} r^2 J_1^2\left(\alpha_n \frac{r}{R_o}\right) dr}$$

The denominator when evaluated yields,

$$\int_0^{R_o} r^2 J_1^2\left(\alpha_n \frac{r}{R_o}\right) dr = \frac{R_o^2}{2} J_o^2(\alpha_n)$$

The nominator requires extra care. Let,

$$\int_0^{R_o} r\, \tilde{V}_\theta(0,r)\, J_1\left(\alpha_n \frac{r}{R_o}\right) dr = B_1 + B_2 + B_3$$

where

$$B_1 = \left[\frac{V_{\theta o}}{R_o} - \frac{\Gamma}{2\pi R_i^2}\right] \int_0^{R_i} r^2 J_1\left(\alpha_n \frac{r}{R_o}\right) dr$$

$$= \left[\frac{V_{\theta o}}{R_o} - \frac{\Gamma}{2\pi R_i^2}\right] \frac{R_i^2 R_o}{\alpha_n} J_2\left(\alpha_n \frac{R_i}{R_o}\right)$$

$$B_2 = \frac{V_{\theta o}}{R_o} \int_{R_i}^{R_o} r^2 J_1\left(\alpha_n \frac{r}{R_o}\right) dr$$

$$= \frac{V_{\theta o}}{\alpha_n} \left[R_o^2 J_2(\alpha_n) - R_i^2 J_2\left(\alpha_n \frac{R_i}{R_o}\right)\right]$$

and

$$B_3 = -\frac{\Gamma}{2\pi} \int_{R_i}^{R_o} J_1\left(\alpha_n \frac{r}{R_o}\right) dr$$

$$= \frac{\Gamma R_o}{2\pi\alpha_n} \left[J_0(\alpha_n) - J_0\left(\alpha_n \frac{R_i}{R_o}\right)\right]$$

Using the identities,

$$J_2\left(\alpha_n \frac{R_i}{R_o}\right) = \frac{2 R_o}{\alpha_n R_i} J_1\left(\alpha_n \frac{R_i}{R_o}\right) - J_0\left(\alpha_n \frac{R_i}{R_o}\right)$$

and $J_2(\alpha_n) = - J_0(\alpha_n)$,

$$A_n = - 4V_{\theta o} \frac{\left[1 + \left(\frac{R_i}{R_o}\right)^2\right]\left(\frac{R_o}{R_i}\right)}{\alpha_n^2 J_o^2(\alpha_n)} J_1\left(\alpha_n \frac{R_i}{R_o}\right)$$

Then,

$$\frac{V_\theta(t,r)}{V_{\theta o}} = \left(\frac{r}{R_o}\right) + 4\left(\frac{R_i}{R_o}\right) \sum_{n=1}^{\infty} \frac{J_1\left(\alpha_n \frac{R_i}{R_o}\right)}{\alpha_n^2 J_o^2(\alpha_n)} J_1\left(\alpha_n \frac{r}{R_o}\right) e^{-\left(\frac{\alpha_n}{R_o}\right)^2 \nu t} \qquad (B.10)$$

(2) No-Slip at the Wall

The governing equation is (2.2.5), and the boundary and initial conditions are,

(v) $V_\theta = 0$ for $r = 0$ and $t \geq 0$

(vi) $V_\theta = 0$ for $r = R_o$ and $t > 0$

(vii) $$V_\theta(0,r) = \begin{cases} \dfrac{\Gamma}{2\pi R_i^2}\, r & \text{for } 0 \leq r \leq R_i \\ \dfrac{\Gamma}{2\pi r} & \text{for } R_i \leq r \leq R_o \end{cases}$$

(viii) $$\lim_{t\to\infty} V_\theta = V_{\theta o}\left(\frac{r}{R_o}\right).$$

Equation (2.2.5) and the boundary conditions are similar with the previous case, thereby,

$$V_\theta(t,r) = \sum_{n=1}^{\infty} A_n J_1\left(\alpha_n \frac{r}{R_o}\right) e^{-\left(\frac{\alpha_n}{R_o}\right)^2 \nu t}$$

Similarly,

$$A_n = 2V_{\theta o}\left[\frac{2}{\alpha_n^2\left(\frac{R_i}{R_o}\right)} \frac{J_1\left(\alpha_n \frac{R_i}{R_o}\right)}{J_o^2(\alpha_n)} - \frac{1}{\alpha_n J_o(\alpha_n)}\right]$$

Then,

$$\frac{V_\theta(t,r)}{V_{\theta o}} = 2\sum_{n=1}^{\infty}\left[\frac{2}{\alpha_n^2 \frac{R_i}{R_o}} \frac{J_1\left(\alpha_n \frac{R_i}{R_o}\right)}{J_o^2(\alpha_n)} - \frac{1}{\alpha_n J_o(\alpha_n)}\right] J_1\left(\alpha_n \frac{r}{R_o}\right) e^{-\left(\frac{\alpha_n}{R_o}\right)^2 \nu t}$$

B.3 Evaluation of Important Integrals

$$\text{(i)} \int_0^{R_o} r^2 J_1\left(\alpha_n \frac{r}{R_o}\right) dr \tag{B.11}$$

Integral (B.11) must be integrated by parts,

let $u = r^2$ and $dv = J_1\left(\alpha_n \frac{r}{R_o}\right) dr$,

then, $du = 2rdr$ and $v = -\frac{R_o}{\alpha_n} J_o\left(\alpha_n \frac{r}{R_o}\right)$.

With the above transformation (A.11) gives,

$$\int_0^{R_o} r^2 J_1\left(\alpha_n \frac{r}{R_o}\right) dr = -\frac{R_o^3}{\alpha_n} J_o\left(\alpha_n\right) + 2\left(\frac{R_o}{\alpha_n}\right) \int_0^{R_o} r J_o\left(\alpha_n \frac{r}{R_o}\right) dr$$

the integral on the right hand side is zero when evaluated, therefore,

$$\int_0^{R_o} r^2 J_1\left(\alpha_n \frac{r}{R_o}\right) dr = -\frac{R_o^3}{\alpha_n} J_o\left(\alpha_n\right) \tag{B.12}$$

$$\text{(ii)} \int_0^{R_o} r J_1\left(\alpha_n \frac{r}{R_o}\right) J_2\left(\alpha_m \frac{r}{R_o}\right) dr \tag{B.13}$$

from orthogonality;

$$\text{integral (B.13)} = \begin{cases} 0 & \text{for} \quad \alpha_n \neq \alpha_m \\ \dfrac{R_o^2}{2} J_o^2(\alpha_n) & \text{for} \quad \alpha_n = \alpha_m \end{cases} \tag{B.14}$$

$$\text{(iii)} \quad \int_0^{R_o} \left[\frac{\partial J_1\left(\alpha_n \frac{r}{R_o}\right)}{\partial r} - \frac{J_1\left(\alpha_n \frac{r}{R_o}\right)}{r}\right]\left[\frac{\partial J_1\left(\alpha_m \frac{r}{R_o}\right)}{\partial r} - \frac{J_1\left(\alpha_m \frac{r}{R_o}\right)}{r}\right] r dr \tag{B.15}$$

With the aid of

$$\frac{\partial}{\partial r}\left[J_1\left(\alpha_n \frac{r}{R_o}\right)\right] - \frac{J_1\left(\alpha_n \frac{r}{R_o}\right)}{r} = r \frac{\partial}{\partial r}\left[\frac{J_1\left(\alpha_n \frac{r}{R_o}\right)}{r}\right],$$

$$\frac{\partial}{\partial r}\left[J_1\left(\alpha_m \frac{r}{R_o}\right)\right] - \frac{J_1\left(\alpha_m \frac{r}{R_o}\right)}{r} = r \frac{\partial}{\partial r}\left[\frac{J_1\left(\alpha_m \frac{r}{R_o}\right)}{r}\right]$$

and the identity,

$$\frac{d}{dX}\left\{\frac{J_n(X)}{X^n}\right\} = -\frac{J_{n+1}(X)}{X^n}$$

the integral (B.15) becomes,

$$\frac{\alpha_n \alpha_m}{R_o^2} \int_0^{R_o} r J_2\left(\alpha_n \frac{r}{R_o}\right) J_2\left(\alpha_m \frac{r}{R_o}\right) dr = \frac{\alpha_n \alpha_m}{R_o^2} \int_0^{R_o} r^2 J_2\left(\alpha_n \frac{r}{R_o}\right) \frac{J_2\left(\alpha_m \frac{r}{R_o}\right)}{r} dr \tag{B.16}$$

Letting,

$$u = r^2 J_2\left(\alpha_n \frac{r}{R_o}\right) \qquad \text{and} \qquad dv = \frac{J_2\left(\alpha_m \frac{r}{R_o}\right)}{r} \, dr$$

and integrating by parts the right hand side of (B.16) yields,

$$\frac{\alpha_n^2}{R_o^2} \int_0^{R_o} r \, J_1\left(\alpha_n \frac{r}{R_o}\right) J_1\left(\alpha_m \frac{r}{R_o}\right) dr \tag{B.17}$$

where;

$$du = \left(\frac{\alpha_n}{R_o}\right) r^2 J_1\left(\alpha_n \frac{r}{R_o}\right) dr \qquad \text{and} \qquad v = -\frac{R_o}{\alpha_m} \frac{J_1\left(\alpha_m \frac{r}{R_o}\right)}{r}$$

From eq. (B.14), the integral (B.17) gives,

$$\frac{\alpha_n^2}{2} J_o^2\left(\alpha_n\right) \qquad \text{for} \qquad \alpha_n = \alpha_m \tag{B.18}$$

and zero if $\alpha_n \neq \alpha_m$.

APPENDIX C

APPENDIX C

Commencing with eqs. (5.2.1) and (5.2.2), and separating the dependent variables into mean and fluctuating parts, followed by a time averaging, yield the Reynolds equations,

radial momentum

$$\frac{\partial \bar{V}_r}{\partial t} + \frac{\partial(\bar{V}_r^2)}{\partial r} + \frac{\partial(\bar{V}_r\bar{V}_z)}{\partial z} + \frac{\bar{V}_r^2 - \bar{V}_\theta^2}{r} = -\frac{\partial \bar{\hat{P}}}{\partial r} + \nu\left[\nabla^2\bar{V}_r - \frac{\bar{V}_r}{r^2}\right]$$

$$- \left[\frac{1}{r}\frac{\partial}{\partial r}(r\overline{V_r'^2}) + \frac{\partial}{\partial z}(\overline{V_r'V_z'}) + \frac{\overline{V_\theta'^2}}{r}\right] \qquad (C.1)$$

tangential momentum

$$\frac{\partial \bar{V}_\theta}{\partial t} + \frac{\partial}{\partial r}(\bar{V}_\theta\bar{V}_r) + \frac{\partial}{\partial z}(\bar{V}_\theta\bar{V}_z) + \frac{2\bar{V}_r\bar{V}_\theta}{r} = \nu\left[\nabla^2\bar{V}_\theta - \frac{\bar{V}_\theta}{r^2}\right]$$

$$- \left[\frac{\partial}{\partial r}(\overline{V_\theta'V_r'}) + \frac{\partial}{\partial z}(\overline{V_\theta'V_z'}) + \frac{2\overline{V_\theta'V_r'}}{r}\right]$$

axial momentum

$$\frac{\partial \bar{V}_z}{\partial t} + \frac{\partial}{\partial r}(\bar{V}_z\bar{V}_r) + \frac{\partial}{\partial z}(\bar{V}_z^2) + \frac{\bar{V}_z\bar{V}_r}{r} = -\frac{\partial \bar{\hat{P}}}{\partial z} + \nu\nabla^2\bar{V}_z$$

$$- \left[\frac{1}{r}\frac{\partial}{\partial r}(r\,\overline{V_r'V_z'}) + \frac{\partial}{\partial z}(\overline{V_z'^2})\right]$$

The continuity equation becomes,

$$\frac{\partial \bar{V}_r}{\partial r} + \frac{\bar{V}_r}{r} + \frac{\partial \bar{V}_z}{\partial z} = 0 \qquad (C.2)$$

The momentum equations (C.1) have the same form for the mean dependent variables with those in eq. (5.1.1). However, the fluctuating components of the velocities have enhanced the stress tensor with a portion. This is present in the right-hand side of the momentum equations, where the stress tensor components are given by,

$$\sigma_{rr} = \left\{ -\bar{\hat{P}} + 2\nu \frac{\partial \bar{V}_r}{\partial r} - \overline{V_r'^2} \right\} \rho$$

$$\sigma_{\theta\theta} = \left\{ -\bar{\hat{P}} + 2\nu \frac{\bar{V}_r}{\partial r} - \overline{V_\theta'^2} \right\} \rho$$

$$\sigma_{zz} = \left\{ -\bar{\hat{P}} + 2\nu \frac{\partial \bar{V}_z}{\partial z} - \overline{V_z'^2} \right\} \rho$$

$$\sigma_{r\theta} = \sigma_{\theta r} = \left\{ \nu \left(\frac{\partial \bar{V}_\theta}{\partial r} - \frac{\bar{V}_\theta}{r} \right) - \overline{V_r' V_\theta'} \right\} \rho$$

$$\sigma_{zr} = \sigma_{rz} = \left\{ \nu \left(\frac{\partial \bar{V}_r}{\partial z} + \frac{\partial V_z}{\partial r} \right) - \overline{V_r' V_z'} \right\} \rho$$

$$\sigma_{\theta z} = \sigma_{\theta z} = \left\{ \nu \frac{\partial \bar{V}_\theta}{\partial z} - \overline{V_\theta' V_z'} \right\} \rho$$

If one accepts the Boussinesqu hypothesis, that the turbulent stresses behave in the same manner as the viscous stresses,

$$\sigma_{ij} = \rho\left\{-\hat{P}\,\delta_{ij} + \nu\left(\frac{\partial \bar{u}_i}{\partial x_j} + \frac{\partial \bar{u}_j}{\partial x_i}\right) - \overline{u_i' u_j'}\right\}$$

$$= \rho\left\{-\hat{P}\,\delta_{ij} + (\nu + \varepsilon_m)\left[\frac{\partial \bar{u}_i}{\partial x_j} + \frac{\partial \bar{u}_j}{\partial x_i}\right]\right\}$$

where ε_m is the eddy viscosity, then the momentum equations become,

radial momentum

$$\frac{\partial \bar{V}_r}{\partial t} + \frac{\partial}{\partial r}(\bar{V}_r^2) + \frac{\partial}{\partial z}(\bar{V}_r \bar{V}_z) + \frac{\bar{V}_r^2 - \bar{V}_\theta^2}{r} = -\frac{\partial \overline{\hat{P}}}{\partial r} + \frac{1}{r}\frac{\partial}{\partial r}$$

$$\left[2r\,\nu_T \frac{\partial}{\partial r}(\bar{V}_r)\right] + \frac{\partial}{\partial z}\left[\nu_T\left(\frac{\partial \bar{V}_r}{\partial z} + \frac{\partial \bar{V}_z}{\partial r}\right)\right] - 2\,\nu_T \frac{\bar{V}_r}{r^2}$$

tangential momentum

$$\frac{\partial \bar{V}_\theta}{\partial t} + \frac{\partial}{\partial r}(\bar{V}_\theta \bar{V}_r) + \frac{\partial}{\partial z}(\bar{V}_\theta \bar{V}_z) + 2\frac{\bar{V}_\theta \bar{V}_r}{r} = \frac{1}{r^2}\frac{\partial}{\partial r}\left[r^3\,\nu_T \frac{\partial}{\partial r}\left(\frac{\bar{V}_\theta}{r}\right)\right]$$

$$+ \frac{\partial}{\partial z}\left(\nu_T \frac{\partial \bar{V}_\theta}{\partial z}\right)$$

axial momentum (C.4)

$$\frac{\partial \bar{V}_z}{\partial t} + \frac{\partial}{\partial r}(\bar{V}_z \bar{V}_r) + \frac{\partial}{\partial z}(\bar{V}_z^2) + \frac{\bar{V}_r \bar{V}_z}{r} = -\frac{\partial \overline{\hat{P}}}{\partial z} + \frac{1}{r}\frac{\partial}{\partial r}$$

$$\left[r\,\nu_T\left(\frac{\partial \bar{V}_r}{\partial z} + \frac{\partial \bar{V}_z}{\partial r}\right)\right] + \frac{\partial}{\partial z}\left(2\,\nu_T \frac{\partial \bar{V}_z}{\partial z}\right)$$

where,

$$\nu_T = \nu_\ell + \dot{\epsilon}_m$$

If ϵ_m is constant, eq. (C.4) is equivalent to eq. (5.2.1), or the turbulent flow is assumed to behave as a laminar flow with an enhanced viscosity ν_T.

APPENDIX D

APPENDIX D

D.1 V_r - Source Terms

$$FVRR = \frac{1}{4\Delta r}\left[\left(V_{r_{i,j}} + V_{r_{i+1,j}}\right)^2 + \alpha\left|V_{r_{i,j}} + V_{r_{i+1,j}}\right|\left(V_{r_{i,j}} - V_{r_{i+1,j}}\right)\right.$$

$$\left. - \left(V_{r_{i-1,j}} + V_{r_{i,j}}\right)^2 - \alpha\left|V_{r_{i-1,j}} + V_{r_{i,j}}\right|\left(V_{r_{i-1,j}} - V_{r_{i,j}}\right)\right]$$

$$FVRZ = \frac{1}{4\Delta z}\left[\left(V_{z_{i,j}} + V_{z_{i+1,j}}\right)\left(V_{r_{i,j}} + V_{i,j+1}\right) + \alpha\left|V_{z_{i,j}} + V_{z_{i+1,j}}\right|\right.$$

$$\left(V_{r_{j,j}} - V_{r_{i,j+1}}\right) - \left(V_{z_{i,j-1}} + V_{z_{i+1,j-1}}\right)\left(V_{r_{i,j-1}} + V_{r_{i,j}}\right)$$

$$\left. - \alpha\left|V_{z_{i,j-1}} + V_{z_{i+1,j-1}}\right|\left(V_{r_{i,j-1}} - V_{r_{i,j}}\right)\right]$$

$$FVRC = \frac{1}{8\Delta r(i-1)}\left[\left(V_{r_{i,j}} + V_{r_{i+1,j}}\right)^2 + \left(V_{r_{i-1,j}} + V_{r_{i,j}}\right)^2\right.$$

$$+ \alpha\left|V_{r_{i,j}} + V_{r_{i+1,j}}\right|\left(V_{r_{i,j}} - V_{r_{i+1,j}}\right) + \alpha\left|V_{r_{i-1,j}} + V_{r_{i,j}}\right|$$

$$\left.\left(V_{r_{i-1,j}} + V_{r_{i,j}}\right)\right] - \frac{1}{4\Delta r(i-1)}\left(V_{\theta_{i,j}} + V_{\theta_{i+1,j}}\right)^2$$

$$VISVR = \nu\left[\frac{1}{\Delta r^2}\left(V_{r_{i+1,j}} - 2\,V_{r_{i,j}} + V_{r_{i-1,j}}\right) + \frac{1}{\Delta z^2}\left(V_{r_{i,j+1}} - 2\,V_{r_{i,j}} + V_{r_{i,j-1}}\right) + \frac{1}{2\Delta r^2(i-1)}\left(V_{r_{i+1,j}} - V_{r_{i-1,j}} - \frac{V_{r_{i,j}}}{\Delta r^2(i-1)^2}\right)\right]$$

D.2 V_θ - Source Terms

$$FV\theta R = \frac{1}{2\Delta r}\left[V_{r_{i,j}}\left(V_{\theta_{i,j}} + V_{\theta_{i+1,j}}\right) + \alpha\left|V_{r_{i,j}}\right|\left(V_{\theta_{i,j}} - V_{\theta_{i+1,j}}\right) - V_{r_{i-1,j}}\left(V_{\theta_{i-1,j}} + V_{\theta_{i,j}}\right) - \alpha\left|V_{r_{i-1,j}}\right|\left(V_{\theta_{i-1,j}} - V_{\theta_{i,j}}\right)\right]$$

$$FV\theta Z = \frac{1}{2\Delta z}\left[V_{z_{i,j}}\left(V_{\theta_{i,j}} + V_{\theta_{i,j+1}}\right) + \alpha\left|V_{z_{i,j}}\right|\left(V_{\theta_{i,j}} - V_{\theta_{i,j+1}}\right) - V_{z_{i,j-1}}\left(V_{\theta_{i,j-1}} + V_{\theta_{i,j}}\right) - \alpha\left|V_{z_{i,j-1}}\right|\left(V_{\theta_{i,j-1}} - V_{\theta_{i,j}}\right)\right]$$

$$FV\theta C = \frac{1.}{2\Delta r(i-1.5)} \left[V_{r_{i,j}} \left(V_{\theta_{i,j}} + V_{\theta_{i+1,j}} \right) + V_{r_{i-1,j}} \left(V_{\theta_{i-1,j}} + V_{\theta_{i,j}} \right) \right.$$

$$\left. + \alpha \left| V_{r_{i,j}} \right| \left(V_{\theta_{i,j}} - V_{\theta_{i+1,j}} \right) + \alpha \left| V_{r_{i-1,j}} \right| \left(V_{\theta_{i-1,j}} - V_{\theta_{i,j}} \right) \right]$$

$$VISV\theta = \nu \left[\frac{1}{\Delta r^2} \left(V_{\theta_{i+1,j}} - 2\, V_{\theta_{i,j}} + V_{\theta_{i-1,j}} \right) + \frac{1}{\Delta z^2} \left(V_{\theta_{i,j+1}} \right. \right.$$

$$\left. - 2\, V_{\theta_{i,j}} + V_{\theta_{i,j-1}} \right) + \frac{1}{2\Delta r^2(i-1.5)} \left(V_{\theta_{i,j+1,j}} - V_{\theta_{i-1,j}} \right)$$

$$\left. - \frac{V_{\theta_{i,j}}}{\Delta r^2 (i-1.5)^2} \right]$$

D.3 V_z - Source Terms

$$FVZR = \frac{1}{4\Delta r} \left[\left(V_{r_{i,j}} + V_{r_{i,j+1}} \right) \left(V_{z_{i+1,j}} + V_{r_{i+1,j}} + \alpha \left| V_{r_{i,j}} + V_{r_{i,j+1}} \right| \right. \right.$$

$$\left(V_{z_{i,j}} - V_{z_{i+1,j}} \right) - \left(V_{r_{i-1,j}} + V_{r_{i-1,j+1}} \right) \left(V_{z_{i-1,j}} + V_{z_{i,j}} \right)$$

$$\left. - \alpha \left| V_{r_{i-1,j}} + V_{r_{i-1,j+1}} \right| \left(V_{z_{i-1,j}} - V_{z_{i,j}} \right) \right]$$

$$FVZZ = \frac{1}{4\Delta z}\left[\left(V_{z_{i,j}} + V_{z_{i,j+1}}\right)^2 + \alpha\left|V_{z_{i,j}} + V_{z_{i,j+1}}\right|\right.$$

$$\left(V_{z_{i,j}} - V_{z_{i,j+1}}\right) - \left(V_{z_{i,j-1}} + V_{z_{i,j}}\right)^2 - \alpha\left|V_{z_{i,j-1}} + V_{z_{i,j}}\right|$$

$$\left.\left(V_{z_{i,j-1}} - V_{i,j}\right)\right]$$

$$FVZC = \frac{1}{8\Delta r(i-1.5)}\left[\left(V_{r_{i,j}} + V_{r_{i,j+1}}\right)\left(V_{z_{i,j}} + V_{z_{j+1,j}}\right)\right.$$

$$+\left(V_{r_{i-1,j}} + V_{r_{i-1,j+1}}\right)\left(V_{z_{i-1,j}} + V_{z_{i,j}}\right) + \alpha\left|V_{r_{i,j}} + V_{r_{i,j+1}}\right|$$

$$\left(V_{z_{i,j}} - V_{z_{i+1,j}}\right) + \alpha\left|V_{r_{i=1,j}} + V_{r_{i-1,j+1}}\right|\left(V_{z_{i-1,j}} - V_{z_{i,j}}\right)\Big]$$

$$VISVZ = \nu\left[\frac{1}{\Delta r^2}\left(V_{z_{i+1,j}} - 2\,V_{z_{i,j}} + V_{z_{i-1,j}}\right) + \frac{1}{\Delta z^2}\left(V_{z_{i,j+1}}\right.\right.$$

$$\left.\left. - 2\,V_{z_{i,j}} + V_{z_{i,j-1}}\right) + \frac{1}{2\Delta r^2(i-1.5)}\left(V_{z_{i+1,j}} - V_{z_{i-1,j}}\right)\right]$$

APPENDIX E

APPENDIX E

E.1 Potential Flow Solution

Solution to the potential flow, assumed in Chapter 4, can be obtained utilizing a numerical technique. Combining the η-vorticity and continuity equations one arrives at a single equation with the stream-function as the dependent variable.

$$\frac{\partial^2\psi}{\partial r^2} - \frac{1}{r}\frac{\partial\psi}{\partial r} + \frac{\partial^2\psi}{\partial z^2} = 0 \qquad (E.1)$$

where,

$$V_r = -\frac{1}{r}\cdot\frac{\partial\psi}{\partial z} \quad \text{and} \quad V_z = \frac{1}{r}\frac{\partial\psi}{\partial r} \qquad (E.2)$$

The general solution of eq. (E.1) can be easily expressed in a linear combination of Bessel functions. However, the complexities arising from the boundaries, forces one to seek a numerical solution. For this reason the flow domain was descretized into rectangular computational cells as depicted in Fig. (E.1). The centered space finite difference approximation of eq. (E.1) is,

$$\psi_{i,j}^{\ell+1} = \frac{1}{2(1+\lambda^2)}\left\{\psi_{i-1,j}^{\ell+1} + \psi_{i+1,j}^{\ell} + \lambda^2\left(\psi_{i,j-1}^{\ell+1} + \psi_{i,j+1}^{\ell}\right) - \frac{1}{r_i}\cdot\right.$$

$$\left.\cdot\left(\psi_{i+1,j}^{\ell} - \psi_{i-1,j}^{\ell+1}\right)\right\} \qquad (E.3)$$

where $\lambda = \Delta r/\Delta z$, and $\ell+1$ and ℓ refer to new and previous iteration levels respectively,

Equation (E.3) can equally be written in terms of residuals ($R_{i,j}$) as,

$$\psi_{i,j}^{\ell+1} = \psi_{i,j}^{\ell} + \frac{\Delta r^2 \, R_{i,j}}{2(1+\lambda^2)} \qquad (E.4)$$

where the expression for the residuals $R_{i,j}$ is given by,

$$R_{i,j} = \left\{ \frac{\psi_{i-1,j}^{\ell+1} + \psi_{i+1,j}^{\ell}}{\Delta r^2} + \frac{\psi_{i,j-1}^{\ell+1} + \psi_{i,j+1}^{\ell}}{\Delta z^2} - \frac{1}{r_i} \frac{\left(\psi_{i+1,j}^{\ell} - \psi_{i-1,j}^{\ell+1}\right)}{2\Delta r} \right\}$$

To accelerate convergence, the successive overrelaxation method (SOR) could be used. For this, a relaxation parameter, ω, is applied to eq. (E.4),

$$\psi_{i,j}^{\ell+1} = \psi_{i,j}^{\ell} + \frac{\omega \Delta r^2}{2(1+\lambda^2)} R_{i,j} \qquad (E.5)$$

where, $1 \leq \omega \leq 2$.

This method also known as "extrapolated Liebmann's," can drastically reduce the computational effort if an optimum ω is applied.

The necessary boundary conditions for the solution are,

(i) for the inner cylinder and bottom disk, $\psi = 0$,

(ii) on the outer cylinder wall and top disk,

$\psi = R_o |V_{rin}| h_{in}$,

(iii) at the inlet, $\psi = R_o |V_{rin}| Z$,

(iv) and on the exit plane, $\psi = \left(r^2 - R_{CE}^2/2\right) V_{ZE}$.

To evaluate the velocity components, V_r and V_z, the eqs. (E.2) are used. Inside the flow domain both V_r and V_z must be represented with central space finite differences in order to obtain a second order accurate velocity representation. For the velocities on the boundaries a second order accurate forward or backward finite differencing scheme must be utilized.

The numerical solution is obtained via eqs. (E.3) or (E.5). The flowfield is swept repeatedly from inlet to outlet ($i \downarrow$ and $j \uparrow$) until the expression,

$$\frac{\left|\psi^{\ell+1} - \psi^{\ell}\right|}{\psi_{max}} \leq \varepsilon$$

is true everywhere in the flowfield. The small parameter ε takes a value of 0.0001. A smaller ε will virtually give unnoticeable changes of the ψ values everywhere in the field.

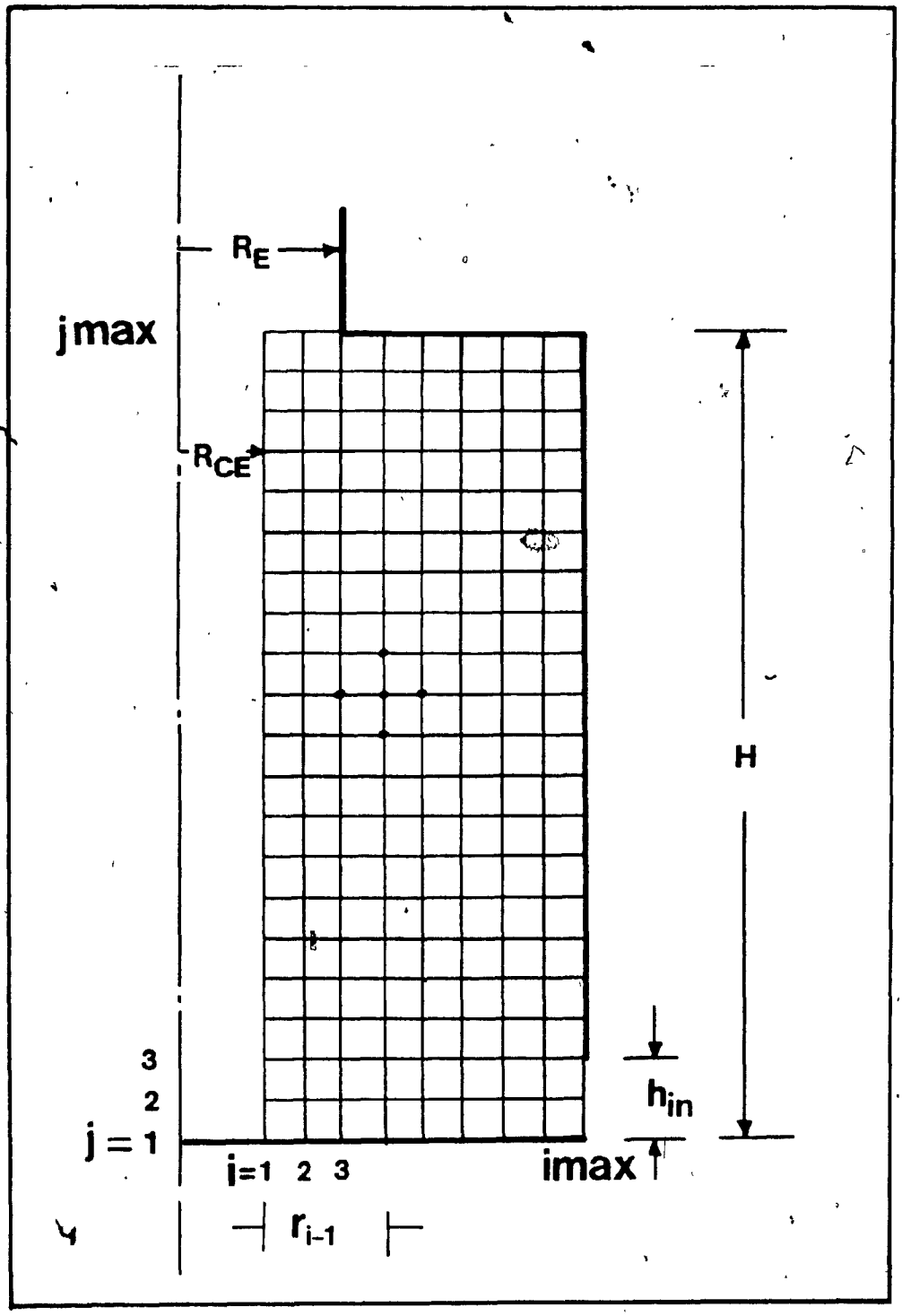

Fig. E.1: The Grid System for the Inviscid Potential Flow Simulation.